Benemérita Universidad Autónoma de Puebla

Facultad de Ciencias Físico-Matemáticas

Propiedades de los sistemas creados en colisiones p-p y p-Pb en ALICE del LHC

tesis presentada a

Posgrado en Física Aplicada
de la Facultad de Ciencias Físico Matemáticas

como requisito parcial para obtener el grado de:

Doctor en Ciencias (Física Aplicada)

por

Héctor Bello Martínez

Asesores:

Dr. Arturo Fernández Téllez (FCFM-BUAP, México)
Dr. Antonio Ortiz Velásquez (ICN-UNAM, México)

Puebla Pue.
14 de diciembre de 2017

Benemérita Universidad Autónoma de Puebla

Facultad de Ciencias Físico-Matemáticas

Properties of the systems created in p-p and p-Pb collisions in ALICE at LHC

Thesis presented to

Graduate program in Applied Physics
Faculty of Physical and Mathematical Science

as a partial requirement to get the degree:

Doctor in Sciences (Applied Physics)

by

Héctor Bello Martínez

Advisors

Dr. Arturo Fernández Téllez (FCFM-BUAP, México)
Dr. Antonio Ortiz Velásquez (ICN-UNAM, México)

Puebla Pue.
December 14th, 2017

Title (english): Properties of the systems created in p-p and p-Pb collisions in ALICE at LHC.
Titulo (español): Propiedades de los sistemas creados en colisiones p-p y p-Pb en ALICE del LHC.
Author: Héctor Bello Martínez.

COMMITTEE

President/Presidente:

Dra. Irais Bautista Guzmán
FCFM-BUAP
Cátedra CONACYT

Spokesmember/Vocal

Dra. Isabel Pedraza Morales
FCFM-BUAP

Secretary/Secretario:

Dr. Mario Rodríguez Cahuantzi
FCFM-BUAP

Supply member/Suplente:

Dr. Gilberto Tavares Velazco
FCFM-BUAP

External member/Vocal externo

Dr. Gerardo Herrera Corral
CINVESTAV-IPN

External member/Vocal externo

Dr. Lukas Nellen Filla
ICN-UNAM

Advisor/Asesor:

Dr. Arturo Fernández Téllez
FCFM-BUAP

Advisor/Asesor:

Dr. Antonio Ortiz Velásquez
ICN-UNAM

Contents

Aknowledgements

> Sans vous, sans cette main affectueuse que vous avez tendue au petit enfant pauvre que j'étais, sans votre enseignement, et votre exemple, rien de tout cela ne serait arrivé
>
> (Albert Camus)

All big "oeuvre" starts with a big dream, a dream that needs many people to get accomplished. Due to this, I want to thank and dedicate this work to:

My father Héctor Bello, who deserve all my appreciation, for believing in me and for the time he dedicated to me, without him I can not be the man I am.

Arturo Fernández who allowed me to work in this international and very nice experiment at CERN, I acknowledge his instruction and time dedicated to each meeting we had every saturday to discuss about the progress during the week.

Antonio Ortiz who has shown me the spirit of a researcher that anybody can achieve with dedication and hard work, I also acknowledge his support, patience and useful discussions.

Guy Paić for sharing his experience, deepest questions and thoughts during my stays at ICN-UNAM. Dr. Eleazar Cuautle, for the support with the "red ALICE México".

Francesca Bellini and Alexander Kalweit (LF-PWG conveners), for the usesful comments and time dedicated to my presentations at each stage of this work.

Jacek Otwinowsky, Oliver Busch, Anton Andronic, and Peter Christiansen, for their questions and recommendations as members of the Analysis Review Committee (ARC) and Internal Review Committee (IRC).

Irais Bautista, Isabel Pedraza, Mario Rodriguez, members of my PhD committee, for the time dedicated to follow my progress during each semester.

David Chinellato, Michele Floris, Satyajit Jena and Chiara Bianchin, for sharing with me their knowledge during my service task in ALICE.

I also want to thank to Christian Bierlich, Gergely Barnafoldy, Lee Barnby, Roberto Preghenella, Gerardo Herrera, Mario Ivan Martinez, Guillermo Tejeda, Pedro Gonzalez and Roger Hernández for their friendship and fruitful conversations.

Thanks to my colleagues Gyula Bencédi, Omar Vázquez, Sergio Iga and Vytautas Vislavicius, for all technical discussions we had and who already know the effort needed to get done this kind of analysis in ALICE.

Thanks to my friends at CERN: Luis A. Pérez Moreno, for his big friendship, Abraham Villatoro, Sol Angel Rojas, Rogelio Reyes and Iraq Rabadan for the good times.

Also to my friends at BUAP who always believed in me and my capabilities to accomplish my PhD: Gerardo Hernández, Elias Flores, Phriel Cavildo, Juan Carlos Molina, Marxil Sánchez, Josue Lima, Ricardo Mejía, Enrique Montero, Salvador Sosa, Ramón Villanueva and also including to the coffee-time-crew at ICFTP[1] (Sebastian Rosado, Manuel Solis Tobon and Diana Rojas).

---

[1] Italian Coffee for Theoretical Physics

I thank to friends and partners at the lab-jail ("el calabozo"): Miguel Nava, Ricardo Alvarado, Pablo Fierro, Rodrigo Mojica, Pedro Esquipula, Ángel Sierra, Rafa Escamilla and Luis Valenzuela, who so many times coexist with me in the office.

Also to my friends and colleagues at ICN: Omar Vázquez, Sergio Iga, Edgar Rosas, Edgar Pérez, Enrique Patiño, Luciano Díaz and Eduardo Murrieta. To my friends colleagues from around the world, David Zhu, Simen Hellesund, Santeri Laurila, Manuel Morgado, José Jiménez, Josue Durán, Ignacio Fabre, Steffen Webber and Enrico Speranza. To my friends José Martinez, Williams Chang, Eduardo Ramírez and Ivan Martinez, for those good times.

To all the very nice friends (women) with every conversation and good moments I had with, made me feel happy: Tania Martinez, Emma Gonzalez, Daniela Blanco, Cristal Robles, Diana Rojas, Pilar Alonso, Dulce Garcia, Freja Thorsen, Julia Peña, Maria Di Domenico, Mariel Estevez, Ivania Matura, Marysia Stefaniak, Dalia Ramirez, Thalia Gallegos, and Shanon Rosslyn.

To my brothers Hecsar, Hecsari and Hecsare, who always gave me the strenght to continue without surrender, cause I wanna show that everthing is possible and one just needs to do it and find the best way to get it.

"In this monetary system, money is always useful and as physicists we know that all is quantitatively measurable as much the natural numbers cardinality, but money and time are finit".

Last but not least, I want to thank the financial support from EPLANET and CONACYT under the grant-project No. 260440 for stays at CERN (France-Switzwerland), FCFM-BUAP (Puebla México) and ICN-UNAM (México city) and projects PAPIIT: IA102515 y IN102118. Also aknowledge the computing support from Tlapoa-UNAM and LNS-BUAP clusters.

"Real generosity towards the future lies in giving all to the present."
(Albert Camus, Notebooks 1935-1942)

Resumen

Se ha establecido que las colisiones ultra-relativistas producen un sistema caliente y denso en QCD el cual se comporta como un líquido perfecto. Sin embargo, el sistema no es el teóricamente predicho Plasma de Quarks y Gluones, su estudio resulta importante para entender la evolución cósmica de nuestro Universo. También como los aspectos específicos del sector de QCD no perturbativa. Por tres décadas, las colisiones protón protón de mínimo sesgo fueron usadas como la base para extraer las nuevas propiedades de los sistemas calientes y densos. Sorprendentemente, el análisis de colisiones pp como una función de la multiplicidad del evento han revelado nuevos fenómenos: comportamiento del tipo colectivo. Para la comunidad de iones pesados es crucial entender el origen de las similitudes entre los sistemas creados en colisiones pp, p-A y A-A.

En esta tesis se realizó un estudio de los sistemas pequeños (colisiones pp y p-A) como función del contenido de jets y la multiplicidad, las interacciones multipartónicas y la reconexión por color ha recibido especial atención por que pueden producir patrones de tipo flujo radial. También incluyendo cuerdas de color, el modelo pude incrementar la producción de bariones y extrañeza.

El estudio fue hecho en 2 partes, una consiste en el estudio de observables sensibles al nuevo fenómeno, pero usando dos diferentes generadores MC: PYTHIA 8 y EPOS 3. El primero esta basado en interacciones multipartónicas y reconexión por color, mientras el último incluye evolución hidrodinámica del sistema.

Usando estas ideas analizamos datos de ALICE para colisiones pp a 13 TeV usando una aproximación alternativa basada en la forma de los eventos, específicamente, esferocidad transversa.

Abstract

It has been established that ultra-relativistic heavy-ion collisions produce a hot and dense QCD system which behaves like a perfect fluid. Albeit, the system is not the theoretical predicted Quark Gluon Plasma, its study results important to understand the cosmic evolution of our Universe. As well as specific aspects of QCD in the non-perturbative sector. For three decades, minimum-bias proton-proton collisions were used as the baseline in order to extract the novel properties of the hot and dense systems. Surprisingly, the analysis of pp collisions as a function of the event multiplicity revealed new phenomena: collective-like behavior. For the heavy-ion community it is crucial to understand the origin of the similarities among the systems created in pp, p-A and A-A collisions.

In this thesis a study of small systems (pp and p-A collisions) as a function of the jet content and multiplicity was done, multi-partonic interactions and color reconnection have received special attention because they can produce radial flow-like patterns. Also, including color ropes, the model can also increase the baryon and strangeness production.

The study was done in two parts, one consists on the study of observables sensitive to the new phenomena, but using two different MC event generators: PYTHIA 8 and EPOS 3. The former is based on multi-partonic interactions and color reconnection, while the latter includes the hydrodynamical evolution of the system.

Using these ideas we analyzed the ALICE data for pp collisions at 13 TeV using an alternative approach based on event shapes, specifically, transverse spherocity.

Introduction

> Scientific discovery and scientific knowledge have been achieved only by those who have gone in pursuit of it without any practical purpose whatsoever in view.
>
> (Max Planck)

The Large Hadron Collider (LHC) has an ambicious program which includes: Standard Model [1, 2, 3, 4, 5] (SM) precision measurements, followed by Beyond Standard Model as Supersymmetry (SUSY) and extradimentions searches. ALICE (A Large Ion Collider Experiment) [6, 7] is one of the four largest experiments at the LHC that has the main porpouse to study a state of matter where quarks and gluons are deconfined, the quark-gluon plasma (QGP) [8]-[11]. To reach this goals we need to understand in detail the hadron-hadron collisions and of course a deep knowledge of the detectors used for the event reconstruction. For example, the study of the hard signals needs a perfect understanding of the background produced in the collisions between the hard partons. This includes the understanding of the transverse momentum spectra in multiplicity bins, particles abundances, as well as the correlations between the observables. A lot of information can be extracted from data using the event shape variables [12][13].

In general, differential studies using pp data open the possibility to unveil novel phenomena. For example, new measurements in pp collisions as a function of the event multiplicity allowed the discovery of QGP-like features in the so-called small systems [14][15].

However, we are still far to establish the formation of the strongly interacting Quark-Gluon-Plasma in those systems, because for example other mechanisms like color reconnection (CR) and jets can contribute to mimic radial flow [16]. Therefore, double differential studies have to be performed in order to test the model predictions. To this end, event shapes offer the possibility of isolating perturbative QCD (pQCD) and non-perturbative QCD (npQCD) enhanced samples [18] which are in average, well modelled by QCD-inspired models. The study of the details of the soft and hard production will allow to understand whether the well-know QCD interactions are enough to explain the data, or, if something else is needed (maybe QGP).

Hydrodynamic calculations reproduce many of the observations qualitatively [19]. However, it has also been found that multi-parton interactions (MPI) [20] and color reconnection as implemented in Pythia [22, 23] produce radial flow patterns via boosted color strings [24]. Moreover, within the dilute-dense limit of the color glass condensate, it has been demonstrated that the physics of fluctuating color fields can generate azimuthal multi-particle correlations [25]; and the mass ordering of elliptic flow when the fragmentation implemented in Pythia is included [26]. The same observable has been studied using the multi-phase transport model [27], where the ridge structure can be generated assuming incoherent elastic scatterings of partons and the string melting mechanism. Other mechanisms like "color ropes", which are formed by the fusion of color strings close in space, can increase both the strangeness production and the radial flow-like effects [28]. The measurements of the transverse momentum (p_{T}) spectra of identified particles as a function of event multiplicity in pp collisions at the LHC [29, 30] have shown that models fail to describe the data quantitatively. Therefore, the results of those comparisons alone are not enough to give desired information about the origin of the observed effects (i.e. radial flow-like patterns). In order to extract more information, we propose the implementation of a double-differential study based on the classification of the events according to event multiplicity and the jet content. In heavy-ion collisions by studying this soft region one can naturally quantify the effect of radial flow. In the so-called MPI-based model of color reconnection, the interaction between scattered partons at soft and at hard p_{T} scales is imposed. The event-by-event partonic scatterings are mostly associated with low-p_{T} interactions, albeit the probability of having a hard scattering increases with the number of MPI. An interplay between soft and hard scatterings mediated by color strings is therefore expected to provide a strong correlation between the radial flow-like patterns and the hard component of the collision [31]. On the contrary, in the scenario where the hydrodynamical evolution of the system is the prime mechanism, jets are not expected to strongly modify the radial flow patterns.

Color reconnection is a mechanism which is interesting, basically because it allows the interactions among partons (coming from different scatterings) before the hadronization. It is needed to produce the increase of the average p_{T} as a function of the event multiplicity, and now, we also know that produces radial flow-like patterns. An analysis using event shapes for example spherocity [32, 33] allows to understand the color reconection effects in jets and in the bulk production. Beyond the potential use of this data (vs multiplicity and event shape) for MC tuning purposes, it can be used to understand a potential jet modification originated from color reconnection [31, 34].

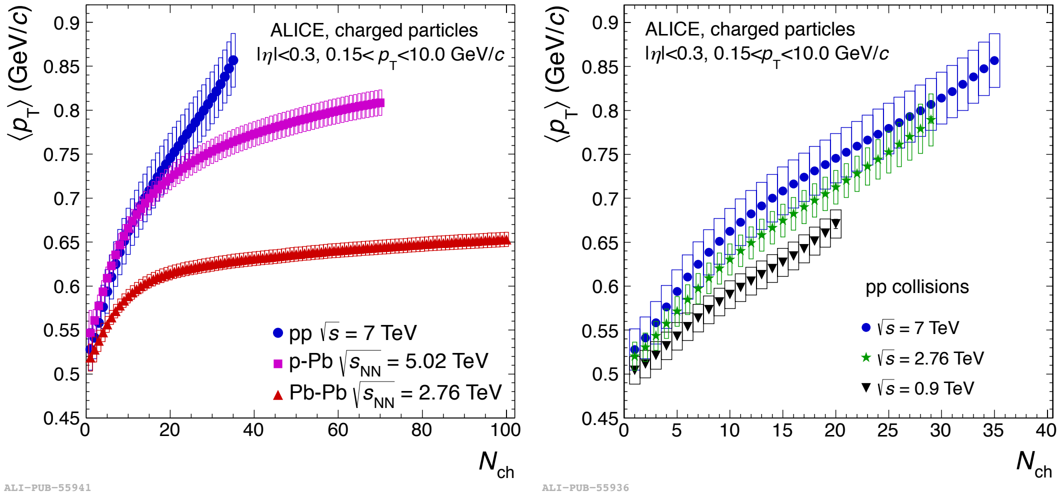

Figure 1: a) Mean p_{T} for different collisions system, b) Mean p_{T} for pp collisions at different energies [36, 37].

In Fig. 1 a, we can see the interesting behaviour of the mean transverse momentum for three different colliding systems pp, p-Pb, Pb-Pb (to see more details for each colliding system you can check [38, 39, 40, 41]). One important thing to remark is that for the three systems a first rise of the mean transverse momentum is seen for N_{ch} between 0 and 20, but just only for pp collisions (Fig. 1 b) a second rise is observed for large multiplicities. This result suggests a potential bias originated from the selection of events having a large number of particles within a very narrow pseudorapidity interval. In this thesis, we investigate the jet effects using the event structure analysis.

This thesis is organized as follows: In chapter 1, a theoretical backgroud is given. This includes discussions about the Standard Model, particularly the QCD theory [42]-[56][60]-[74] which is used to introduce the theoretically predicted QGP [8]-[10][75]-[78]. Then hadronic interactions [75] at high energies as well as event shapes are described. The chapter is closed with a discussion about the Monte Carlo modelling [101]-[106][21, 22, 23, 107, 108, 109] of the high energy pp collisions.

In chapter 2, we make a full description of the experiments at the LHC [110]-[114] specially focusing on ALICE [115, 116]. In this chapter, I describe the main detectors systems which were used in my analysis [115]-[132]. In addition, a brief summary on how the primary track reconstruction is performed in ALICE, as well as the details of the software used in ALICE to analyze the data [137, 138, 139].

In chapter 3, a discussion of some ALICE results [144]-[202] is made. The results are described in terms of the characterization of the QGP.

In chapter 4, a description of my published paper [34] is given. The paper aimed to discuss new tools in order to unveil the underlying physics which is generating the new penomena in pp collisions.

In chapter 5, I describe the data analysis done in ALICE using the event shape called spherocity. The chapter includes a full description of the event selection, correction procedure and systematic uncertainties, everything have been documented in an ALICE analysis note [32]. It is worth mentioning that in October 2017, the ALICE collaboration approved the preparation of a paper where my results will be reported [205].

In chapter 6, a discussion based on the results is given in terms of what has been found in data and in the models predictions.

Finally in chapter 7, the conclusions are presented.

Chapter 1

Theoretical Background

> Scientific knowledge is a body of statements of varying degrees of certainty-some most unsure, some nearly sure, but none absolutely certain.
>
> (Richard Feynman)

1.1 Standard Model

The Standard Model (SM) is the theory that describes all of the known elementary particle interactions, except gravity [1]. We understand for elementary particles to the matter constituents without any substructure known at the present limits between $10^{-18} - 10^{-19}$m.

The Standard Model is the effective and renormalizable quantum-relativistic theory [2], of the strong, weak and electromagnetic interactions, based on the symmetry group $SU_C(3) \times SU_L(2) \times U_Y(1)$ which unifies these 3 interactions. The symmetry group $SU_C(3)$[1] (of the special unitary matrices 3×3 or the color group, so the C subindex) characterizes the strong interactions, while the symmetry group $SU_L(2) \times U_Y(1)$[2] (or electroweak group composed by the group of special unitary matrices of dimension 2×2 with isospin (L) and the hypercharge (Y) as generators), unifies the electromagnetic and weak interactions.

The strong interactions are mediated by gluons, which just couple to quarks. The weak interaction is mediated by the massive gauge bosons $W^{\pm}$ and Z^0, while the electromagnetic interaction is mediated by the photon. The elementary particles are divided into two types (Fig. 1.1): fermions and bosons.

1. **Fermions**: Particles with half-integer spin (it could be 1/2 as leptons and quarks or 3/2 as some baryons) [3], these are described in the fermionic sector, and they are clasiffied as:

    - *Leptons*: There are six leptons in the present structure, the electron (e^-), muon (μ^-) and tau (τ^-) (with charge -1[3]) particles and their asscociated neutrinos (ν_e, ν_μ, ν_τ) (with null charge). The different varieties of the elementary particles are commonly called "flavors". The present SM assumes that there are no more than three generations of leptons.

---

[1] Subject of study of the Quantum Chromodynamics (QCD).

[2] Subject of study of the electroweak theory.

[3] In the charge units $e = 1,602176 \times 10^{-19}$ Coulombs.

- *Quarks*: There are six "flavors" of quarks. they can successfully account for all known mesons and baryons. The properties of quarks are listed in 1.1. This are the up (u), charm (c), top[4](t) quarks, (these have charge 2/3), and the down (d), strange (s), and bottom (b), (these with charge $-1/3$).

The stable states composed of quarks are called hadrons, these can be clasified by the flavour constituents as ligth flavor hadrons or heavy flavour hadrons depending, if light flavour (LF) (u with $m_u \approx 2.2$ MeV, d with $m_d \approx 4.7$ MeV and s with $m_s \approx 96$ MeV $\ll \Lambda_{QCD}$, which most of the mass of LF hadrons is generated by spontaneous breaking of chiral symmetry in QCD [11]) or heavy flavour (HF) quarks (c with $m_c \approx 1.27$ GeV, b with $m_b \approx 4.6$ GeV $\gg \Lambda_{QCD}$, the heavy quarks can only be created in pQCD processes [11]).

Baryons (composites of three quarks ($q_i q_j q_k$)) are strongly interacting hadrons [4] they are acted on by the strong nuclear force and are described by Fermi-Dirac statistics, which applies to all particles obeying the Pauli exclusion principle, some baryons have spin 1/2 (for example some from the uds baryon octect[5]) and others as 3/2 (belonging to the uds baryon decuplet).

All fermions respect the Pauli exclusion principle and they are described by Fermi statistics and the quantization rule is given by

$$\{\psi(\mathbf{r}), \mathbf{\Pi}(\mathbf{r})\} = \mathbf{i}\hbar\delta(\mathbf{r} - \mathbf{r}^{'}), \tag{1.1}$$

where $\Pi_\mu = \frac{\partial \mathcal{L}}{\partial(\partial_\mu \psi)}$ is their conjugate momentum.

The gauge bosons: Particles with integer spin [3], these are described in the bosonic sector, can be classified as scalar, vector or tensor boson:

- scalar bosons: These are spin 0 particles, for example the Higgs boson which was discovered in 2012.
- vector bosons: These are spin 1 particles and some of them are responsible of certain interactions:
  - For electromagnetic interacction, which is of infinite range produced by the *electric charge*, we asociate a bosonic field which boson is the foton who has spin 1.
  - For the weak-nuclear interaction, which is of range 10^{-18}m produced by the *weak charge*, three bosonic fields W^+, W^- and Z^0 are asociated; all having spin 1.
  - For the strong nuclear interaction, which range is $\leq 10^{-15}$m produced by *color charge*, we asociate 8 gluonic fields which bosons are the 8 gluons with spin 1.
- tensor bosons: These are particles with spin ≥ 2, for example in the gravitational interaction[6], (this has an infinite range produced by the mass), there is asociated 1 gravitational field where the graviton is the respective boson.

Some mesons are also considered as bosons [4] due to the fact that they are formed by quark anti-quark pairs ($q_i\bar{q}_j$), and their spín can be 0 or 1, they could be scalar or vectorial mesons respectively, most are scalar mesons as pions $\pi^\pm$ others as the ρ_0 or J/ψ are vectorial mesons. All the bosons are described by the Bose-Einstein statistics which quantization rule is given by:

$$[\phi(\mathbf{r}), \pi(\mathbf{r})] = \mathbf{i}\hbar\delta(\mathbf{r} - \mathbf{r}^{'}), \tag{1.2}$$

where $\pi_\mu = \frac{\partial \mathcal{L}}{\partial(\partial_\mu \phi)}$ is its conjugate momentum.

---

[4] Discovered in 1995 at Fermilab, is the heaviest quark known, with a mass of 170.9 GeV/c^2 (this is the only quark which not hadronize), and which life time is 10^{-24}s.

[5] Clasiffication from the Gell Mann Eightfold Way [5]

[6] Which until now it's not in the Standard Model, there are also tries to get a complete theory to unified this interactions with the other three.

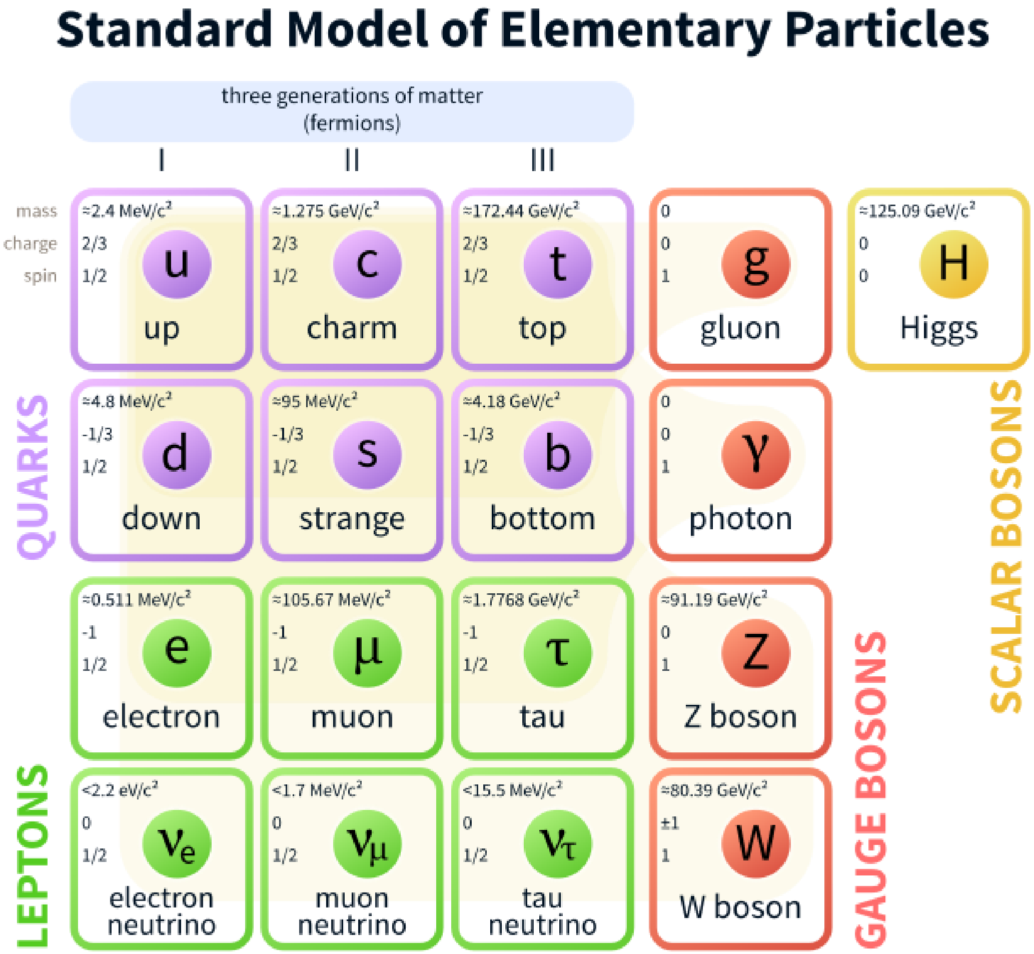

Figure 1.1: Classification and properties of particles in the SM.

1.2 Quantum Chromodynamics (QCD)

Quantum Chromodynamics [42, 43] is the theory of strong interaction between quarks and gluons in order to form hadrons. During [44, 45] 1953 physicists as Murray Gell-Mann and Kazuhiko Nishijima made a classification of the known particles not only by its charge or isospin, but also by its strangeness. Later in 1961 Gell-Mann and Yuval Ne'eman classified the hadrons in groups with similar properties and masses using "octuplets". Two years later; in 1963, Gell-Mann and George Zweig proposed that the structure of the groups could be explained by the existence of three flavors of small particles inside the hadrons: the quarks.

By those years the Δ^{++} particle was still a mystery in the quark model, because it is composed of three quarks up with a paralell spin and this is unacceptable by the Pauli's exclusion principle. In 1965 this problem was solved proposing that the quarks had an extra degree of freedom, latelly called "color charge" and that quarks interact via vector gauge boson octets: the gluons.

Since in QCD a color charged is assigned to each quark, in analogy to the electric charge, the color charged should be conserved during a specific process. A quark could be red, blue, green, anti-red, anti-blue, anti-green, where a compose of hadronic particles are always of neutral color, for example an hadron of neutral color like a meson containing red and anti-red quarks or a baryon with red, blue and green quarks.

When one tries to separate a $\mathrm{q}-\bar{\mathrm{q}}$ pair, due to confinement the strong force will increase as much as we try to separate the two quarks the strong forces increases with the separation distance. This process continues until eventually we put so much energy[7] into the system such that a new $\mathrm{q}-\bar{\mathrm{q}}$ pair is created. Therefore one can not separate the quarks at normal low temperatures, because the strong force is greater enough, this is know as "color confinement" [46]. The quarks are also free in a short distance range, because at very short distance the strong force has a small effect, this is know as "asymptotic freedom" [47], this also happend at high temperatures, in order to see how strong is the interaction a coupling constant needs to be described. A coupling constant [42] g is a number that determines. The strenght of the interaction. In quantum field theory a beta function $\beta(g)$ carries the variation of the coupling constant and is defined by [42, 48]:

$$\beta(g) = \mu\frac{\delta g}{\delta\mu} = \frac{\partial g}{\partial log(\mu)}, \tag{1.3}$$

where $\mu = Q^2$ is the energy scale of a given physical process with transfered momentum Q. As a result, the QCD coupling constant [48] decrease logarithmically at high energies, which can be observed from:

$$\alpha_s(Q^2) = \frac{4\pi}{\beta_0 ln\left(\frac{Q^2}{\Lambda^2_{QCD}}\right)}, \tag{1.4}$$

where Λ_{QCD} (see Fig. 1.2) is the energy scale where the QCD coupling diverge. This behaviour implies two important QCD properties which discovery gave the nobel prize in 2004 to David Politzer [51], David Gross and Frank Wilczek [52]. From the expession 1.4 one can see that at high value of Q^2, the coupling constant becomes very small, this property is the so-called asymptotic freedom. Basically this means that in high energy collisions the quarks can be kicked out but due to confinement they hadronize to form the so-called jets. At low Q^2 the coupling constant diverge, this is called "color confinement" and this is why we never see free quarks or gluons in the nature. Instead of this they form color singlets known as hadrons. Different theoretical approaches are used to describe each of the QCD domains. For small distances (high values of Q^2) perturbatives methods can be applied (pQCD), while phenomenological models are used for processes involving at large distances (small Q^2). The behaviour of the QCD coupling constant is mainly due to the presence of auto-interactions of the gauge bosons. The parameter Λ_{QCD} depends on the normalization frame and the number of active flavors (number of quarks with mass $m_q < Q$). Its value has been determined experimentally and is approximatly of 213 MeV. So the perturbative approximation fails in scales comparable with the mass of the light hadrons ($Q \sim 1$ GeV/c).

---

[7] A classic approximation to this potential is the Yukawa potential and its given by $V(r) = -\frac{g_s}{4\pi r}e^{\frac{mcr}{\hbar}}$, where m is the mass of the interchanged meson and r the separation distance.

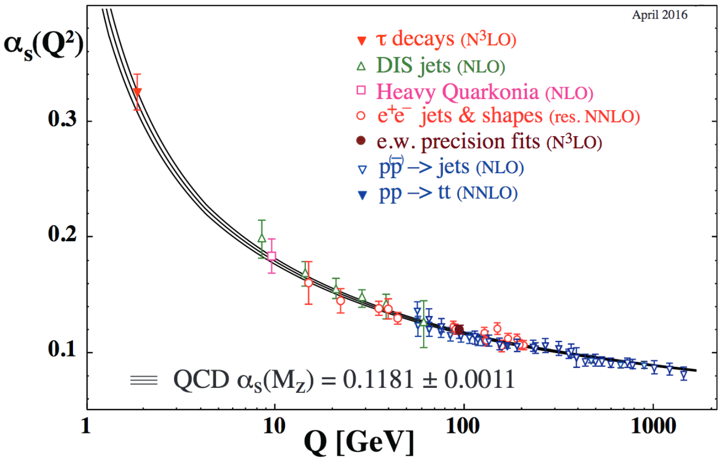

Figure 1.2: Summary of measurements of the QCD coupling constant [42], description of the method for values calculations can be found here: [49, 50].

The QCD theory can be described by an analitic formalism where the lagrangian density with a non abelian gauge group is given by:

$$\mathcal{L}_{QCD} = \mathcal{L}_{fermion} + \mathcal{L}_{YangMills} + \mathcal{L}_{gauge} + \mathcal{L}_{ghost}, \tag{1.5}$$

Where

$$\mathcal{L}_{fermion} = \bar{\psi}^i_q (i\gamma^\mu)(D_\mu)_{ij}\psi^j_q - m_q\bar{\psi}^i_q\psi^i_q \tag{1.6}$$

where ψ^i_q denotes a quark field with colour index i, $\psi_q = (\psi^R_q, \psi^G_q, \psi^B_q)^T$, γ^μ is the Dirac matrix that expresses the vector nature of strong interaction, m_q the mass of the quarks, and D_μ the covariant derivative in QCD given by $(D_{mu})_{ij} = \delta_{ij}\partial_\mu - ig_s t^a_{ij} A^a_\mu$, with $g_s = 4\pi\alpha_s$ the strong coupling constant, A^a_μ the gluon field with colour index a and $t^a_{ij} = \frac{\lambda^a_{ij}}{2}$ proportional to the hermitian traceless Gell-Mann matrices of SU(3). An example of the color flow in a quark gluon interaction can be seen in Fig. 1.3.

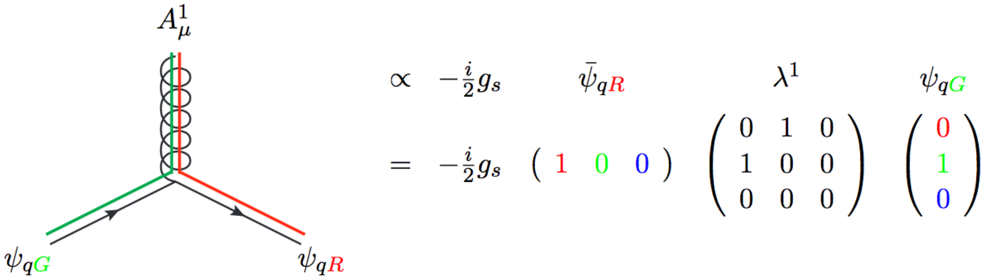

Figure 1.3: Representation of a gluon in a state λ^1 interacting via a qqg vertex with ψ^R_q and ψ^G_q [43].

And the Yang Mills[8] lagrangian density is given by:

$$\mathcal{L}_{YangMills} = -\frac{1}{4} G^i_{\mu\nu} G^{\mu\nu}_i, \tag{1.7}$$

where the gluonic field strenght tensor is given by:

$$G^i_{\mu\nu} = \underbrace{\partial_\mu A^i_\nu - \partial_\nu A^i_\mu}_{Abelian} - \underbrace{g f^{ijk} A^j_\mu A^k_\nu}_{non-Abelian}, \tag{1.8}$$

with $i = 1, 2...8$, f^{ijk} the QCD Lie group coupling structure constants ($SU(3)$) and $A^j_\mu A^k_\nu$ representing its auto-interactions. The commutator of gluon potentials leads to three and four gluon vertices when squared in the Lagrangian with the universal coupling g^2 in the case of the 4-gluon vertex, the main point is that the gluon-gluon vertices are the reason why the strong interaction is short-ranged, even though the force carriers are massless. The gluonic field strength tensor is gauge invariant, where the QCD vacuum expectation value ($\langle G_{\mu\nu} G^{\mu\nu} \rangle$) is given by $\langle g^2 G_{\mu\nu} G^{\mu\nu} \rangle \sim 0.5$ GeV^4. The QCD vacuum is an example of a non perturbative vacuum state characterized by a lot of condensates as the gluon condesate or the quark condensate, which characterize the normal phase or the confined phase of the quark matter.

The gauge fixing lagrangian density [55] ($\mathcal{L}_{gauge}$) and the Faddeev-Popov ghost [56] lagrangian ($\mathcal{L}_{ghost}$) arrives in the quantization and renormalization of QCD. In the renormalization of QCD a scale dependence on the renormalization scale μ_R is introduced, which in perturbative calculations leads to Q^2 (the transfered momentum in the interaction). The QCD lagrangian has color charge conservation, and flavor number conservation which implies electric charge and baryon number conservation[9] ($B = 1/3(n_q - n_{\bar{q}})$, baryons have a baryon number of +1, mesons have a baryon number of 0, and antibaryons have a baryon number of -1).

QCD is very precise for processes involving a large momentum transfer, where perturbative methods can be applied. However, non-perturbative techniques are needed for real precision test of the theory at low energies. Lattice QCD is a non-perturbative QCD technique which is still too far to make reliable predictions for example, for the total pp cross sections. However, it provides quantitative estimates of many physical observables. Furthermore, it lead to the prediction for the behaviour of matter under extreme conditions, the existence of a new phase called Quark-Gluon Plasma. This new form of matter can be produced in the laboratory by means of ultra-relativistic heavy-ion collisions and perhaps, in pp collisions too [15].

---

[8] The Yang-Mills theory was developed in early 1954, by Chen Ning Yang and Robert Mills, where they extended the concept of gauge theory for abelian groups to non-abelian groups to provide an explanation for strong interactions. Yang-Mills theories was included in the Clay Mathematics Institute's list of Millennium Prize Problems. Here the prize-problem consists, especially, in a proof of the conjecture that the lowest excitations of a pure Yang-Mills theory (i.e. without matter fields) have a finite mass-gap with regard to the vacuum state [53, 54]

[9] One exception will ocurre for example in some GUT's theories [57] where are based on protons decay [58] which has not been observed [59] as today due to its large timelife ($> 10^{34}$).

1.3 Ultra-Relativistic Heavy Ion Collisions a mini Big-Bang

Matter as we know, is made up from molecules which consist of atoms which consist of electrons circling around a nucleus, which also consist of protons and neutrons which themselves are bound states of quarks and gluons; has not existed forever. Our Universe originated in a Big Bang from a state of almost infinite energy density and temperature. During the first few microseconds of its life the energy density in our Universe was so high that hadrons (color singlet bound states of quarks, antiquarks and gluons) such as, the nucleons inside a nucleus, could not form. Instead, the quarks, antiquarks and gluons were deconfined and permeated the entire Universe in a thermalized state known as quark-gluon plasma (QGP explained in Appendix B). Only when the energy density of the Universe dropped below the colored degrees of freedom became confined into color singlet objects of about 1 fm diameter: the first hadrons were formed. After the Universe hadronized, it took another 200 seconds or so, until its temperature dropped below 100 keV [75] such that small atomic nuclei could form and survive. This is known as primordial nucleo-synthesis. At this point (i.e. after "the First 3 Minutes") the chemical composition of the early Universe was fixed ("chemical freeze-out" [75, 80]). All unstable hadrons had decayed and all antiparticles had annihilated, leaving only a small fraction of excess protons, neutrons and electrons, with all surviving neutrons bounded inside small atomic nuclei. The chemical composition of the Universe began to change again, only several hundred million years later, when the cores of the first stars ignited and nuclear fusion processes were set in. The only other surviving feature of the Big Bang is the ongoing Hubble expansion of our Universe, and the structure of its density fluctuations, amplified over eons by the action of gravity and reflected in today's distribution of stars, galaxies, galactic and supergalactic clusters, and dark matter. Using the observational pillars (today's expansion rate or "Hubble constant", the microwave background spectrum and its fluctuations, the primordial nuclear abundances and, most recently, also today's spectrum of density fluctuations) together with the equations of motion of general relativity, we have been able to reconstruct the cosmological evolution of our Universe from its origin in the Big Bang. However, try as you want, we will never be able to directly see anything that happened before 300 000 years after the Big Bang, due to the opacity of the Early Universe, the only way its to try to reproduce those conditions by colliding heavy nuclei.

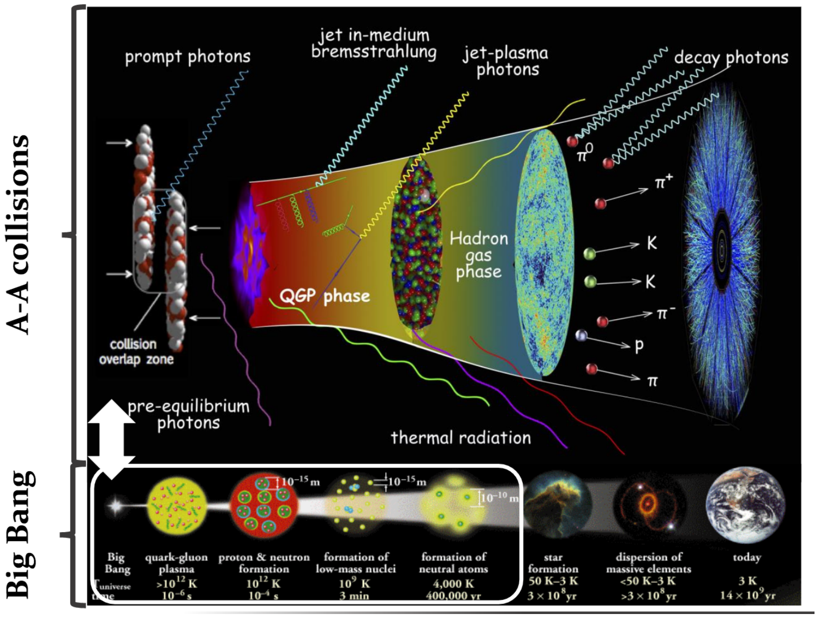

Figure 1.4: Comparison between a heavy ion collision and the early universe formation in the Big Bang.

Heavy-ion collisions have been studied at several accelerators with different energies which has provided results of measurements at different values of temperature and baryon chemical potential, to which study requires a model for the collisions. Over the years several models have been developed (Fermi statistical model [69], Pomeranchuk model [70] Landau model [71], Hagerdorn model [72, 73]), but today the approach proposed by Bjorken [74] is commonly used. A heavy-ion collision is a highly-dynamical event. The evolution of the collision is pictorially represented in Fig.1.5 in a light cone where the system is expanding under pressure gradients and cools down as time evolves. One can identify, schematically, the five following stages [75, 8, 9]:

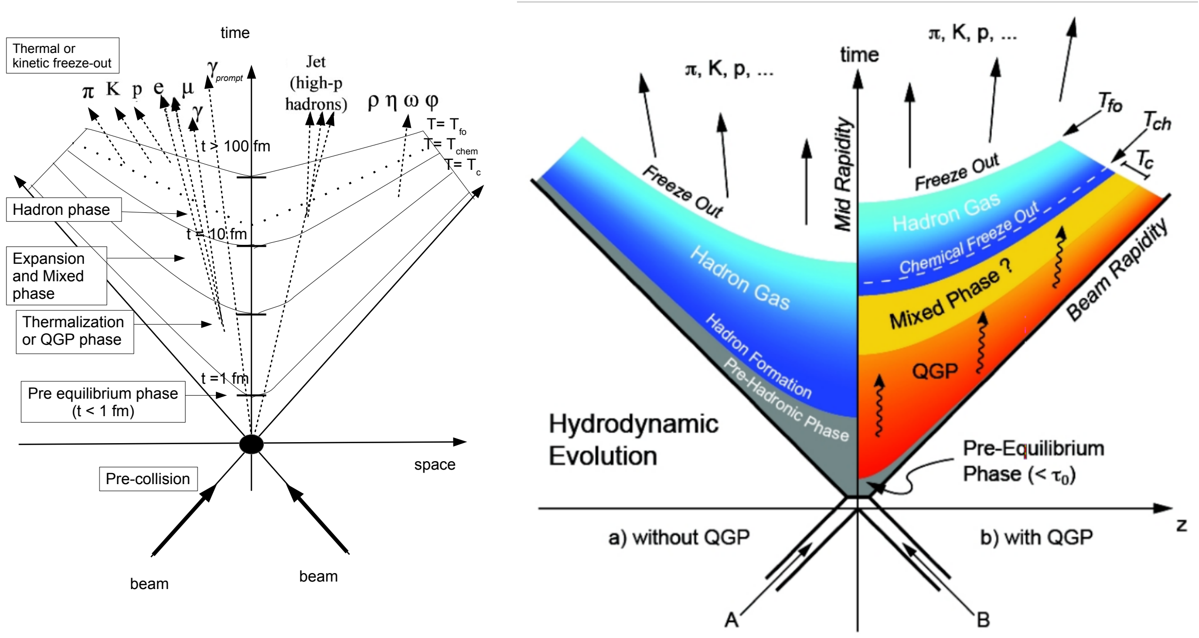

Figure 1.5: left) Illustration of the evolution phases of an ultrarelativistic heavy-ion collision, right) comparison of the hydrodynamical evolution without and with QGP.

Pre-equilibrium ($t \lesssim 1$ fm/c), this ocurrs inmediatly after the initial collisions during the passage time of the nuclei ($t_{cross} = 2R/\gamma_{cm}c \approx 10^{-2}$ fm)[10]. High transverse momentum particles ($p_T \gg 1$ GeV/c) are produced at this stage. A large quantity of photons is also produced, *direct photons* (which can be seen at the end and carry thermal information of the initial collision), real or virtual photons that decay in lepton-antilepton pairs.

Thermalization ($t \sim 1 - 10$ fm/c), where the partons created in the primary collisions between the incoming nucleons can't right away escape into the surrounding vacuum, but they can rescatter of each other. In this way they create a form of dense, strongly interacting matter which, when it thermalizes quickly enough and at sufficiently large energy density, this is the quark-gluon plasma or the so-called "fireball". Here the inelastic interactions can modify the flavour composition of particles. If the reaction zone thermalizes at energy density $> e_{cr}$ such that gluons are deconfined and chiral symmetry is restored, leading to chemical equilibration between light and strange quarks ($m_s \approx 150$ MeV). The observed strangeness suppression in pp collisions should thus, be reduced or absent in relativistic heavy-ion collisions.

A thermalized system has thermal pressure which, when acting against the surrounding vacuum, leads to collective (hydrodynamic) expansion of the collision fireball. Due to its internal pressure, the system at thermal

---

[10] which is much smaller than the typical timescale of the strong interaction $t_{strong} \approx 1/\Lambda_{QCD} \approx 1$ fm. We also note, that the crossing time t_{cross} as well as t_{strong} are much smaller than the transverse size of the nucleus [76].

equilibrium rapidly expands.

Expansion and Mixed phase, while expanding, the system begins to convert into hadron gas, (this is why is a mixed phase between QGP and hadrons formation).

Hadronization ($t \sim 20$ fm/c), this is where fragmentation or coalescense take place. When it reaches again the critical energy density, the hadronization begins and quarks and gluons of the QGP matter interact among themselves until the interaction rate can no more substain the QGP expansion and they condensate in new hadrons. Here also the **chemical freeze-out** take place, where inelastic collisions cease at a chemical freeze-out temperature ($T_{ch} \sim 160$ MeV[11]), at this point the flavour composition of the QGP matter is fixed.

Thermal or kinetic freeze-out, this occurs when the mean distance between the hadrons becomes greater than the radius of strong interaction (at $T \sim 120$ MeV), due to this, elastic collisions cease and the correlations and momentum spectra remain fixed, these particles yields can be described by an hydrodynamic motivate blast wave model, where it's assumed that particles are locally thermalized at a kinetic freeze-out temperature moving with a collective common transverse radial flow velocity.

The challenge is to characterize the hot (deconfined) stage iii), called early-on "fireball", while most of the measurements are performed via hadrons (or their decay products) carrying primarily information from the system at stages iv) and v). Some probes o the formation of QGP are: the transverse collective radial and anisotropic flow, the strangeness enhancement, the radiation of the plasma as the measurement of direct photons, the restoration of chiral symmetry, the formation of vector mesons in dense matter, the quarkonia suppression, the evidence for deconfinement or dynamical ionization [173].

1.4 Hadron-hadron interactions

The protons not only consist of valence quarks, also of a "sea" of quarks and gluons that are constantly producing or anihilating. Each of these partons (quarks and gluons within proton) carry a fraction of total energy of an hadron. In fact the collisions at high energy are not between protons but between partons. The functions that describe the probability to find a parton carrying a fraction x of the longitudinal momentum of the hadron energy are the parton distribution functions (PDF's by acronym). The inelastic cross section of the collisions between hadrons is dominated for a "soft" component, which means that just a small fraction of momentum is trasfered to form new particles. Nevertheless, sometimes a "hard" scattering could take place. In this case, there are high transverse momentum partons created in the collisions. This partons radiate soft gluons creating the so-called partonic showers. The probability that a gluon with a momentum k and transverse momentum k_T to be emmited for a quark with momentum p is [60]:

$$d\omega^{q\to q+g} = 2C_F \frac{\alpha_s(k_T)}{4\pi}[1+(1-\frac{k}{p})^2]\frac{dk}{k}\frac{dk_T^2}{k_T^2}, \tag{1.9}$$

where

$$\alpha_s(k_T) = \frac{2\pi}{\beta_0} ln(\frac{k_T}{\Lambda}), \tag{1.10}$$

C_F is the Casimir factor, in this case its value is 4/3. It is easy to see that the jet evolution is determined by the soft and colinear gluon emission [60], this is, $\omega \sim \alpha_s ln^2 p$ always that $k \ll p$. The emission of a parton at a big angle is also possible, however it's suppressed by $\omega \sim \alpha_s/\pi \ll 1$ when $k \sim p$. In practice we can't see the parton shower (final stage particles), this is what we say that it is a process at a "partonic level". Due to the color confinement, the partons in the shower has to hadronize. A jet is a collimated hadrons cone and other particles produced by the hadronization procedure from a quark or a gluon. The particle content in an event after the hadronization is refered to "hadronic level". The hadronization is described by the fragmentation functions (FF) these are relevant for all collision system.

---

[11] Similar to lattice QCD calculations of the cross-over temperature, this can be understood considering that the freeze-out temperature is not related to kinetic processes and hadronization should be universal [77], also see 5.

Intuitively we can think that the inclusive production process of an hadron could be predicted, if first; we calculate the process equivalent at partonic level (this means, replazing the produced hadron by a final parton and the inclusive sum over all the final hadrons by final partons), then allowing this to hadronize.
The general description of the final stage hadron production it's obtained by mean of the QCD factorization theorem [61, 62], which can be summarized as:

$$\frac{d\sigma}{dX} = \sum_{j,k} \int_{\hat{X}} f_j(x_1, Q_i) f_k(x_1, Q_i) \frac{d\hat{\sigma}_{jk}(Q_i, Q_j)}{d\hat{X}} D_l^h(X, Q_l^{'}) \tag{1.11}$$

Note that the factorization theorem is separated in two parts: the partonic cross section $\left(\frac{d\hat{\sigma}_{jk}(Q_i,Q_j)}{d\hat{X}}\right)$, that incorporates the short range process that are calculables in pQCD, and the universal functions that describe the non perturbative process, the parton distribution functions (PDFs) denoted as $f_j(x_1, Q_i)$ and the fragmentation functions (FFs) denoted as $D_l^h(X, Q_l^{'})$, to know more about it see Appendix C. The hard part of the process it's well described by pQCD, however the particle production at low momentum can be very difficult described by an analogous theory to QCD, rather than this, phenomenological models are used to describe some particular experimental measurements, but they fail in other measurements. This enviroment so complex that an understanding of the hard processes is needed as better as possible.

1.4.1 Event Shapes at hadron colliders

The event shape analysis (ESA) [12, 13] is used to study the geometrical properties (in the phase space) and characterize the distribution of the outgoing particle energy flow from a high energy collision. These variables are useful for:

1. In hadronic collisions they allow to measure events with hard (jets) and soft (no jets) components [88].
2. In e^+e^- collisions were used to suport the existence of jets and then for the discovery of the gluon [89, 90].
3. It can be useful to discriminate physics as SUSY from extradimentions [91].

Some Event Shape [12, 92, 21] in hadron collisions are:

- Transverse Sphericity (S_{T}),
- Transverse Spherocity (S_{O}),
- Thrust (T),
- Thrust-Minor (T_{min}),
- many other as: aplanarity, circularity and so on.

These quantities are defined in the transverse plane of the phase space in terms of p_{T} (Lorentz invariant) these are also Infra-red Safe and collinear safe.

Sphericity (S) and Transverse Sphericity (S_{T}).

The momentum tensor is one analog to the inertia tensor, this was introduced by J.D. Björken and S.J. Brodsky [98] as [99]:

$$T^{ab} = \sum_i \left(\delta^{ab} p_i^2 - p_i^a p_i^b\right). \tag{1.12}$$

If this tensor is diagonalized we get the eigenvalues λ_1,λ_2 and λ_3, which are the sum of the square of the transverse momenta with respect to the directions of the 3 eigenvectors. The smallest eigenvalue (λ_3) is the minimum of the sum of the squared transverse momentum. The eigenvector asociated with λ_3 is defined as the axis of the reconstructed jet. To determine how similar are the events to a dijet structure, we calculate the quantity called sphericity (S) given by [100]:

$$S = \frac{3\lambda_3}{\lambda_1 + \lambda_2 + \lambda_3} = \min\left(\frac{3}{2}\frac{\sum_i p_{i\ \mathrm{T}}^2}{\sum_i p_i^2}\right) \tag{1.13}$$

In e^+e^- collisions the axis of sphericity is taken in the direction of the original pairs $q\bar{q}$ and this definition is valid for hadron-hadron collisions. In hadronic collisions the transverse sphericity (S_{T}) [92], is defined in terms of the eigenvalues ($\lambda_1 \geq \lambda_2$) of the linearized transverse momentum tensor:

$$S^L_{x,y} = \frac{1}{\sum_i p_{\ \mathrm{T}i}} \sum_i \frac{1}{p_{\mathrm{T}i}} \begin{pmatrix} p_{xi}^2 & p_{xi}p_{yi} \\ p_{yi}p_{xi} & p_{yi}^2 \end{pmatrix} \tag{1.14}$$

and it's defined as: $S_{\mathrm{T}} = \frac{2\lambda_2}{\lambda_1+\lambda_2}$, thus, the sphericity has the limit values (see Fig. 1.6):

$$S_{\mathrm{T}} = \begin{cases} 1 \text{ isotropic structure} \\ 0 \text{ dijet structure} \end{cases} \tag{1.15}$$

Transverse spherocity (S_O).

Transverse spherocity is an event shape which is defined as [12, 18, 16, 13, 32, 33]:

$$S_{\mathrm{T}}^{pherocity} = \frac{\pi^2}{4} \underset{\vec{n}=(n_x,n_y,0)}{min} \left(\frac{\sum_i |\vec{p}_{\mathrm{T}i} \times \vec{n}|}{\sum_i |\vec{p}_{\mathrm{T}i}|}\right)^2 \tag{1.16}$$

where the limits values of this variable are:

$$S_o = S_{\mathrm{T}}^{pherocity} = \begin{cases} 1 \text{ isotropic structure} \\ 0 \text{ jetty structure} \end{cases} \tag{1.17}$$

For more details of spherocity selection in data, you can see the section 5.3.1. Some examples for isotropic and jetty events can be seen in next figure.

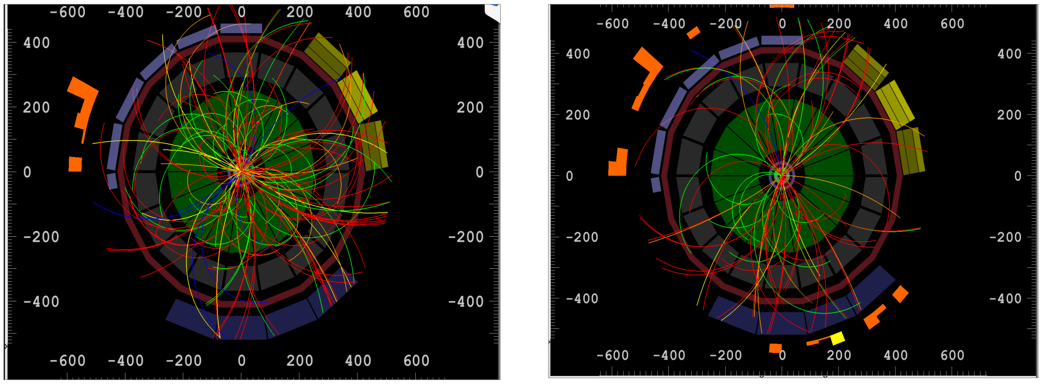

Figure 1.6: Events with different event topologies: a) isotropic (Run 225050 event 564, $S_O > 0.9$ Nch=158) and, b) dijet event (Run 225035 event 189, $S_O < 0.01$ Nch=86).

1.4.2 Monte Carlo event generators models

The complexity of the hadron-hadron collisions at high energy requires also complex models that can explain the processes behind the behaviour of the measured observables, due to this; the models are formulated via MC event generators. The MC generators need to simulate events similar to that in real interactions. Usually the event generators combine the information from pQCD, and some phenomenological approximation for no pQCD to simulate the soft components of the collisions (underlying events [17], low p_{T} particle producction, etc). In this work we use the generators Pythia 6 [109], Pythia 8 [22] and Epos 3 [101]

Epos

Epos [101, 102] is a Monte Carlo event generator which takes a Parton-Based Gribov Regge Theory approach for the event generation. For high string densities, e.g. achieved in high-multiplicity pp collisions, the model does not allow the strings to decay independently, instead, if energy density from string segments is high enough they fuse into the so-called "core" region, which evolves hydrodynamically. On the other hand, the low energy density region forms the "corona" which hadronizes using the unmodified string fragmentation.

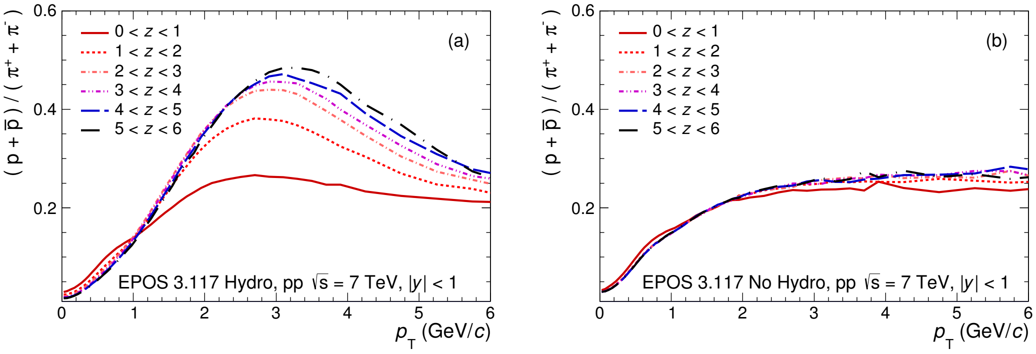

Figure 1.7: (Color online) Proton-to-pion ratio as a function of p_{T} for different multiplicity event classes. Results for pp collisions at $\sqrt{s} = 7\,\mathrm{TeV}$ generated with Epos are presented. The ratios are displayed for simulations (a) with and (b) without the hydrodynamical evolution of the system.

The “core” region originates around 30% of the central particle production for an average pp collision at $\sqrt{s} = 7\,\mathrm{TeV}$, $\langle \mathrm{d}N_{\mathrm{ch}}/\mathrm{d}\eta\rangle_{|\eta|<2.4} \approx 6.25$. This fraction might reach $\approx 75\%$ for $\langle \mathrm{d}N_{\mathrm{ch}}/\mathrm{d}\eta\rangle_{|\eta|<2.4} \approx 20.8$ [107]. Concerning the hard component, the inclusive jet cross section for pp collisions at $\sqrt{s} = 0.2\,\mathrm{TeV}$ obtained with Epos 3 agrees within 5% and 4% with STAR data and NLO pQCD calculations, respectively [103]. Therefore, an analysis in Epos as a function of event multiplicity and leading jet transverse momentum makes sense.

To illustrate the effect of hydrodynamics on flow observables, Fig. 1.7 shows the proton-to-pion ratio as a function of p_{T} for different multiplicity classes. Results are presented in intervals of z, defined as

$$z = \frac{\mathrm{d}N_{\mathrm{ch}}/\mathrm{d}\eta}{\langle \mathrm{d}N_{\mathrm{ch}}/\mathrm{d}\eta\rangle}\ , \tag{1.18}$$

where $\langle \mathrm{d}N_{\mathrm{ch}}/\mathrm{d}\eta\rangle$ is the average mid-rapidity particle density for minimum bias pp collisions at $\sqrt{s} = 7\,\mathrm{TeV}$. Fig. 1.7 a) shows the case when hydrodynamics is considered in the simulations. In this case, a clear evolution of the particle ratio with z can be observed, e.g. going from the lowest z to the highest z values the particle ratios exhibit a depletion (enhancement) for the transverse momentum interval $p_{\mathrm{T}} < 1\,\mathrm{GeV}/c$ ($1 < p_{\mathrm{T}} < 6\,\mathrm{GeV}/c$). This feature is usually attributed to radial flow which modifies the spectral shapes of the p_{T} distribution depending on the hadron mass. On the contrary, Fig. 1.7 b) shows the case without hydrodynamics, where the particle ratios do not evolve with multiplicity. It is worth noticing that similar effects are observed in Pythia, but in that case the radial flow-like behavior is attributed to color reconnection [24].

Pythia and its tunes

Pythia [109] is an event generator that combines phenomenological models motivated mainly by pQCD. The pp cross section used in Pythia is described by the 1992 Donnachie-Landshoff parametrization [22]:

$$\sigma_{\ \mathrm{pp}}(s) = 21.70 s^{0.0808} + 56.08 s^{-0.4525}, \tag{1.19}$$

where the first terms comes from the Pomeron exchange, the second is from the Reggeon exchange, the constants are found from fits to the measured data. Also the total cross section includes different partial cross sections as shown in next equation.

$$\sigma^{tot}_{\mathrm{pp}} = \sigma^{el}_{\mathrm{pp}} + \sigma^{SD}_{\mathrm{pp}} + \sigma^{DD}_{\mathrm{pp}} + \sigma^{ND}_{\mathrm{pp}}. \tag{1.20}$$

The optical theorem is adopted to obtain the elastic contribution ($\sigma^{el}_{\mathrm{pp}}$) and the calculated expressions by Regge theory determine the diffractive cross section ($\sigma^{SD}_{\mathrm{pp}}$ and $\sigma^{DD}_{\mathrm{pp}}$). A diffractive event is such that in which one (or both) projectiles stay intact(s). In the events without diffraction there are the partonic interactions with low transfered momentum. In collisions with one diffraction, just one of the particles from the beam is divided and produces particles with high rapidity in just one side. In a collision with doble diffraction both beams are divided and produce particles at high rapidity values (positive and negative) with a gap in the central region. The remanents cross sections are $\sigma^{ND}_{\mathrm{pp}}$. In the features of this class of events, the pseudorapidity particle distribution shows that the no diffractive processes have many particles in the central region and then fall as the rapidity increases.

Pythia defines the hard interactions as the interactions with a transfered momentum greater than the p_{Tmin}. Thus, by construction, all the no diffractive events correspond to the semi-hard interactions. Due to the nature of quantum mechanics, the first step in the event generation process is random in the simulation process. The selection is drived by the previous cross sections mentioned. The next step depends on the type of the selected process. For the case of a hard interaction the procedure is the next:

- Two particles beams move one to each other. Every of this consist of several partons (quarks, antiquarks and gluons) which distribution can be characterized by parton distribution functions such as the described in the QCD factorization theorem. Several parameters exist: thus, the generated events also depend on the PDF election. The default value for PDF is CTEQ5L. This parametrization result from a global fit for lepton-hadron and hadron-hadron measurements at high energies.

- Partons of each of the beams could be fragmented before the interaction (e.g. $q \rightarrow qg$), this is called the initial cascade.
- The hard interaction (e.g. $qg \rightarrow qg$ or $qg \rightarrow q\gamma$) ocurres between two partons and produces particles. In this process could appear short live resonances (e.g Z^0) which decay have been considered by the event generator. The total interaction cross section (σ_{int}) which is found by integrating the differenctial cross section (given by the factorization theorem) with respect to p_{Tmin}. The σ_{int} could be greater than σ_{ND}, which is interpreted as multiparton interactions. Thus the average number of parton-parton interactions by event is directly given by the ratio of the cross sections.

$$N_{parton-parton} = \frac{\sigma_{int}}{\sigma_{ND}}. \tag{1.21}$$

- Simultaneusly to the hard process, or the semi-hard processes could happen between two partons.
- After the interaction the resultant partons could fragment which is refered as the final state cascade. This process becames important to high energies and its realization has a significant influence in the jet structure. Pythia uses the parton cascade approximation. The partons are subject to a branching series, e.g. $q \rightarrow qg$, $q \rightarrow q\gamma$, and $g \rightarrow gg$. Each one is described by a branching kernel P(z) where z denotes the energy and transfered momentum to the two products. This kernel approximations of the matrix element that describes the branching process (in the logarithmic square doesn't contain terms $\mathcal{O}(\alpha_s^2)$). The proceeding is initiated with an energy that match the hard interaction ends when the remanent energy is below the threshold of 1 GeV.
- The QCD-strings are extended over the produced quarks and gluons that subsecuently are fragmented to hadrons without color due to the QCD confinement. The strings topology are in principle found by break down of the QCD basis cross sections in defined color states. The fragmentation process (some times at the final state called hadronization) is not understood by first principles. So then, phenomenological approximations are used; Pythia implements the so-called "Lund string model". An example of the fragmentation process in the Lund model is of the type: string→ hadron + remanent string. The string stretches between for example a q and $\bar{q}$; while the quarks move far away, the potential energy in the string increases due to confinement that kept connected. If the energy its big enough, the strings break producing an additional pair $q\bar{q}$. The two resultant strings ($q - \bar{q}^{'}$ and $q^{'} - \bar{q}$) continues spliting. If the energy of a pair is low enough, a meson is formed. In an analog way, a pair diquark-antidiquark can be created when a string is broken.
- The produced hadrons in the previous case can be inestables and they can decay. Pythia contains a list of properties of the decays (branching fractions, decay products, life times) of relevant inestables particles. Also there exist a significative amount of experimental data in the decay properties, the information of a lot of particles still incomplete, specifically for charm and bottom mesons. This became uncertain in the events properties.

Perugia2011 tune

In Pythia 6 [21] some updates that has been prepared during the spring of 2011, these are the Perugia tunes[12],which include the following features [108]:

---

[12] Name derived from Perugia MPI Workshop [108]

1. Use the same value of Λ_{QCD} for all shower activity (ISR and FSR), in particular to simplify matching applications. Due to a slightly increased level of soft ISR, the Perugia 2011 tunes only need 1 GeV of primordial k_T to describe the CDF and D0 Drell-Yan p_T spectra, as compared to 2 GeV in the previous tunes.

2. Take into account some of the early lessons of LHC minimum bias and underlying event data at 900 and 7000 GeV.

    (a) Faster scaling of multiplicities with energy, motivated, e.g., by the ALICE and ATLAS min-bias charged multiplicity measurements.

    (b) Increased baryon production, especially of strange baryon s (larger Λ/K ratio), motivated by identified particle measurements by the ALICE and CMS experiments and by the p/π ratio measured by STAR. The total amount of baryon production (dominated by protons and neutrons) now appears to be at the upper limit of the range allowed by LEP.

    (c) The default suppression of strangeness in association with popcorn mesons was removed to help improve Ξ and Ω yields at LEP.

Monash2013 tune

Pythia 8 [22] is a full event generator for pp collisions. For inelastic collisions, which is the main interest here, each collision is modelled via one or more parton-parton interactions. The full calculation involves leading-order (LO) pQCD $2 \rightarrow 2$ matrix elements, complemented with initial and final-state parton radiation, multiple particle interactions, beam remnants and the Lund string fragmentation model. Pythia 8 also has strong final-state parton interactions (implemented through the CR models [22]). In this work we use the Monash 2013 tune [23] which has as default parametrisation the so-called MPI-based model of color reconnection. Such model allows partons of each MPI system to form their own structure in color space and then, they are merged into the color structure of a higher p_{T} MPI system, with a probability $\mathcal{P}$ given by:

$$\mathcal{P}(p_{\mathrm{T}}) = \frac{(R \times p_{\mathrm{T0}})^2}{(R \times p_{\mathrm{T0}})^2 + p_{\mathrm{T}}^2} \ , \tag{1.22}$$

were R is the reconnection range ($0 \leq R \leq 10$) and p_{T0} is the energy dependent parameter used to damp the low-p_{T} divergence of the $2 \rightarrow 2$ QCD cross section.

To illustrate how the Monash 2013 tune describes the data, Fig. 1.8 a) shows the proton-to-pion and the kaon-to-pion ratios for inelastic pp collisions at $\sqrt{s} = 7\,\mathrm{TeV}$. As discussed in [24], the model shows a qualitative agreement with data, e.g., the bump in the proton-to-pion ratio, though the size of the effect is underestimated. The same level of accuracy is achieved by Epos 3 which according to Fig. 1.8 b) overestimates the effect when hydrodynamics is included. So, in the end we will compare models which still do not fully describe the data, but this does not matter for our purposes. Because, we want to study differences attributed to the fundamental underlying physics mechanisms which produce the observed radial flow effects.

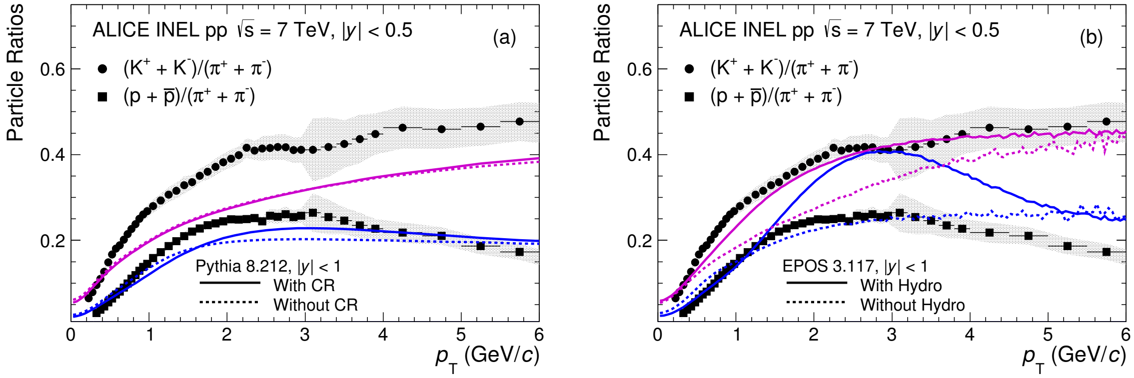

Figure 1.8: (Color online) Proton-to-pion ratio as a function of p_{T} for inelastic pp collisions at $\sqrt{s} = 7\,\mathrm{TeV}$ measured by the ALICE Collaboration [185]. Results are compared to models carried out (a) with Pythia 8 and (b) Epos 3 event generators. Cases with and without the effect of color reconnection and hydrodynamics are plotted as solid and dashed lines, respectively

Chapter 2

ALICE experiment

> .. We are just doing what you have done by following the rabbit ... satisfying human curiosity ... From our results, we can learn for example how the matter of the early universe evolved. We? But who is we? ...
>
> from a 2004 ALICE cartoon

The Large Hadron Collider, in the European Center For Nuclear Research [110] (CERN, for the french acronym of Conseil Européen pour la Recherche Nucléaire) is the greater particle accelerator built in the world until now[1]. The first meeting that drived to the beginning of the project was in 1984. The LHC project was approved in 1994 and the construction of the underground tunnel started in 2001, after the dismantling of the LEP collider which was previously built under the french-swiss border, in an area near to Geneva (see Fig. 2.1) at 50 to 175 m deep, and having 27 km of cincunference. The LHC has reached the greatest center-of-mass energies registered until now ($\sqrt{s}$ = 13 TeV and $\sqrt{s}_{\rm NN}$ = 5.02 TeV for pp and Pb-Pb collisions, respectively). This complex machine is divided in 8 octants (refered as "points") (see Fig. 2.1):

- Point 1: ATLAS [112] experiment (acronym of A Toroidal LHC ApparatuS) studies Higgs physics and Beyond Standar Model, supersymmetry and extra-dimentions searches.
- Point 2: ALICE [6, 7, 111] (acronym of A Large Ion Collider Experiment) which studies strong interactions and Quark Gluon Plasma (QGP) physics.
- Point 3: Beam cleaning and collimation system.
- Point 4: Radiofrecuency systems the protons and heavy nuclei.
- Point 5: CMS experiment [113] (acronym of Compact Muon Solenoid) with similar goals than ATLAS but with a different detector and different technique.
- Point 6: Beam dump system.
- Point 7: Beam cleaning and collimation system.
- Point 8: LHC-b experiment [114] (acronym of the Large Hadron Collider beauty experiment) which studies CP symmetry violation processes in systems with b quarks.

---

[1] Up to 2017, other projects are ongoing as the FCC (Future Circular Collider) CEPC (Circular Electron Positron Collider) to be build in China

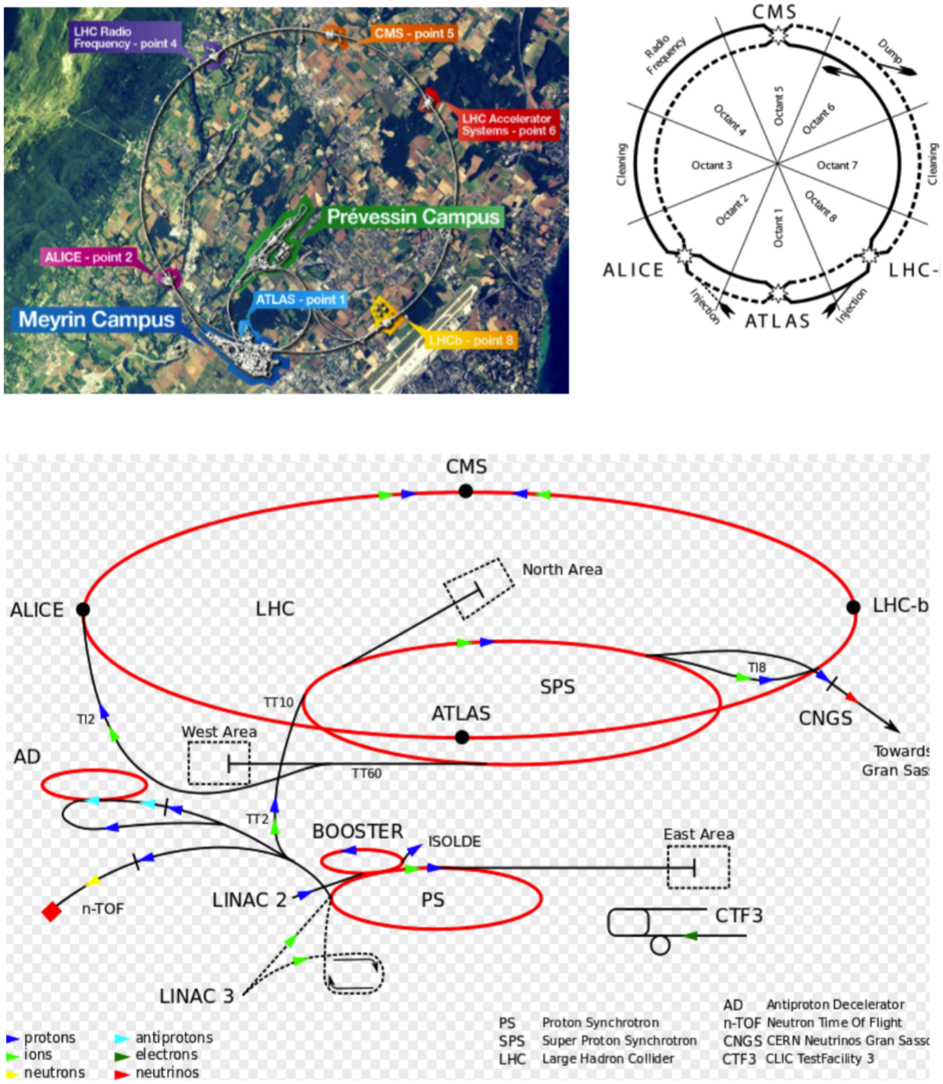

Figure 2.1: a) Different experiments at CERN, b) LHC schematical view, c) LHC aceleration systems map.)

2.1 The ALICE experiment at LHC

ALICE [6, 7, 111](A Large Ion Collider Experiment) is one of the four main LHC experiments, which main porpouse is to study heavy-ion collisions where QGP is formed. ALICE is a massive experiment, built by a collaboration of more than 1800 scientists of 174 institutions of 42 countries. The experiment is 10 000 tons of weight and has a volume of 16m× 16m× 26m= 6656 m^3. The detector is located in a cavern 56 m under ground close to the village of St. Genis-Pouilly in France. The experiment has 19 subdetectors (see Fig 2.2), which can be classified in three subgroups:

1. **Central barrel detectors**. These are located inside the external magnet with a 0.5 T magnetic field. They are mainly dedicated to vertex reconstruction, tracking, particle identification and momentum measurements.
   - From the interaction point and going outward in the central rapidity ($|\eta| < 0.9$) region:
     - Inner Tracking System (ITS), which consists of 3 subdetectors (SSD, SPD and SDD) [115]
     - Time Projection Chamber (TPC) [116]
     - Transition Radiation Detector (TRD) [117]
     - Time Of Flight (TOF) [118]
   - In the mid-rapidity region the following detectors can be found:
     - High Momentum Particle Identification Detector (HMPID) [119]
     - PHOton Spectrometer (PHOS) [120]
     - ElectroMagnetic CALorimeter (EMCAL) [121]
     - Dijet Calorimeter (DCAL) [122]
2. **Forward detectors** These are located at high pseudo-rapidity, i.e., small angles with respect to the beam pipe. They complete the central detection system, characterize the event and provide the interaction trigger. Besides, they are mainly dedicated for triggering. They are:
   - Time Zero detector (T0) [123]
   - VZERO [124], that is made of two scintillator counters arrays, VZERO-A[2] and VZERO-C[3]
   - ALICE Diffractive detector (AD0) [125, 126]
   - Muon Forward Tracker (MFT) [128]
   - Forward Multiplicity Detector (FMD) [123]
   - Photon Multiplicity Detector (PMD) [127]
   - Muon spectrometer [129, 130, 131]
   - Zero Degree Calorimeter (ZDC) [132]
3. **Cosmic Ray detector** A COsmic Ray DEtector (ACORDE),[4] this detector consit on 60 scintillator modules located on top of the ALICE experiment, it provides the information of cosmic ray muons reconstructed also in the TPC, whose primary energies are greater than 10^{14} eV.

---

[2] See 4

[3] VZERO-C detector was developed by the Lyon group from France

[4] The ALICE's Mexican group, was responsible for, not only the design and construction, but also the operation of V0A, AD0 and ACORDE detectors

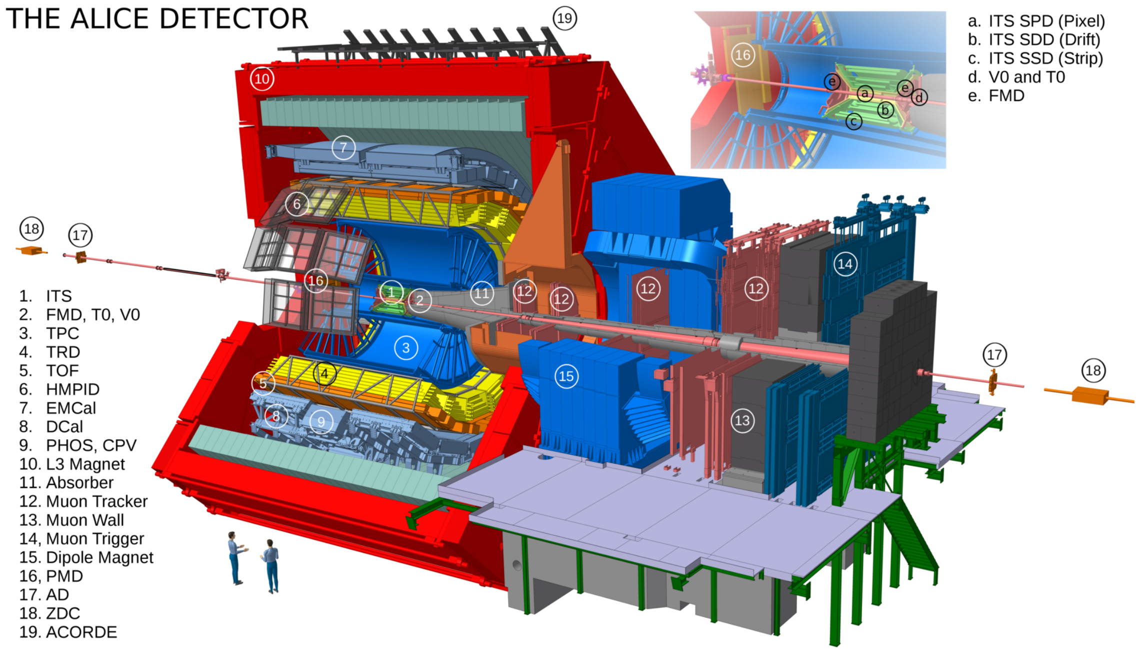

Figure 2.2: Subdetectors system for ALICE used in RUN 2.

For our analysis we used bassically four detectors, this are V0, ITS, TPC and TOF, a full description of these detectors is done in the next sections.

2.1.1 VZERO detector

The VZERO detector [111, 124, 123] has the capability to measure the charge signal and the leading time (pulse time) [124], due to this fact the important roles of the V0 detector are:

- To be part of the minimum bias and the high multiplicity triggers for the central barrel detectors.
- It is a centrality indicator and reaction plane of Pb-Pb collisions.
- It is used for luminosity measurement.
- It is used to reject background induced by beam-gas collisions (see Fig. 2.3), using the crossing time of the tracks at the vertical plane $z = 0$ [124].

This detector is made of two circular scintillator arrays (see Fig. 2.4), VZERO-A and VZERO-C located asymmetrically in the forward and backward directions with respect to the interaction point, these are connected to Hamamatsu photomultipliers through WLS[5] and clear fibers on A and C sides. They cover the pseudorapidity ranges $2.8 < \eta < 5.1$ and $-3.7 < \eta < -1.7$, respectively.

The VZERO-A is located 340 cm from the vertex, on the opposite side to the muon spectrometer. The VZERO-C is fixed at the front face of the front absorber, 90 cm from the vertex. Hence, measuring the leading time difference between two detectors located on each side of the interaction point will enable to identify background events, that is particularly important in pp high multiplicity events. Both of them are segmented into 32 elementary counters distributed in four rings, which are divided into eight sectors of 45 degrees. The elementary counter consists of scintillator material with embedded Wave Length Shifting (WLS) fibers.

---

[5] Abreviation of Wave Lenght Shifters

The time resolutions are about 450 ps and 350 ps, whose are achieved by VZERO-A and VZERO-C arrays, respectively. Indeed, VZERO system allows the rejection of events, as it was said in the beginning of this section, coming from beam-induced background

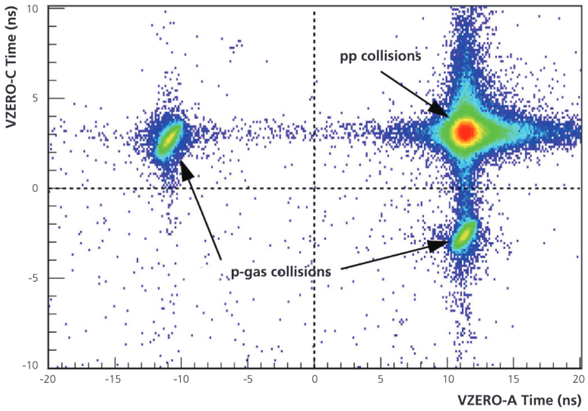

Figure 2.3: Illustration of beam-beam and beam-gas events, that can be discriminated on timming criteria.

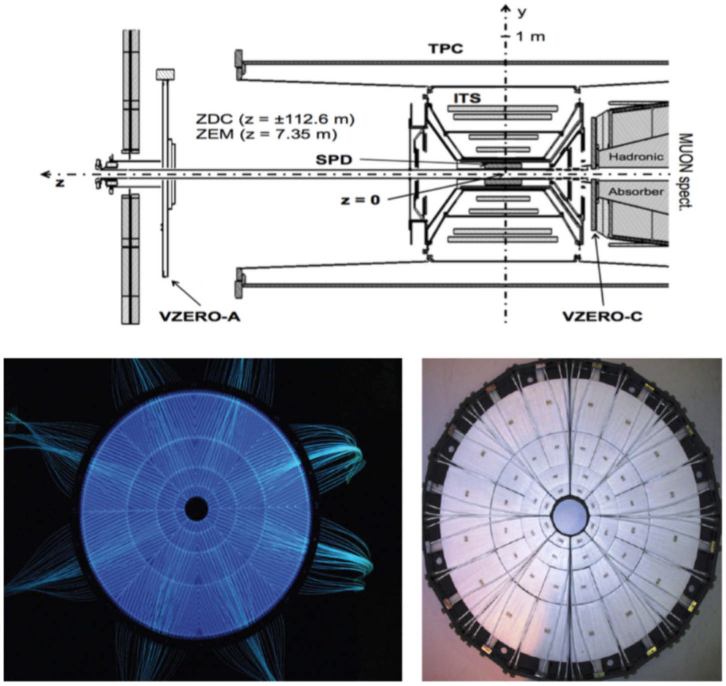

Figure 2.4: VZERO detector schematics (upper) and photo of VZERO-C (lower left) and VZERO-A (lower right).

2.1.2 Inner Tracking System

The Inner Tracking System [111, 115] (ITS, by acronym) consists of 6 layers of silicon detectors located at a radii between 3.9 and 43 cm (see Fig 2.5) and that are coaxial to the beam pipe. Its main tasks are: locate and reconstruct the primary vertex with a resolution better than 100 μm, to reconstruct the secondary vertex of decays from hyperons and D or B mesons, to track and identify particles with 200 MeV/c $> p_{\mathrm{T}} \geq 35$ MeV/c, to get a better angular resolution and momentum for particles reconstructed at the TPC and to reconstruct particles that go in to the dead zones of the TPC. There are three subdetectors implemented in the ITS, these are described as follows.

Silicon Pixel Detector (SPD)

Due to the high particle density in heavy-ion collisions and to guarantee the required resolution in the impact parameter, the SPD is used for the two inner layers of ITS. The SPD covers a pseudorapidity range of $|\eta| < 2$ and $|\eta| < 1.4$, respectively. And it has a total of 9.8 millions of pixels: 50 × 425. The SPD is used as a L0 trigger (trigger of level 0). For this porpouse each of the 1,200 read chips give a fast signal called "fast OR" that indicates that at least one pixel of a given chip produce a signal. These signals are sended to a FPGA[6] that is capable of implement Boolean logic functions. This allows to develop "triggers" that goes from the MB to the most complicate ones, as the high multiplicity trigger (HM). The detector can be also used for the primary vertex reconstruction, having spacial resolution of $12 \times 100\ \mu\mathrm{m}^2$

Silicon Drift Detector (SDD)

These are two layers of silicon with a total of 133,000 reading channels. The SDD is operated with a drift field of 500 V/cm that results in a drag velocity near to the 6.5 μm/ns in a maximum drag time around 5.3 μs. Its spatial design resolution is near the $35 \times 25\ \mu\mathrm{m}^2$.

Silicon Strip Detector (SSD)

These are the two most external silicon layers of the ITS. The SSD consists of silicon micro strips of two faces, it includes a total of 2.6 million of reading channels which spatial resolution is of $20 \times 830\ \mu\mathrm{m}^2$.

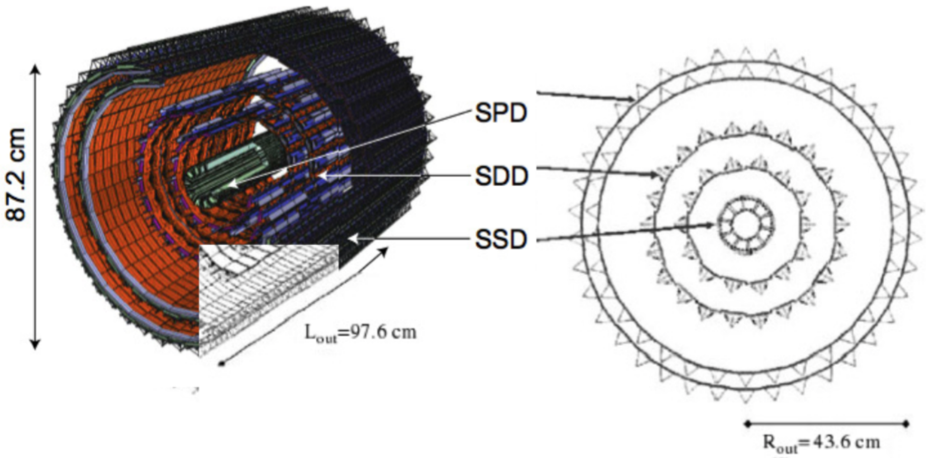

Figure 2.5: ITS schematic, external dimentions are shown.

---

[6] from the acronym of Field Programmable Gate Array, is a semiconductor dispositive that contains logic blocks which interconection and functionality can be configured by a specialized description language.

Particle identification with ITS

The four of the six layers of the ITS (2 of SDD and 2 of SSD) give us the quantity of the energy loss when the particles cross the medium, the combination with the other detectors allows to have a better identification. For the case of the low momentum particles or particles that are not reconstructed by the TPC, the ITS is the only source of identification. The particle identification its made using the method of N-sigma, which consist that to each particle specie (π, K or p) identified by the energy loss dE/dx it is fitted to a Bethe-Bloch function that depends on the particle momentum. For this it is used the PHOBOS parametrization [133] as a function to fit the charged particle energy loss in the silicon.

In the figure 2.6 we show a signal obtained from ITS and the Bethe-Bloch for π, K and p. Taking all the particles that are between $+2\sigma$ and -2σ for each function.

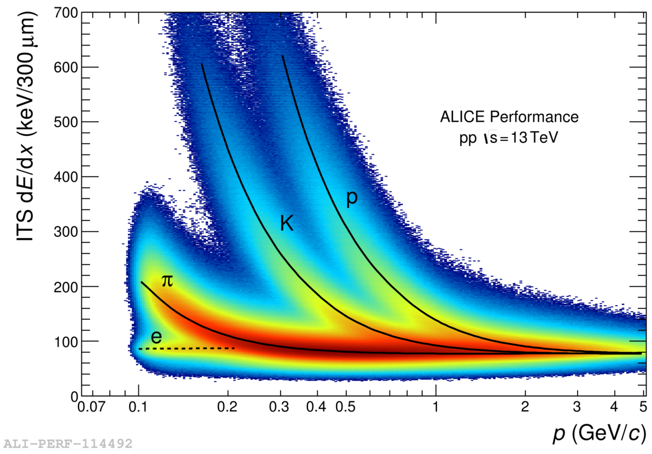

Figure 2.6: Particle identification using ITS detector using the energy loss, the lines represent the PHOBOS parametrization.

2.1.3 Time Projection Chamber

Since TPC[7] [111, 116] (see Fig. 2.8) is the main device used in my analysis for the track reconstruction. It makes sence to briefly describe how a gas detectors works.

Gas Ionization by charged particles

A charged particle that passes through matter, interacts with the electrons and nuclei, and possibly also with the medium as a whole (Cherenkov radiation, Bremsstrahlung). The average energy loss $\langle \mathrm{d}E/\mathrm{d}x \rangle$ is described by the Bethe-Bloch formula which is valid for $\beta\gamma$ (where $\beta = v/c$ and $\gamma = (1-\beta^2)^{-1/2}$) between 0.1 and 1000. When a particle is passing, for example, a kaon passing through the medium and interacts with an atom A, the process will look as $\mathrm{K} + A \rightarrow \mathrm{K} + A^* + e^-$ where due to the liberation of a free electron e^-, then the atom A will be positively charged (a positive ion A^*) [135]. Due to the incident energy, excitations on molecules or atoms are spected, due to this; for the case of ionization the mean energy loss is around twice the value of the ionization potential. As example, for argon, the ionization potential is of 15 eV, but the mean energy required to produce a pair of ion-electron is 26 eV [134]. If we apply an electrostatic potential in the detector, the primary ionization electrons, e^-, are going to be dragged to the positive charge electrode (anode). The positive ions, A^+, will move to the cathode. Thus, we obtain two charged clouds moving in opposite directions. Due to the low mass electrons, they move with a greater drift velocity than the ions. The value of the drift velocity deppends on the form of the $\vec{E}$ field, the properties of the gas molecules, the density or the presure (P) and the temperature (T). What we want is to guarantee that the drift velocity will be stable with low variations of the field intensity. This is the reason why in the drift chambers [134] it is used an electric field $\geq 1 - 1.1$ kV/cm. In this case the drift velocity is around 50 microns per ns.

Ionization Amplification

If an electric field is large enough, the electrons are accelerated such that they will have enough kinetic energy to get free electrons, then, they can participate in subsequent collisions ($e^-A \rightarrow e^-e^-e^-A^+$). Considering a thin wire as anode, we could have high electric field. As an electron is dragged through this wire, the electron will travel in an electric field ($\vec{E}$) that increases. In a neighborhood of the anode this field at a radius r, is given by the linear charge density (λ) as $E \sim \lambda/r$. To describe the multiplicative factor of the gas, we use the Townsend coeficient, $\alpha(E)$/cm, that determines the gas multiplication by unit of lenght at a particular intensity of the field E. In a variable field the gain of a gas (M) could be described by the integration from a radius at which it starts the gas gain to a radius of the anode wire:

$$M = exp^{\int_{r1}^{r2} \alpha(x)dx} \tag{2.1}$$

The Townsend coeficient depends significativly on the gas composition. For example, for drift chambers the gas gain is of the order of 10^4. The devices that uses this mechanism of signal amplification are the multiwire proportional chambers [134] discribed as follows.

Multiwire Chamber in ALICE TPC

The multiwire proportional chamber (MWPC[8]) is a plane formed by anode wires located inside two cathode plates. Each wire acts as an individual proportional counter. The spatial resolution is determined by the spacing between the anodes wires. It is possible to perform a simultaneus lecture of the anode and cathode electrodes. A time projection chamber consists of a cylindrical camera filled by gas with MWPC as the "end caps". A TPC is the main device of ALICE to make the track reconstruction, this covers the full azimuthal angle and a pseudorapidity range $|\eta| < 0.8$ to reconstruct the tracks with full radial lenght. For pp collisions, the memory time of the TPC is a limitation factor for the luminosity given the drift time of $\approx 94\mu$s. The TPC has a central

---

[7] Invented by the physicist David Robert Nygren

[8] Invented by Georges Charpak polish-french physicist winner of the nobel prize in 1992

membrane mantained at high voltage ≈ 100 kV (see Fig. 2.7) and two reading planes in the final covers (see Fig. 2.8). Its active volume is limited to $85 < r < 247$ cm and $-250 < z < 250$ cm in the longitudinal and radial directions, respectively. The material between the interaction point and the active TPC volume corresponds to 11% of an average radiation lenght in $|\eta| < 0.8$. The central membrane divides the volume in two parts. The homogeneous drift field of 400 V/cm in the gas mixture $Ne - CO_2 - N_2$ $(85.7\% - 9.5\% - 4.8\%)$ originates a maximum drift time of 94μs. The electrons of ionization produced by the charged particles that travel trough the TPC are dragged to the reading end caps composed of 72 MWPC with cathodes for the lecture.

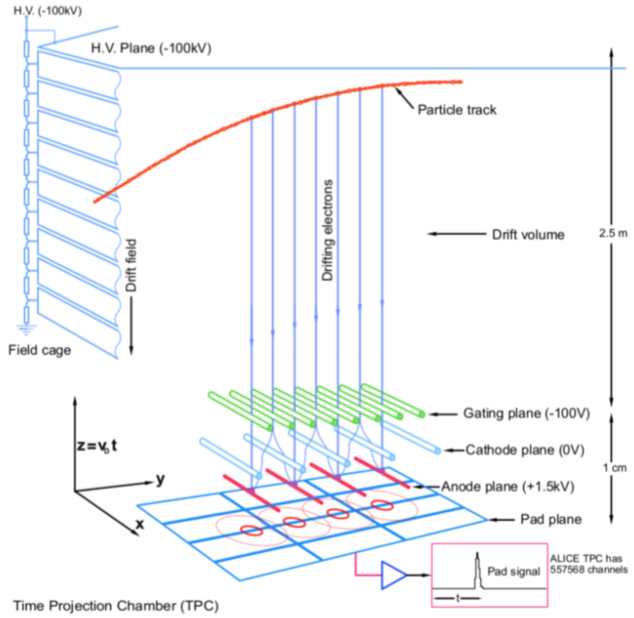

Figure 2.7: Schematic illustration of the reading process of the signals in the endcaps of the TPC [76].

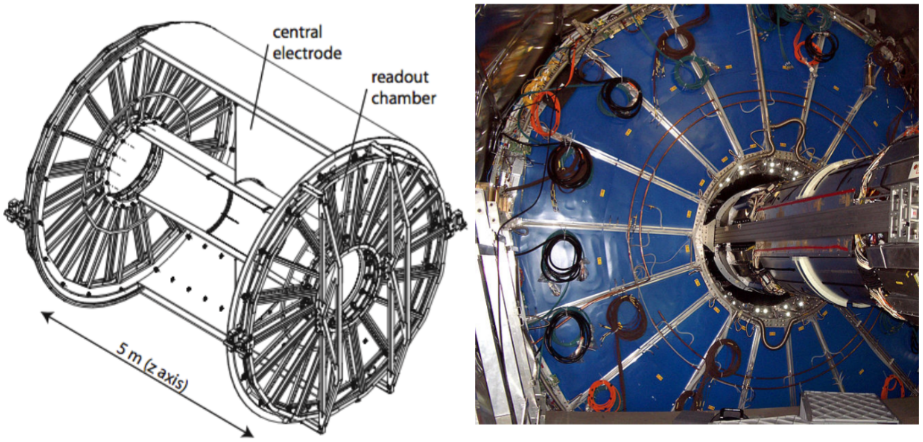

Figure 2.8: TPC esquematic with dimentions and photograph.

Particle identification with TPC

For the TPC the particle identification inside is done using the charged particles energy loss. To use the Bethe-Bloch function as a method to identify the particles, the constants should be parametrized and optimized for the TPC detector. For this the ALEPH parametrization proposed by Blum and Rolandi [134] is used and is described as follows:

$$f(\beta\gamma) = \frac{P_1}{\beta^{P_4}}\left(P_2 - \beta^{P_4} - ln(P_3 + \frac{1}{(\beta\gamma)^{P_5}})\right) \tag{2.2}$$

Using this parametrization and using the N-sigma method the particles are identified where if a particle is inside the $\pm3\sigma$ region predicted by the ALEPH parametrization, then the particle can be identified as π, K or p. In the figure 2.11 the energy loss versus momentum for each particle crossing the TPC is plotted, from this we can observe that the minimum ionizing energy loss (MIP) for most of the particles is about the region $40 < dE/dx < 60$, below the region of the electrons at the Fermi-plateau ($dE/dx > 60$), also we see that the energy loss at high momentum rises slowly within a logarithmic shape, the so-called "relativistic rise", which rise decrease as the mass of the particles increase.

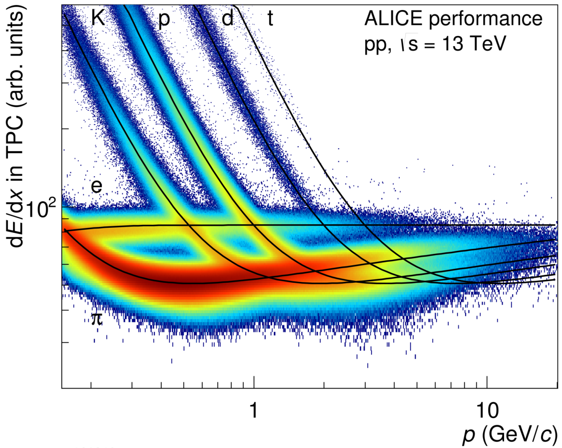

ALI-PERF-101240

Figure 2.9: Particle identification using TPC energy loss versus momentum, lines represent the ALEPH parametrization.

2.1.4 Time Of Flight (TOF)

The Time Of Flight detector [111, 118] covers a central region of $\eta < 0.9$ in pseudorapidity, and it is capable to identify charged particles in a intermediate momentum range from 0.4 to 2.5 GeV/c for pions, kaons and 4 GeV/c for protons, achieving a separation greater than 3σ between π/K and K/p. The detector covers a cylindric surface with an acceptance in the polar angle between 45 and 135 degress. The internal radius of the cilindrical shell is of 370 cm and the external radius of 399 cm, with a lenght of 741 cm in the z direction. The modular structure of TOF counts with 18 sectors distribuited in the azimuthal angle (ϕ) and this arrange is repeated in five modules in the z direction (see Fig. 2.10). The modules contain a total of 1638 detector elements, called Multi-gap Resistive Plate Chamber (MRPC) and they cover an area of 160 m^2. The main characteristic of this chambers is the strong and uniform electric field in all the gaseous volumes of the detectors, causing that the ionization due to the charged particles produced during the collisions, generate inmediatly a particle avalanch that will produce the signals. Therefore, it doesn't exist a drift time asociated to the moving electrons, in contrast to the TPC, the time of flight of the detected particles is obtained measuring the delay between the trigger signal, given by the T0 detector, and the signal of TOF.

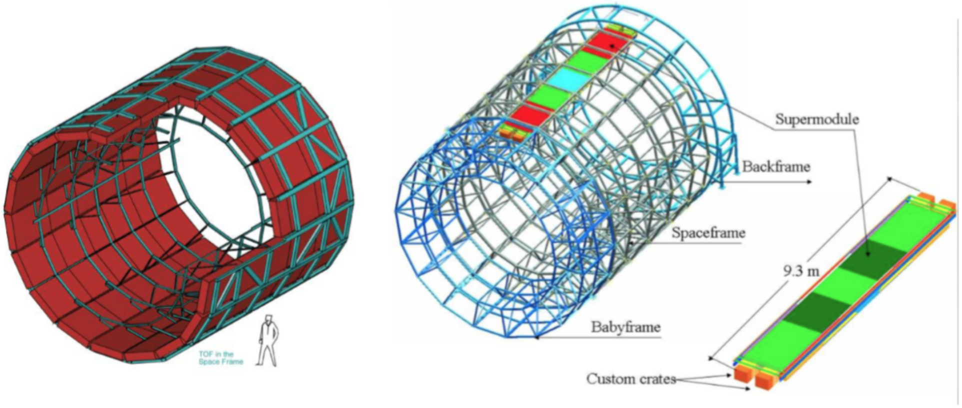

Figure 2.10: TOF schematics and dimentions of the layouts.

Particle identification with TOF

Differing the technique from ITS (section 2.1.2) and TPC (section 2.1.3), the TOF detector doesn't use the energy loss as a method of particle identification, instead of this the identification is based on the time of flight and the integrated path lenght of each particle that cross the detector. We know that $\beta = v/c = L/(tc)$, with L the distance that a particles flies, also the difference on the particle arriving time signal between two detectors will be given by $\Delta t = t_2 - t_1 = L/(c\beta) = t_{TOF}$, but due that the particle velocity depends on its mass m and momentum p by $\beta = ((\frac{mc}{p})^2 + 1)^{-1/2}$ and using the β definition with t_{TOF} we have an expression for the mass of a charged particle defined by [136]:

$$m = p\sqrt{\left(\frac{ct_{TOF}}{L}\right)^2 - 1} \tag{2.3}$$

In the next figure we can find the velocity β for the particles as a function of the momentum. The particle-identification capability of a TOF detector is related to the number of standard deviations in the time-of-flight difference of two particles $n\sigma = (t_1 - t_2)/\delta t$, where δt is the time resolution.

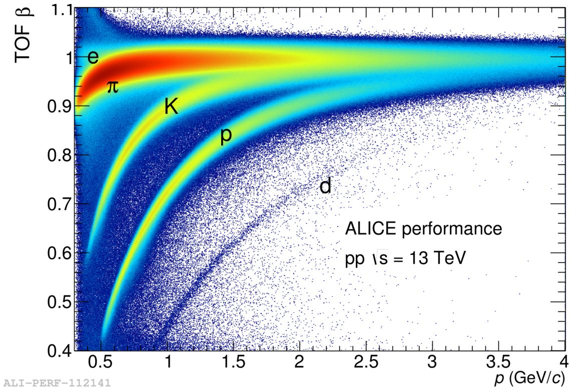

Figure 2.11: Particle identification using TPC detector using the energy loss, the lines represent the ALEPH parametrization.

2.2 ALICE offline software

The data producction of the LHC experiments (near 10-15 PB per year) is at a new scale compared to every previous experiment. For a year standard run of the order of 10^9 pp events and 10^8 Pb-Pb events are espected given place to a total volume of "raw" data of 2.5 PB. The data taken with cosmics in 2008 acumulate a total of 300 TB. The computing source required for the reconstruction and data analysis, thus as production of data from simulated events needed for the understanding of the data, exceed the computing power of only one institute or even centers as CERN. Also institutes that are part of the collaboration provide storage and computing resource. Actually more than 80 centers contribute to the ALICE computing source. The data distribution for reconstruction and analyzing can not be manually developed and this leads to the need of automatized systems. The GRID [137] concept was identified as a solution. ALICE also use a proper enviroment called AliEn [138] (for ALICE Environment); as an interface to connect with Grid, composed of specified service of ALICE that are part of the AliEn and basic GRID service installed in different sites. The GRID paradigm imply the unification of computing centers distribuited to provide storing power and computing around the world. The software that implements the GRID concept is called Grid middleware. ALICE has developed his own one‘s called AliEn since 2001.

An ALICE user employs AliEn to connect to the ALICE Grid, which is composed of a general services combination that are provided for many solutions of the Grid middleware and specific ALICE services provided by AliEn. Part of ALICE Grid, is a global catalog of files storage around the world, the automatic merge of execution jobs to a localization in one of the connected sites, an user interface of shell type and API9 services for ROOT [9] [139] platform. Actually the ALICE Grid has 80 sites localized in 21 countries (see Fig 3.8). The system has been extensively proved with a running number of jobs above 10000 for several weeks. The simulated official data used in this thesis were produced in this sites.

For the event simulation the framework provides the following functionality:

1. Event generation. A collision is simulated by an event generator that is interfaced with AliRoot, this step produces the kinematics tree containing the full information about the generated particle.

2. The particles are propagated through the detector material which is modeled as realistically as possible. In this process, particles can interact with matter, decay, and create additional particles. Naturally, these particles have to be propagated through the detector as well. The total number of particles after the transport is significantly larger than the number of particles created in the initial generation step. During this process all interactions of particles with sensitive detector parts are recorded as hits that contain the position, time, and energy deposit of the respective interaction. Furthermore, track references are stored that can be used to follow a track's trajectory, mainly needed for the debugging of the reconstruction algorithms.

3. Digitization. If a particle produced a signal in a sensitive part (hit), the corresponding digital output of the detector is stored as a summable digit taking into account the detector's response function. Possible noise is then added to the summable digit and it is stored as a digit. Summable digits allow events to be merged without duplication of noise. In the last step, the data is stored in the specific hardware format of the detector.

---

[9] The ROOT platform for ALICE is called ALIROOT.

Figure 2.12: Computing centers that contribute the the ALICE Grid. They are mostly located in Europe, nevertheless, some others are in other continents. In México there are 2 located at UNAM [140].

2.3 Track reconstruction in ALICE

2.3.1 Primary-vertex reconstruction

The reconstruction of the primary vertex is performed by the hit points reconstructed in the two layers of the SPD. The algorithm uses the reconstructed points in the two layers that are close in ϕ and z which are paired and used in a linear extrapolation to estimate the position of the primary vertex along the beam axis and in the transverse plane separately. The estimate of the vertex position along the beam axis is then corrected using the result obtained for the transverse plane. This estimate is used as a constraint in the first pass of the track reconstruction. The tracks reconstructed in the TPC and the ITS are then used for recalculating the position of the primary vertex which improves the precision of the measurement. The resulting resolution of the vertex position depends on the track multiplicity and is typically better than 10 μm in the z coordinate and about 35 μm in the transverse plane for heavy-ion collisions and about 110 μm in the z coordinate and 70 μm in the transverse coordinate for proton collisions.

A charged-particle decay inside the tracking volume can produce a kink on the track's trajectory, for example the decay $K^+ \rightarrow \mu^+\nu_\mu$. Due to the fact that the neutrino is not tracked, the kaon's trajectory appears changed, hence the name kink. In the reconstruction the K^+ and the μ^+ are found as separate tracks that obviously only correspond to one primary particle. The reconstruction identifies that the two tracks are related and flags the first as the *"kink mother"*, the second as the *"kink daughter"*.

To assure that the tracks originate from the primary vertex (in the following just called vertex), a cut on the distance between the vertex and the track is applied. For this purpose the closest point of the track's trajectory to the vertex is determined (*"Distance of Closest Approach"* -DCA). Either a cut on the absolute DCA (*"absolute DCA cut"*) or on the DCA divided by its estimated resolution is applied (*"normalized DCA cut"*). The first approach is more resilient in the case that the vertex position and the track-parameter resolutions are imprecise. The latter is in principle better as it uses more of the measured information. The accuracy of the resolutions calculated in the reconstruction is not well-known in early data-taking, therefore the first approach is more extensively discussed here. Furthermore, the absolute DCA cut can be applied separately in two dimensions [141]:

$$\left(\frac{\Delta r}{dr}\right)^2 + \left(\frac{\Delta z}{dz}\right)^2 < 1. \tag{2.4}$$

still allowing for different values dr and dz in the r and z directions, respectively (elliptic cut). The choice depends on the status of the calibration and alignment and possible correlations between the two values. For example an insufficient drift-time calibration in the TPC leads to an imprecise value in z. In this case a narrow r cut could be combined with a wider z cut.

2.3.2 Track reconstruction in the central barrel

When a charged particle passes through a tracking detector it leaves a signal in the sensitive regions which allows to determine the position of the points in space where the particle crossed the detector called as *"clusters"*. Reconstruction algorithms are designed to recognize which space points belong to the same track and to reconstruct the momentum of the corresponding particle. Tracking in the central barrel of ALICE starts with setting initial seed values for the track parameters using space points in the outermost pad rows of the TPC and a rough constraint on the position of the primary vertex. The tracking proceeds inwards by propagating tracks and combining compatible space points in the TPC using Kalman filtering [143], which is a method that allows to consider effects such as energy loss and multiple scattering in the material of detectors or to take into account dead zones between detectors when extrapolating tracks. The seeding and track propagating within the TPC is done once more without considering the primary vertex position in order to reconstruct tracks of secondary particles, that were not produced in the vicinity of the primary vertex. The tracks are then propagated to the outer layer of the ITS, starting with the tracks having the highest momentum. The propagation is done first with a strict primary-vertex constraint and then without it in order to consider candidates for secondary tracks reconstructed in the TPC. When propagating TPC tracks into the ITS layers, ITS tracker attempts to prolong the TPC tracks as close as possible to the primary vertex. All space points compatible with the extrapolation of a given TPC track are considered and the resulting track candidates are compared at the end using their sums of the *"χ^2 per cluster"* which determines the quality of the fit between the track and the contributing clusters.

Then, a special ITS stand-alone tracking procedure is applied in order to recover more tracks from the rest of the ITS clusters belonging to low p_T particles with p_T down to about 80 MeV/c that cannot be efficiently reconstructed inside the TPC or to recover tracks that went through dead regions of the TPC. After this stage, Kalman filtering is applied for the second time but outwards from the point of closest approach to the collision point, through the ITS, and back to the outer wall of the TPC. Points with large deviation from the fit are removed during this pass. More space points are assigned to the tracks as the filtering proceeds into more distant detectors such as TRD, TOF, EMCal, HMPID and PHOS. Finally, Kalman filtering is applied once more for refitting all tracks from the outside inwards, starting from the outer radius of the TPC, in order to calculate track parameters at the point of the closest approach to the primary vertex.

2.3.3 Minimum Bias trigger events

Different trigger systems can be configured simultaneously and a lot of complex patterns of this can be implemented in the ALICE high level trigger system (HLT, by acronym).

The Minimum-Bias (MB) trigger is the trigger system used to select the greater number of interactions seen by the detector, even when the transfered momentum between the interacting particles is low, or when just final state particles are produced. This triggers combined the detector information of VZERO and SPD.

The VZERO detector use the time of the hits produced by charge particles to distinguish and select events. In the practice during the normal operation, both arrange are required. The VZERO.AND[10] mode, to provide the triggers: Minimum Bias, semicentral (CT1) and central (CT2), and the VZERO.OR mode[11] can be also used. By the other hand, the 1,200 reading chips of the SPD produce the same number of signals which are logically combined to form the global element of the trigger fast-OR (GLOB.OR). Using the logical combinations of the different elements of the trigger, we have the next set of MB triggers which were used for RUN 1.

- MB1 = (GLOB.FO or VZERO.OR) and no V0 BG[12].
- MB2 = (GLOB.FO or VZERO.OR) and no V0 BG.
- MB3 = (GLOB.FO and VZERO.AND) and no V0 BG.

For RUN 2 the trigger for Minimum Bias uses the selection requiring a hit in either the VZERO scintillators or in the AD arrays [142].

In practive for real data, the triggers (off-line) are combined with the information provided by the signals of bunch crossing of LHC.

---

[10] Requires at least one hit in the counter in both sides.

[11] Requires one hit in the counter in one side.

[12] This means that in a collision of beam-gas or beam-halo was detected by the V0 which uses the time of the collision.

Chapter 3

ALICE recent results: QGP in small and large systems

> The only object of theoretical physics is to calculate results that can be compared with experiment... it is quite unnecessary that any satisfactory description of the whole course of the phenomena should be given.
>
> (Paul Dirac)

In this section we discuss the discovery of QGP-like phenomena in small collision systems, proton-proton (pp) and proton-led (p-Pb) collisions with some results obtained by ALICE during RUN1. This chapter is based on the review published in [35].

3.1 Soft probes

To learn about the early state of the system, low p_{T} ($< 2.2\,\mathrm{GeV}/c$) direct photons are studied. A temperature $T = 297 \pm 12^{\mathrm{stat}} \pm 41^{\mathrm{syst}}$ MeV has been measured for the $0-20\%$ Pb-Pb collisions at $\sqrt{s_{\mathrm{NN}}}$ =2.76 TeV [144]. Hence, the system at the LHC is hotter than that produced at RHIC, where an early temperature of $239 \pm 25^{\mathrm{stat}} \pm 7^{\mathrm{syst}}$ MeV was measured for the same centrality class in Au-Au collisions [145]. It is worth noticing that such temperatures are already above the one predicted to achieve the QCD phase transition [87]. The system formed at the LHC is also denser, the average multiplicity per number of participants is twice that measured at RHIC [146].

The system expands and cools down, when the inelastic interactions cease the yields of particles are fixed. This is the stage of the so-called chemical freeze-out which is studied using the yields of identified hadrons. Within 20% particle ratios, e.g., the proton yield normalized to that of pions, are described by thermal models with a common chemical freeze-out temperature of $T_{\mathrm{ch}} \approx 156$ MeV [147]. However, larger deviations are observed for protons and K^{*0}, for the latter, this is not a surprise since its mean lifetime is smaller than that of the fireball ($\approx$10 fm/c) [148], and therefore the resonance yield may deviate from the expected values due to hadronic processes like rescattering and regeneration [149].

On the other hand, the measurement of the spatial extent at decoupling time is accesible via intensity interferometry, a technique which exploits the Bose-Einstein enhancement of identical bosons emitted close by in phase space. This approach is known as Hanbury Brown-Twiss analysis (HBT) [150]. Such an analysis using identical charged pions has been performed by ALICE. The results give a pion homogeneity volume of $\approx 300\,\mathrm{fm}^3$ (two times that reported at RHIC) and a decoupling time of $\approx 10\,\mathrm{fm}/c$ [148].

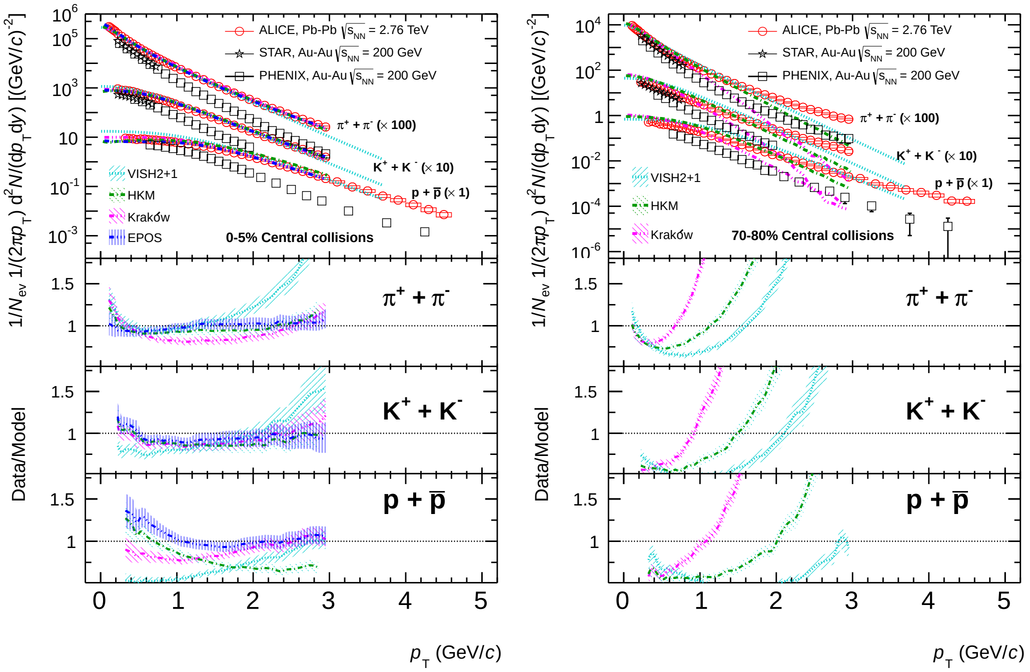

Figure 3.1: (Color online) Transverse momentum spectra of charged pions, kaons, and (anti)protons measured in central (left) and peripheral (right) Pb-Pb collisions at $\sqrt{s_{\rm NN}}$ = 2.76 TeV. The systematic and statistical uncertainties are plotted as color boxes and vertical error bars, respectively.

The transverse momentum distributions of identified hadrons contain valuable information about the collective expansion of the system ($p_{\rm T} \lesssim 2\,{\rm GeV}/c$), the presence of new hadronization mechanisms like quark recombination ($2 \lesssim p_{\rm T} \lesssim 8\,{\rm GeV}/c$) [151] and, at larger transverse momenta, the possible modification of the fragmentation due to the medium [152, 153]. ALICE has reported the transverse momentum spectra of charged pions, kaons and (anti)protons as a function of the collision centrality from low (hundreds of MeV/c) [154] to high $p_{\rm T}$ (20 GeV/c) [156, 186].

Figure 3.1 shows that for central Pb-Pb collisions the low momentum spectra ($< 2\,{\rm GeV}/c$) are well described by hydrodynamic models (within 20%), except the low $p_{\rm T}$ ($< 1\,{\rm GeV}/c$) proton yield [158, 104, 105, 106, 159]. Models which best describe the data include hadronic rescattering with non-negligible antibaryon annihilation [106, 159]. The description of the results by hydrodynamic models is only observed in $0 - 40\%$ Pb-Pb collisions, results for more peripheral collisions disagree with such prediction. This behavior has been recently studied for the average $p_{\rm T}$ in different colliding systems [160]. In order to quantify the freeze-out parameters, a simultaneous fit of the blast-wave function to the low $p_{\rm T}$ part of the spectra can be performed. This model assumes a locally thermalized medium, expanding collectively with a common velocity field and undergoing an instantaneous common freeze-out.

The analysis of the spectral shapes of the $p_{\rm T}$ distributions can be done using a blast-wave fit [79], which allows the extraction of the parameters related with the temperature at the kinetic freeze-out ($T_{\rm kin}$) and the average transverse expansion velocity ($\langle\beta_{\rm T}\rangle$). At the LHC, the radial flow in the most central collisions is found to be $\approx 10\%$ higher than at RHIC, while the kinetic freeze-out temperature was found to be comparable to that extracted from data at RHIC, $T_{\rm kin} = 95\,{\rm MeV}$ [154]. From the study of the low $p_{\rm T}$ particle production we conclude that at the LHC the created system is larger, hotter and longer-lived than that produced at RHIC.

The intermediate $p_{\rm T}$ is studied with the particle ratios as a function of $p_{\rm T}$ [186]. For central heavy-ion

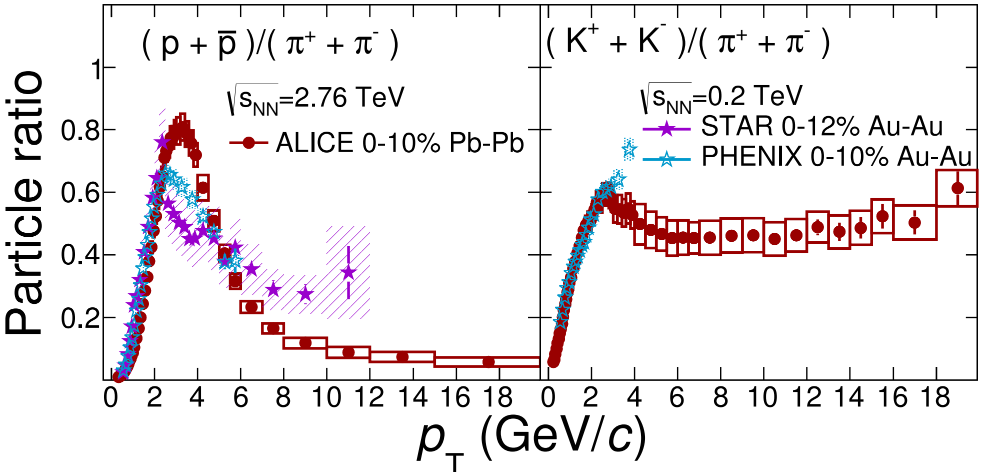

Figure 3.2: (Color online) ALICE (circles) results from $\sqrt{s_{\mathrm{NN}}} = 2.76\,\mathrm{TeV}$ Pb-Pb collisions compared with STAR and PHENIX results for $\sqrt{s_{\mathrm{NN}}} = 200\,\mathrm{GeV}$ Au-Au collisions. Left panel: the proton-to-pion ratio. Right panel: the kaon-to-pion ratio.

collisions, Fig. 3.2 shows a comparison of particle ratios with results from STAR and PHENIX at the RHIC measured in Au-Au collision at $\sqrt{s_{\mathrm{NN}}} = 200\,\mathrm{GeV}$. The proton-to-pion peak at the LHC is approximately 20% larger than at the RHIC, which is consistent with an increased average radial flow velocity. Interestingly, there is no evidence for a peak in the kaon-to-pion ratio measured by PHENIX, which is similar to the ALICE data points for $p_{\mathrm{T}} < 3\,\mathrm{GeV}/c$, but continues to rise in the few data points above this p_{T}. To check the effect of radial flow the shapes of the p_{T} distributions of ϕ-meson and protons are compared. The results indicate that for central Pb-Pb collisions the shapes of the proton-to-pion and ϕ-to-pion ratios are the same. On the other hand, for $p_{\mathrm{T}} < 4\,\mathrm{GeV}/c$, the ϕ-meson yield normalized to that of protons becomes flat going from the most peripheral to the most central Pb-Pb collisions. This suggests that the mass, and not the number of quark constituents, determines the spectral shape in central Pb-Pb collisions. This is in a good agreement with the hydrodynamical interpretation. It has been recently shown that the spectral shapes, studied with the average p_{T}, exhibit a scaling with the hadron mass (number of constituent quarks) only in the $0-40\%$ ($40-90\%$) Pb-Pb collisions [160].

Using the scalar product method, the elliptic flow for identified hadrons has been measured [161] over a broad p_{T} range. Going from central to semi-peripheral Pb-Pb collisions v_2 increases as expected due to the eccentricity increase. For p_{T} below $2\,\mathrm{GeV}/c$ a mass ordering is observed indicating the interplay between elliptic and radial flow. For higher p_{T}, the hadron-v_2 seems to be grouped into baryons and mesons, the exception is the v_2 of ϕ-mesons, which for central Pb-Pb collisions follows that for baryons. This observation indicates that the behavior of v_2 is driven by the hadron mass and not by the number of quark constituents. ALICE has also reported the violation of the scaling of v_2 with the number of constituent quarks, such a observation is also against the scenario with quark recombination/coalescence.

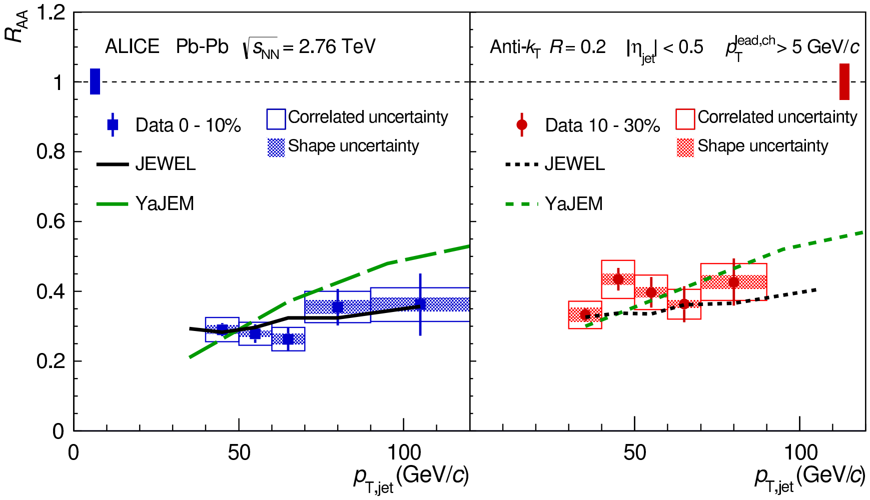

Figure 3.3: (Color online) Nuclear modification factor of full jets with $R = 0.2$ and p_T leading bias of 5 GeV/c in central Pb-Pb collisions [163].

3.2 Jet studies

The amount of suppression of inclusive particle production relative to pp collisions can be quantified with the nuclear modification factor, defined as

$$R_{AA}(p_T) = \frac{1}{\langle N_{coll}\rangle} \frac{d\sigma^{AA}/dp_T}{d\sigma^{pp}/dp_T} \tag{3.1}$$

where σ^{AA} and σ^{pp} are the cross section in pp and AA collisions, respectively; and $\langle N_{coll}\rangle$ is the average number of binary nucleon-nucleon collisions.

Figure 3.3 shows R_{AA} of full jets with $R = 0.2$–0.3 in central Pb-Pb collisions at $\sqrt{s_{NN}} = 2.76$ TeV. The data manifest a strong suppression of jet production relative to pp collisions used as a reference for the charged jet study and relative to the pp reference in case of full jet studies [162]. Comparing the nuclear modification factor of charged jets to that of charged particles at large p_T one can see that the amount of the suppression is similar although the underlying parton p_T scale is different for inclusive particles and jets. This observation, although it may seem at first glance counterintuitive as one would expect jets to recover most of the radiated energy, could be explained by the radiation of soft particles at large angles away from the jet axis. The nuclear modification factor of full jets is in Fig. 3.3 confronted with two models of jet quenching. The JEWEL model [164] incorporated a microscopical description of the transport coefficient $\hat{q}$ and to determine the initial geometry it uses a combination of Glauber approach and PYTHIA including one dimensional Björken expansion of the medium. YAJEM [165] is based on 2+1D hydrodynamical description including Glauber Monte-Carlo approach for initial state and leading order QCD calculations to determine outgoing partons. Both predictions eventually use the Lund hadronization model implemented in PYTHIA. Although both models are conceptually different and in YaJEM the jet quenching effect is a bit stronger with p_T than observed in data, they describe the measured data well. Larger statistics and more differential jet observables are therefore needed to further constrain models.

In order to study details of path-length dependence of energy loss, ALICE performed studies of elliptic anisotropy of inclusive charged jets [166] and semi-inclusive distributions of recoil jets [167] which complement and further extend earlier studies of elliptic anisotropies of inclusive high-p_T particles and modification of away-side di-hadron correlations [168]. For collisional energy loss, the path length dependence is expected to be

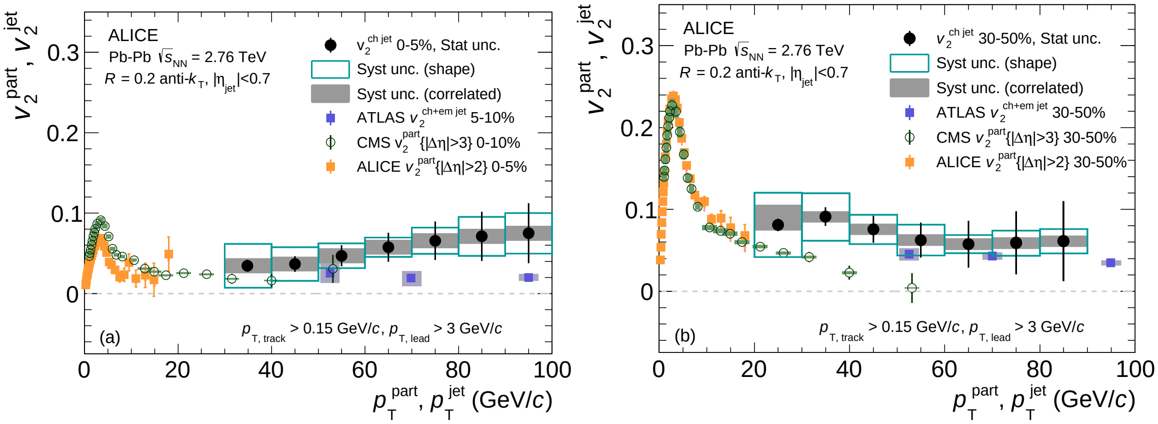

Figure 3.4: (Color online) Elliptic anisotropy (v_2) of inclusive charged particles and charged jets with the resolution parameter $R = 0.2$ in central (lef) and semicentral (right) Pb-Pb collisions at $\sqrt{s_{\mathrm{NN}}} = 2.76\,\mathrm{TeV}$ measured by ALICE [166]. The data are compared with charged particle v_2 anisotropies measured by ALICE [169] and CMS [170] and calorimetric jets with $R = 0.2$ measured by ATLAS [171].

linearly proportional to the length traversed by the parton in medium, while for radiative energy loss, where in addition interference effects play a role, the dependence can be quadratic. In AdS/CFT class of models an even stronger dependence on path length traversed is predicted. In Figure 3.4 the measurement of elliptic anisotropy v_2 for charged jets with the resolution parameter $R = 0.2$ is shown in central and semi-central Pb-Pb collisions. The data show significant positive v_2 value in semi-central Pb-Pb collisions pointing to the path length dependence of jet suppression. In central collisions the current uncertainties on the measurement do not allow to draw a definite conclusion, although the v_2 magnitude is also positive. These data are also compared to v_2 for full jets measured by ATLAS [171] and inclusive charged particles [169, 170]. Although these measurements cannot be directly compared quantitatively due to different p_{T} scales and centrality selections, qualitatively they agree and provide a clear evidence of path-length dependent parton energy loss [172].

3.3 Hydrodynamic Flow and Blast Wave analysis

Observables such as the two hadron correlations in the longitudinal (η) and transverse (ϕ) region respect to the beam direction, are used to find hydrodynamic flow signals. In Heavy Ion collisions long range angular correlations are observed between the reference particle and the associated. Such effect has been understood as a consecuence of the collective expansion of the medium and it's well described by the models that incorporates the hydrodynamical evolution of the system. As we have describe in the previous section 3.1, the transverse momentum spectra of identified chaged particles are sensitive to radial flow. As illustrated in figure 3.1 the measured spectra in central collisions are described by hydrodynamical models, while in peripheral collisions the models fail and in fact the spectra are quite similar to those measured in pp collisions [155]. This can be an indication that QGP is only produced in central collisions. With the available data from ALICE p-Pb collisions, it has been studied the two hadron correlations as a function of multiplicity and they have observed that there is evidence of collective phenomena present in this small systems. This is perfectly illustrated in Fig. 3.5 where the Fourier coeficient v_2, which is extracted from the two hadron correlations, it's ploted as funtion of the p_{T} for different multiplicity intervals and for different particle species. At high multiplicity it is observed the mass ordering typical from Pb-Pb collisions [184]. It is important to mention that such quantity is measured in the region outside of the jet peak. Also, it has been reported the presence of two "ridges" located in the near and away side to the triggered particle [182].

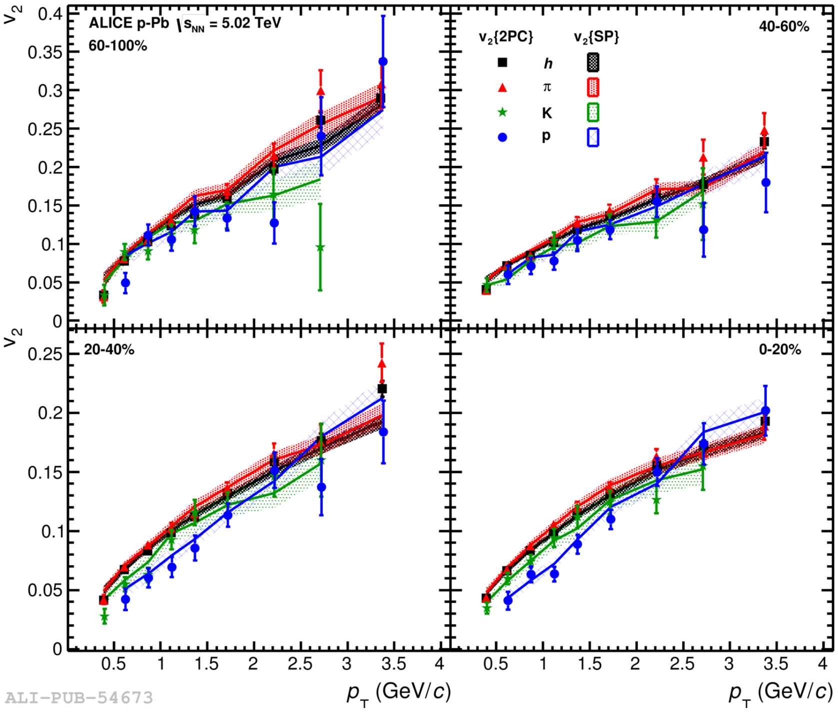

Figure 3.5: Elliptic flow v_2 for charged particles, pions, kaons and protons as function of p_T its shown for different multiplicity intervals. Measurements where done with p-Pb data at $\sqrt{s}_{NN} = 5.02$ TeV. the upper left panel (lower right) corresponds to low (high) multiplicity events.

The identified particles spectra also reveal such similar features to that observed in heavy ion collisions, to know, as the event multiplicity increaces the spectra gets harder, also this effect increaces as the hadron mass increaces (efect featured of radial flow). Almost, the models that include hydrodynamics describe better the data. To study the evolution of the spectra shapes as function of multiplicity or centrality and to compare the results from the analysis applied to different systems, it has been used as a tool a simultaneus fit of the Blast-Wave function to the measured spectra in a given system.

An hydro-thermal model called Boltzman-Gibbs Blast Wave (BGBW) [79] is used to describe the yield of identified particles, this is expressed in terms of the identified particle's transverse mass ($m_T = \sqrt{m_T^2 + p_T^2}$), the kinetic freeze-out temperature (T_{kin}) and the transverse velocity (β_T) as follows:

$$\frac{1}{p_T}\frac{dN}{dp_T} \propto \int_0^R m_T I_0\left(\frac{p_T \sinh\rho}{T_{kin}}\right) K_1\left(\frac{m_T \cosh\rho}{T_{kin}}\right) rdr. \tag{3.2}$$

Where I_0 and K_1 are the modified Bessel functions, $\rho = \tanh^{-1}\beta_T = \tanh^{-1}\left(\left(\frac{r}{R}\right)^n \beta_s\right)$, where r is the radial distance from the center of the fireball in the transverse plane, R is the radius of the fireball, B_s is the transverse expansion velocity at the surface and n is the exponent of the velocity profile.

This kind of analysis are commonly applied in Pb-Pb collisions and they used to extract quantities such as the kinetic freeze-out themperature (T_{kin}) and the mean transverse velocity of the medium (β_T). It results surprisingly that the values for the obtained parameters are very similar in very different systems such as Pb-Pb, p-Pb and pp. This is shown in Fig. 3.6, where the T_{kin} and the β_T are ploted. As discussed in the identified particle spectra they require an hydrodynamical flow to be produced by the models, However, in this figure it is shown that PYTHIA 8 also produce similar qualitative results. This fact is important because the model does not include hydrodynamics. To resume, we see that p-Pb collisions show collectivity evidence but there's no signal of "quenching".

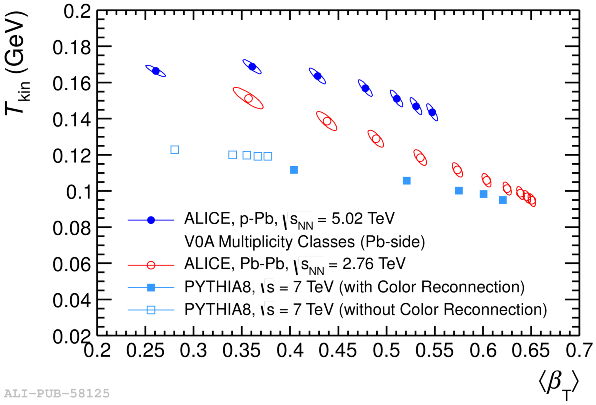

Figure 3.6: Parameters extracted from the blast wave analysis applied to the identified particles spectra [187].

3.4 Fluid-like behavior in small systems: pp and p-Pb collisions

The study of particle production in high-multiplicity pp and p-Pb collisions at the LHC has revealed unexpected new collective-like phenomena. The understanding on the origin of these effects is ongoing, for the majority of the heavy-ion community they are interpreted as the evidence of the QGP formation in small systems [174, 175]. Although, another fraction of the community is exploring new explanations in terms of initial state effects [176, 177, 178], i.e., without invoking the formation of a small drop of QGP.

Two-particle angular correlations provide important information about the hot and dense QCD matter formed in heavy-ion collisions. In particular at RHIC energies, long-range angular correlations (ridge structure) were reported [179], and they were attributed to the hydrodynamical evolution of the system. Motivated by the high particle densities produced in the highest multiplicity pp collisions at the LHC energies, which were very close to those measured in high energy Cu-Cu collisions, the CMS Collaboration studied the two-particle angular correlations of charged particles in pp collisions at $\sqrt{s} = 7\,\mathrm{TeV}$ and discovered the ridge structure in small systems [180]. While the $p_{\rm T}$-integrated correlation does not show any special feature, in the $p_{\rm T}$ range 1–3 GeV/c the near side long range angular correlation is clearly observed. Similar structures were also observed in p-Pb collisions at $\sqrt{s_{\rm NN}} = 5.02\,\mathrm{TeV}$ [181, 182, 183]. Furthermore, in high multiplicity events, non-zero second-order Fourier coefficients were extracted from the long-range correlations. Using the ALICE capabilities for particle identification, the proton v_2 was observed to be smaller than that for pions, up to about $p_{\rm T} = 2\,\mathrm{GeV}/c$ [184]. This effect is similar to the mass ordering of v_2 observed in heavy-ion collisions.

The transverse momentum spectra of charged pions, kaons and (anti)protons as a function of the event multiplicity have been measured up to 20 GeV/c [185]. At low $p_{\rm T}$ (< 2–$3\,\mathrm{GeV}/c$) the spectra exhibit a hardening with increasing multiplicity, with this effect being more pronounced for heavy particles. We are therefore observing features which resemble the radial flow effects well known from heavy-ion collisions [186] and which are well described when a hydrodynamical evolution of the system is considered. At the LHC [187] it was shown that for high multiplicity p-Pb events, the $p_{\rm T}$ spectra were described by the blast-wave function. Using the parameters obtained from the simultaneous fit to pion, kaon, proton and lambda $p_{\rm T}$ spectra the model is able to describe the multi-strange baryon $p_{\rm T}$ distributions ($p_{\rm T} < 4\,\mathrm{GeV}/c$) [191]. The feature is also observed in pp collisions simulated with PYTHIA 8 [188, 24], where no hydrodynamical evolution is included, instead multiple partonic interactions (MPI) and color reconnection are producing the effects. Some ideas have been proposed

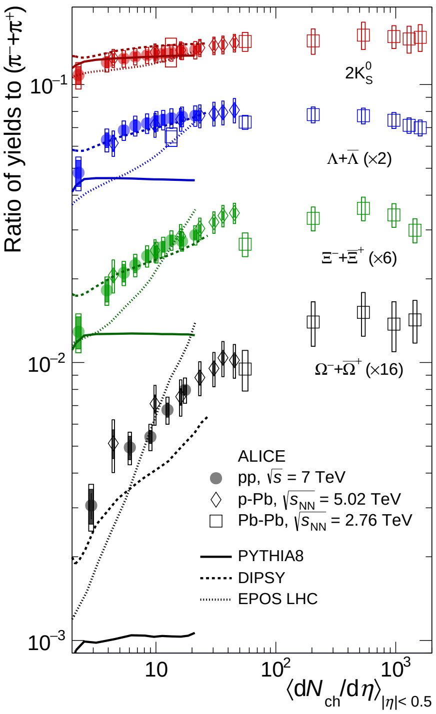

Figure 3.7: (Color online). Multiplicity dependence of strange and multi-strange hadrons yields normalized to than for charged pions. The empty and dark-shaded boxes show the total systematic uncertainty and the contribution uncorrelated across multiplicity bins, respectively. The values are compared to calculations from MC models and to results obtained in Pb-Pb and p-Pb collisions at the LHC.

to understand the role of MPI in data [189, 190, 92, 16, 34]. The multiplicity dependence of the intermediate to high-p_{T} particle production is studied with the particle ratios [185]. The proton-to-pion ratio as a function of the event multiplicity exhibits a maximum (bump) at $p_{\mathrm{T}} \approx 3\,\mathrm{GeV}/c$ and the size of the bump increases with increasing multiplicity. On the other hand, at higher transverse momenta ($p_{\mathrm{T}} > 10\,\mathrm{GeV}/c$) the ratios return to the values measured for pp and Pb-Pb collisions. Any particle species dependence of the nuclear modification factor is therefore excluded.

In order to look for the presence of re-scattering effects in high multiplicity p-Pb collisions; the K^{*0} and ϕ relative to charged kaons production is studied as a function of the cube root of the average mid-rapidity charged particle density. In heavy-ion collisions the decreasing trend of $\mathrm{K}^{*0}/\mathrm{K}$ with increasing fireball size has been explained as a consequence of a re-scattering of K^{*0} decay daughters in the hadronic phase. It is worth noticing that a similar trend is also observed in p-Pb collisions.

Finally, I will discuss the latest results on multiplicity-dependent enhancement of strange and multi-strange hadron production in pp and p-Pb collisions [29]. Figure 3.7 shows a significant enhancement of strange to non-strange hadron production with increasing particle multiplicity in pp collisions. The behaviour observed in pp collisions resembles that of p-Pb collisions at a slightly lower centre-of-mass energy [191], both in the values of the ratios and in their evolution with the event activity. This suggests that the origin of strangeness production in hadronic collisions is driven by the characteristics of the event activity rather than by the initial-state collision system or energy. In the context of heavy-ion collisions, this effect (strangeness enhancement) has been considered a signature of the QGP formation. Recently, it has been pointed out that a perfect scaling of the particle ratios with the energy density holds for the different colliding systems [192] opening new possibilities for a better understanding of the QGP-like features in small systems.

3.5 Event sphericity measurements

Measurements of event sphericity [92], where the MC event generators exhibit at high multiplicities a decrease on the transverse sphericity $< S_T >$, which is defined with a value between 0 and 1, (given by the eigenvalues of a momentum linearized tensor described in section 1.4.1), where 0 indicates a dijet structure and 1 indicates an isotropic structure. In contrast to this the ALICE data points shows that sphericity still approximatly continuously acompained by an soft increase in the $< p_T >$ (see Fig. 3.8). The mean shericity seems to depend mainly in the multiplicity and not in the $\sqrt{s}$ (see Fig. 3.9). Where also it suggests that tunnings to generators should include sphericity as a reference.

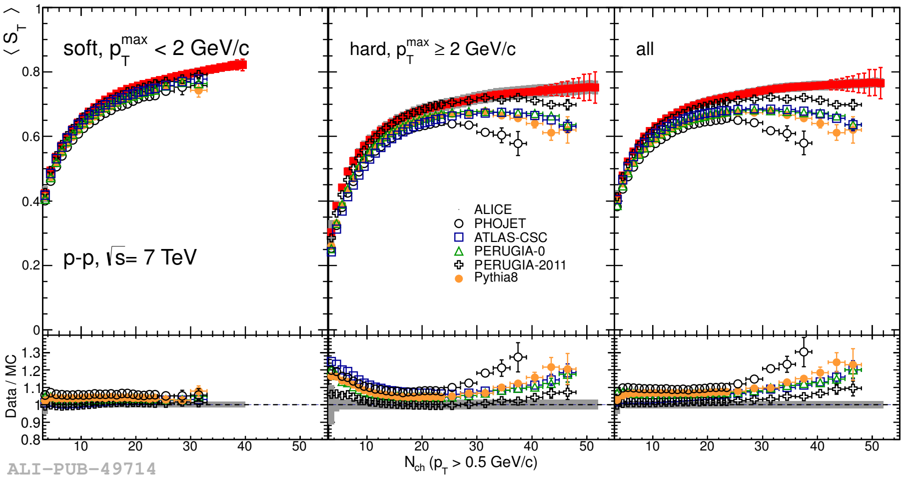

Figure 3.8: Mean transverse sphericity for soft events, hard and all the sample as function of N_{ch} for data and MC [92].

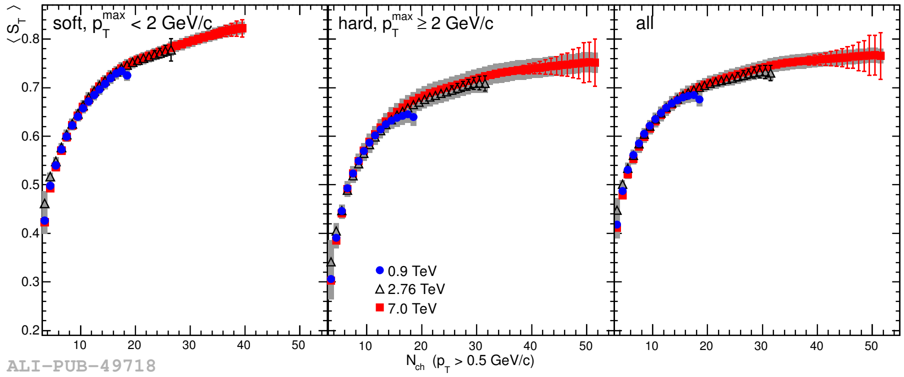

Figure 3.9: Mean transverse sphericity for soft, hard events and for inclusive case as function of N_{ch} in pp collisions at $\sqrt{s} = 0.9$, 2.76, and 7 TeV [92].

Chapter 4

New tool to unveil the new phenomena in small systems

> Measure what can be measured and make measurable what is not.
>
> (Galileo Galilei)

In small systems it is important to recognize that during the interpretation of results in data, there exist some issues related with for example biases due to the event selection. Now in this chapter we are going to discuss some results obtained and published in the Journal Physics G [34] which show the importance to use some tools that allow us to have good control of the jet content. The problems with jets is that they can give false signals of radial flow. As we will see during the pages of this chapter how we make a study employing a jet finder in simulated events with two generators, one called Epos which include QGP effects within the hydrodynamical evolution using the so-called core-corona separation, and another generator Pythia which contains only pure partonic interactions as color reconnection and no hydrodynamical evolution that also produce radial flow signals. This chapter will give a motivation to introduce event shapes as new tool (optional to jet finder) which can be used to separate events with jet content and without them, to make a more differential analysis taking away this fake flow signals as will be discused in the chapter of data analysis.

4.1 The source of the radial flow patterns in MC models

The study of particle production in high-multiplicity events in small collision systems at the LHC has revealed unexpected new collective-like phenomena. In particular, for high-multiplicity proton–proton (pp) and proton–lead (p-Pb) collisions, radial flow signals [187, 185], long-range angular correlations [184, 193], and the strangeness enhancement [29, 191, 194] have been reported. Those effects are well-known in heavy-ion collisions, where they are attributed to the existence of the strongly interacting Quark-Gluon Plasma (QGP) [195, 156, 186]. Understanding the phenomena is crucial because, for heavy-ion physics, pp and p-Pb collisions have been used as the baseline ("vacuum") to extract the genuine QGP effects. However, it is worth mentioning that no jet quenching effects have been found so far in p-Pb collisions [196], suggesting that other mechanisms could also play a role in producing collective-like behavior in small collision systems [160, 197].

Hydrodynamic calculations reproduce many of the observations qualitatively [19]. However, it has also been found that multi-parton interactions (MPI) [20] and color reconnection (CR) as implemented in Pythia [22] produce radial flow patterns via boosted color strings [24]. Moreover, within the dilute-dense limit of the color glass condensate, it has been demonstrated that the physics of fluctuating color fields can generate azimuthal multi-particle correlations [25]; and the mass ordering of elliptic flow when the fragmentation implemented in

PYTHIA is included [26]. The same observable has been studied using the multi-phase transport model [27], where the ridge structure can be generated assuming incoherent elastic scatterings of partons and the string melting mechanism. Other mechanisms like “color ropes”, which are formed by the fusion of color strings close in space, can increase both the strangeness production and the radial flow-like effects [28].

The measurements of the transverse momentum (p_{T}) spectra of identified particles as a function of event multiplicity in pp collisions at the LHC [29, 30] have shown that models fail to describe the data quantitatively. Therefore, the results of those comparisons alone are not enough to give desired information about the origin of the observed effects (i.e. radial flow-like patterns). In order to extract more information, we propose the implementation of a differential study based on the classification of the events according to event multiplicity and the jet content.

In the so-called MPI-based model of color reconnection [22], the interaction between scattered partons at soft and at hard p_{T} scales is imposed as follows. All gluons of low-p_{T} interactions can be inserted onto the colour-flow dipoles of a higher-p_{T} one, keeping the total string length as short as possible. Since the probability of having a hard scattering increases with the number of MPI, color reconnection can give a strong correlation between the radial flow-like patterns and the hard component of the collision in high-multiplicity events.

On the contrary, in the scenario where the hydrodynamical evolution of the system is the prime mechanism, jets are not expected to strongly modify the radial flow patterns. Albeit hard partons cannot thermalize, momentum loss of jets could affect the fluid dynamic evolution of the medium. However, the effect has been studied for heavy-ion collisions and it was found to give only a minor correction [202]. In the present paper we argue that by exploiting such a fundamental difference between both models, one might say whether or not the observed effects are driven by hydrodynamics. To this end, we propose a systematic study by analyzing the mid-rapidity ($|y| < 1$) inclusive p_{T} spectra of identified charged hadrons as a function of the mid-pseudorapidity ($|\eta| < 1$) event multiplicity (N_{ch}) and transverse momentum of the leading jet ($p_{\mathrm{T}}^{\mathrm{jet}}$). This study was carried out using PYTHIA 8.212 and EPOS 3.117 Monte Carlo (MC) event generators, from now on referred to as PYTHIA 8 and EPOS 3, respectively.

4.1.1 FastJet 3.1.3 and hardness of the event

Besides the multiplicity selection, we also classify events based on the transverse momentum ($p_{\mathrm{T}}^{\mathrm{jet}}$) of the produced jets. Per event, jets are reconstructed with the well-known anti-k_{T} algorithm implemented in FASTJET 3.1.3 [203], using charged and neutral particles, considering a cone radius of 0.4 and a minimum transverse momentum $p_{\mathrm{T,min}}^{\mathrm{jet}} = 5\,\mathrm{GeV}/c$. The lower requirement on the jet p_{T} acts to suppress soft interactions by ensuring that at least one semi-hard scattering is present within the acceptance. In the following, the jet searching is done within a given pseudorapidity interval, which defines the maximum pseudorapidity of the jet. It is important to highlight that FASTJET is a well-known tool for jet reconstruction in heavy-ion collisions, where it has been extensively used, even in most central Pb-Pb collisions.

4.2 Multiplicity dependence of the leading jet p_{T}

By running FASTJET (considering cone radius 0.4, $|\eta| < 1$ and $p_{\mathrm{T,min}}^{\mathrm{jet}} = 5\,\mathrm{GeV}/c$) over the sample generated with PYTHIA 8 we obtained the results for the average mid-pseudorapidity densities, presented in Table 4.1. Going from $\langle \mathrm{d}N_{\mathrm{ch}}/\mathrm{d}\eta \rangle = 2.12$ to $\langle \mathrm{d}N_{\mathrm{ch}}/\mathrm{d}\eta \rangle = 46.1$, the average leading jet p_{T} ranges from $7.09\,\mathrm{GeV}/c$ up to $19.7\,\mathrm{GeV}/c$. A similar behavior was found for the leading parton transverse momentum, obtained at mid-pseudorapidity, as a function of $\langle \mathrm{d}N_{\mathrm{ch}}/\mathrm{d}\eta \rangle$. The effect is explained in the context of multi-partonic interactions because the probability of finding a hard parton is expected to be larger in high-multiplicity events (large average N_{mpi}) than in low-multiplicity events (small average N_{mpi}). This effect is also reflected in the behavior of the fraction of events having at least one jet with momentum above $5\,\mathrm{GeV}/c$. In the second column of Tab 4.1 we included the corresponding event multiplicity class in comparison to the other measured variables. For the presented results we considered events having z from the lowest possible value ($0 < z < 1$) up to $5 < z < 6$.

$\left\langle \frac{\mathrm{d}N_{\mathrm{ch}}}{\mathrm{d}\eta} \right\rangle_{\vert\eta\vert<1}$	$\frac{\mathrm{d}\,N_{\mathrm{ch}}/\mathrm{d}\,\eta}{\langle \mathrm{d}\,N_{\mathrm{ch}}/\mathrm{d}\,\eta\rangle_{\vert\eta\vert<1}}$ $(\equiv z)$	$\langle p_{\mathrm{T}}^{\mathrm{jet}}\rangle_{\vert\eta\vert<1}$ (GeV/c)	% of events with $p_{\mathrm{T}}^{\mathrm{jet}} > 5\,\mathrm{GeV}/c$
2.12	$0 < z < 1$	7.09	1.03
8.12	$1 < z < 2$	7.49	13.1
13.6	$2 < z < 3$	7.83	37.3
19.0	$3 < z < 4$	8.48	63.7
24.4	$4 < z < 5$	9.56	83.2
29.8	$5 < z < 6$	11.1	93.9
35.2	$6 < z < 7$	13.2	98.2
40.6	$7 < z < 8$	16.1	99.5
46.1	$8 < z < 9$	19.7	99.8

Table 4.1: Charged-particle pseudorapidity densities at central pseudorapidity ($|\eta| < 1$), for pp collisions at $\sqrt{s} = 7\,\mathrm{TeV}$ simulated with Pythia 8 having jets with p_{T} above $5\,\mathrm{GeV}/c$ in the same pseudorapidity region. The multiplicity classes are presented along the leading jet p_{T} and the fraction of events where a jet with p_{T} above $5\,\mathrm{GeV}/c$ was identified.

One can see that for the highest considered z interval ($5 < z < 6$) more than 90 % of the events contain jets with $p_{\mathrm{T}}^{\mathrm{jet}} > 5\,\mathrm{GeV}/c$. This feature is simply the result of the selection bias, i.e. the higher the multiplicity at mid-pseudorapidity the higher the probability to find jets within the same η region.

4.2.1 Proton-to-pion ratio as a function of z and $p_{\mathrm{T}}^{\mathrm{jet}}$

Figure 4.1 shows the proton-to-pion ratio as a function of p_{T} for event classes with low and high z. Regarding the low-z case ($0 < z < 1$), results indicate that for $5 < p_{\mathrm{T}}^{\mathrm{jet}} < 10\,\mathrm{GeV}/c$ the ratios exhibit an enhancement at $p_{\mathrm{T}} \approx 3\,\mathrm{GeV}/c$ for both Epos 3 and Pythia 8. If the $p_{\mathrm{T}}^{\mathrm{jet}}$ is increased then the position of the observed peak is shifted to higher p_{T}. This observation suggests that the peak is not an exclusive effect of radial flow (as suggested by Fig. 1.7), but also a feature of the fragmentation. It is worth noticing that the same effect has been observed in ALICE data, where the jet hadrochemistry has been measured in minimum bias pp collisions at $\sqrt{s} = 7\,\mathrm{TeV}$ [199].

Also shown in Fig. 4.1 the multiplicity class $5 < z < 6$, where we see that the maximum of the proton-to-pion ratio increases with increasing multiplicity, showing significantly stronger behavior for Epos 3 than for Pythia 8. In Epos 3, the event class $5 < p_{\mathrm{T}}^{\mathrm{jet}} < 10\,\mathrm{GeV}/c$ exhibits an enhancement of the $(\mathrm{p}+\bar{\mathrm{p}})/(\pi^{+}+\pi^{-})$ ratio with respect to the inclusive case shown in Fig. 1.7 without any selection on $p_{\mathrm{T}}^{\mathrm{jet}}$. Going to higher $p_{\mathrm{T}}^{\mathrm{jet}}$, the position of the peak is shifted to lower p_{T} values and the magnitude of the peak is significantly smaller than in the inclusive case. In contrast, the effect is quantitatively and qualitatively different in Pythia 8. Namely, the height of the peak is approximately independent of the increase of $p_{\mathrm{T}}^{\mathrm{jet}}$, instead, there is a moderate shift towards higher p_{T}. In Epos 3, the effect vanishes when hydrodynamical effects are switched off − in a similar way as seen in Fig. 1.7(b). Therefore, it can be a consequence of the "core-corona" separation, where low-momentum partons are more likely forming the "core" region. It is worth mentioning that this difference between the two event classes could contribute to the differences observed in the hadrochemistry measured in the so-called "bulk" (outside the jet peak) and the jet regions in p-Pb and Pb-Pb collisions at the LHC [200, 201]. To summarize, an analysis of data as a function of event multiplicity and the hardness of the event provides a more powerful tool for testing the aforementioned models than the one which considers selection based only on event multiplicity.

4.3 Blast-wave Analysis in MC models

Color reconnection, without any hydrodynamical component, produces radial flow-like patterns in events simulated with Pythia 8, as shown in Ref. [24]. Such a conclusion was based on the good agreement between the

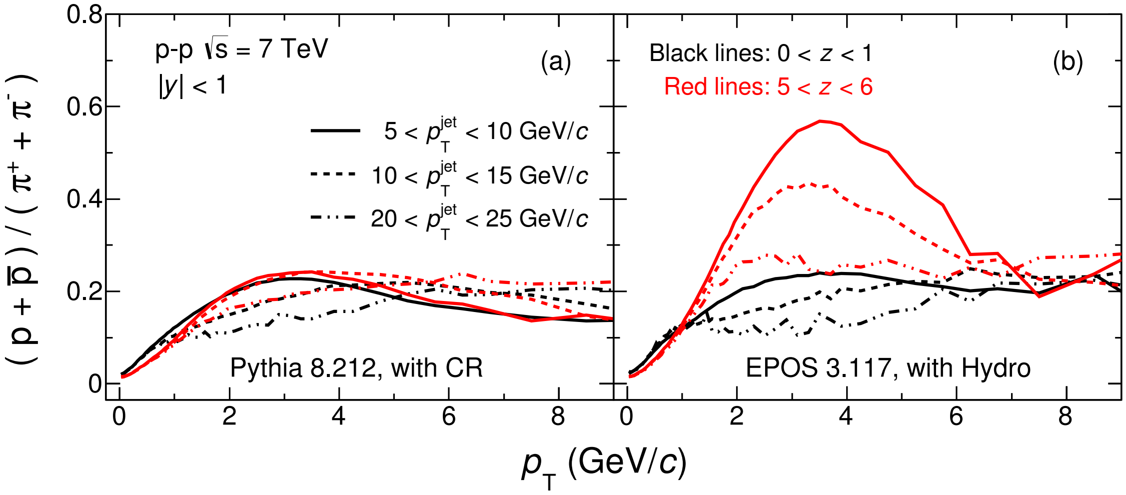

Figure 4.1: (Color online) Proton-to-pion ratio as a function of p_{T} for two multiplicity classes, $0 < z < 1$ (black lines) and $5 < z < 6$ (red lines); and for different $p_{\mathrm{T}}^{\mathrm{jet}}$ intervals. Results are shown for both (a) Pythia 8 and (b) Epos 3.

Boltzmann–Gibbs blast-wave model and the p_{T} spectra of different particle species.

From the simultaneous fit of the blast-wave model to the p_{T} spectra of different particle species we extract two parameters: T_{kin} and $\langle\beta_{\mathrm{T}}\rangle$. In the current study we considered the p_{T} ranges: $0.5 < p_{\mathrm{T}} < 1.0\,\mathrm{GeV}/c$, $0.3 < p_{\mathrm{T}} < 1.5\,\mathrm{GeV}/c$ and $0.8 < p_{\mathrm{T}} < 2.0\,\mathrm{GeV}/c$ to fit the model to the p_{T} distributions of charged pions, kaons and (anti)protons, respectively. The specific selection of the p_{T} ranges mentioned above was successfully applied in our previous studies [16] where the parametrizations, obtained from the fits, described within 10 % the strange and multi-strange hadron p_{T} spectra.

For pp collisions at $\sqrt{s} = 7\,\mathrm{TeV}$ simulated with Pythia 8, Fig. 4.2 shows the p_{T} spectra of charged pions, kaons and (anti)protons for two multiplicity classes, $0 < z < 1$ (upper panel (a)) and $5 < z < 6$ (lower panel (b)), being each one split into three specific subclasses based on the selection of the jet transverse momentum, $p_{\mathrm{T}}^{\mathrm{jet}}$. The first subclass is treated as a baseline since no jets at mid-pseudorapidity are found; it is compared with samples in which low (5–10 GeV/c) and high (20–25 GeV/c) p_{T} jets are produced. For a given average multiplicity z class and jet transverse momentum $p_{\mathrm{T}}^{\mathrm{jet}}$ interval two cases are considered: with and without color reconnection.

There are some interesting observations one might read off from the results of this analysis. Firstly, we concentrate on results obtained from Pythia 8 simulations, since we already know we might expect the presence of radial flow patterns. Then we shall be examining the results produced by Epos 3.

Even at extremely low multiplicity ($0 < z < 1$), where color reconnection effects are negligible, it is possible to find an event class where the radial flow-like patterns pop up. Specially, in events having $p_{\mathrm{T}}^{\mathrm{jet}} > 5\,\mathrm{GeV}/c$ the p_{T} distributions of identified hadrons are better described by the blast-wave model than in those without jets. Looking at differences between the model fit and the MC result in terms of ratios (shown in the bottom rows of Fig. 4.2(a)) one can see a smoothening trend with p_{T} when going towards higher $p_{\mathrm{T}}^{\mathrm{jet}}$ which is hardly visible for pions but more pronounced for kaons and (anti)protons. This behavior is also supported by the reduction on the reduced χ^2 values: fit results give $\chi^2/\mathrm{n.d.f} = 3.28$ (4.65) for events without jets and $\chi^2/\mathrm{n.d.f} = 1.51$ (1.09) for events including jets with $20 < p_{\mathrm{T}}^{\mathrm{jet}} < 25\,\mathrm{GeV}/c$ for the case with (without) color reconnection, respectively. It is worth mentioning that recently the CMS Collaboration has reported that in low-multiplicity pp events, the elliptic flow Fourier harmonic is not zero [193], supporting the idea that other mechanisms could produce the collective-like behavior.

In high-multiplicity events ($5 < z < 6$), again, examining the relative differences between the spectra and the fits, the overall agreement between the spectra and the blast-wave fits shows a smaller dependence with

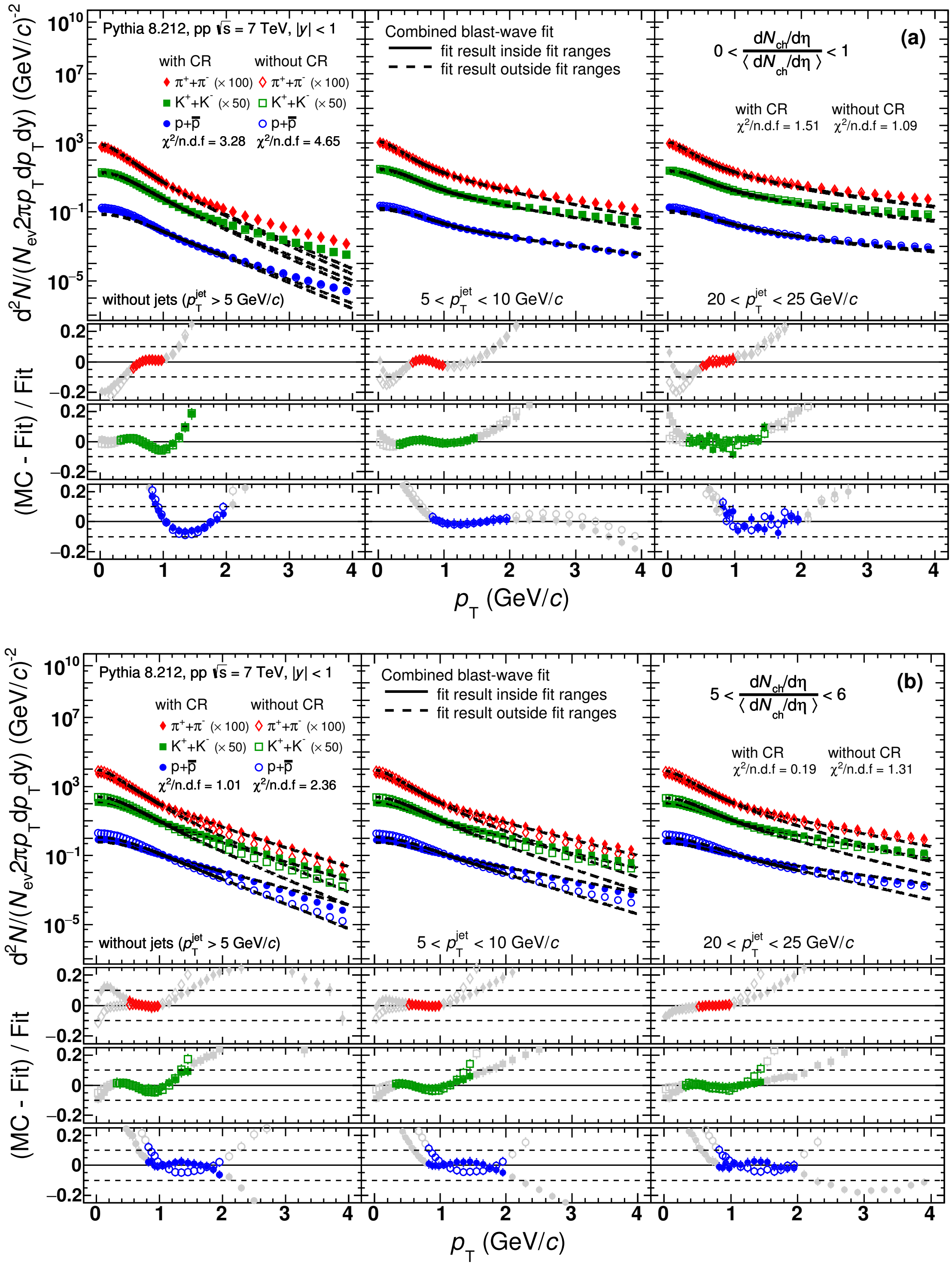

Figure 4.2: (Color online) Transverse momentum distributions of charged pions, kaons and (anti)protons for (a) low- and (b) high-multiplicity pp collisions at $\sqrt{s} = 7\,\mathrm{TeV}$ generated with Pythia 8. For each multiplicity class, three sub-samples are shown, from left to right, events without a leading jet with $p_{\mathrm{T}}^{\mathrm{jet}} > 5\,\mathrm{GeV}/c$, with $5 < p_{\mathrm{T}}^{\mathrm{jet}} < 10\,\mathrm{GeV}/c$ and with $20 < p_{\mathrm{T}}^{\mathrm{jet}} < 25\,\mathrm{GeV}/c$, respectively. Results for the cases with and without color reconnection (CR) are plotted with full and empty markers, respectively.

$p_{\mathrm{T}}^{\mathrm{jet}}$. The blast-wave model fits give a slightly worse description of the spectra when CR is not included in the simulation − even if a jet with $p_{\mathrm{T}}^{\mathrm{jet}} > 5\,\mathrm{GeV}/c$ is produced at mid-rapidity − than for the case with the inclusion of CR. The ratios of spectra (simulated with CR) to blast-wave model show a modest smoothening trend with increasing $p_{\mathrm{T}}^{\mathrm{jet}}$ while those without CR stay approximately $p_{\mathrm{T}}^{\mathrm{jet}}$-independent. These observations are confirmed by the fit qualities in terms of reduced χ^2 values: $\chi^2/\mathrm{n.d.f} = 1.01$ (2.36) for events without jets and $\chi^2/\mathrm{n.d.f} = 0.19$ (1.31) for events including jets ($20 < p_{\mathrm{T}}^{\mathrm{jet}} < 25\,\mathrm{GeV}/c$) for the case with (without) color reconnection. The observed effects just reflect the fact that in PYTHIA 8 the interaction between jets and the underlying event is crucial for generating a collective-like behavior.

Shown in Fig. 4.3 the results obtained from the blast-wave analysis of the p_{T} spectra simulated with EPOS 3. In general, the observed effects are quite similar to those shown for PYTHIA 8 (Fig. 4.2), even though the statistics is notably limited for jets with higher $p_{\mathrm{T}}^{\mathrm{jet}}$. In low-multiplicity events with no jets produced (Fig. 4.3(a) left column) charged kaons show worse model description than those seen for PYTHIA 8 (Fig. 4.2(a) left column) which are similar in shape and magnitude to (anti)protons. Also, the corresponding χ^2 values are remarkably higher in events without jets simulated with (without) hydrodynamical evolution, i.e. $\chi^2/\mathrm{n.d.f} = 5.55$ (9.18), than in those simulated with (and without) color reconnection in PYTHIA 8.
Low-z p_{T} spectra in EPOS 3 for all particle species are better described by the blast-wave model. It is noteworthy that it is hard to make strong conclusion for the highest $p_{\mathrm{T}}^{\mathrm{jet}}$ event class due to its limited statistics, but the points tend to show similar behavior compared to the former event class with jets $5 < p_{\mathrm{T}}^{\mathrm{jet}} < 10\,\mathrm{GeV}/c$.
In high-z events, the model description of the p_{T} spectra show the same behavior seen in PYTHIA 8. Namely, with the inclusion of hydrodynamical component in the simulation, the agreement is somewhat better for the case with the hydro option. Besides that, there is a clear dependence seen between the two options (shown with full and open markers) also for charged pions and kaons. The p_{T} spectra have a weak $p_{\mathrm{T}}^{\mathrm{jet}}$-dependent behavior and their agreement with the blast-wave model improves towards higher $p_{\mathrm{T}}^{\mathrm{jet}}$, with the change of $\chi^2/\mathrm{n.d.f}$ from 1.33 (6.74) to 0.77 (1.29) as we consider events with (without) setting hydro option, respectively.

To quantify the importance of jets in events where flow patterns are generated with hydrodynamics or color reconnection, Fig. 4.4 shows the correlation between the blast-wave parameters T_{kin} and $\langle\beta_{\mathrm{T}}\rangle$. Results are shown for different z multiplicity classes which are indicated by different marker sizes and increase from low to high multiplicity. Besides the multiplicity selection, also shown the case when we consider the selection on the hardness of the event by imposing a cut on $p_{\mathrm{T}}^{\mathrm{jet}}$.
In continuation to the previous observation based on the fit qualities for various event classes in PYTHIA 8 and in EPOS 3, by looking at the evolution of the blast-wave fit parameters in terms of z and $p_{\mathrm{T}}^{\mathrm{jet}}$ we see that:

- For events containing jets and being in the same multiplicity class (indicated by the same marker size), $\langle\beta_{\mathrm{T}}\rangle$ increases with respect to the case without any selection on the hardness (inclusive case indicated by open markers). This is a somewhat natural consequence of the auto-correlation bias due to hard partons inducing a large boost. Moreover, by looking at, the case of jets with $20 < p_{\mathrm{T}}^{\mathrm{jet}} < 25\,\mathrm{GeV}/c$ and the highest multiplicity class ($5 < z < 6$), the effect is weaker in EPOS 3 ($\approx 0.6\,\%$) than in PYTHIA 8 ($\approx 6.8\,\%$). Implicitly, this is also illustrated in the smaller multiplicity dependence of $\langle\beta_{\mathrm{T}}\rangle$ obtained in PYTHIA 8 than that observed in EPOS 3 where the role of jets is considerably weaker.

- In low-z events (as explained earlier) the p_{T} spectra deviate from the blast-wave model − in constrast to events with higher z − and the agreement improves with increasing $p_{\mathrm{T}}^{\mathrm{jet}}$. In connection to those observations, taking low-z parameters in Fig. 4.4 we see a weak $p_{\mathrm{T}}^{\mathrm{jet}}$ dependence as a function of $\langle\beta_{\mathrm{T}}\rangle$ in EPOS 3 whereas in PYTHIA 8 for a given low-z class events with increasing $p_{\mathrm{T}}^{\mathrm{jet}}$ experience a larger radial flow velocity $\langle\beta_{\mathrm{T}}\rangle$. In addition, one sees that in PYTHIA 8 the larger the $\langle\beta_{\mathrm{T}}\rangle$ the smaller the T_{kin} reaching at slightly smaller values for the highest z class than those in EPOS 3 where the T_{kin} dependence of $\langle\beta_{\mathrm{T}}\rangle$ is almost flat.

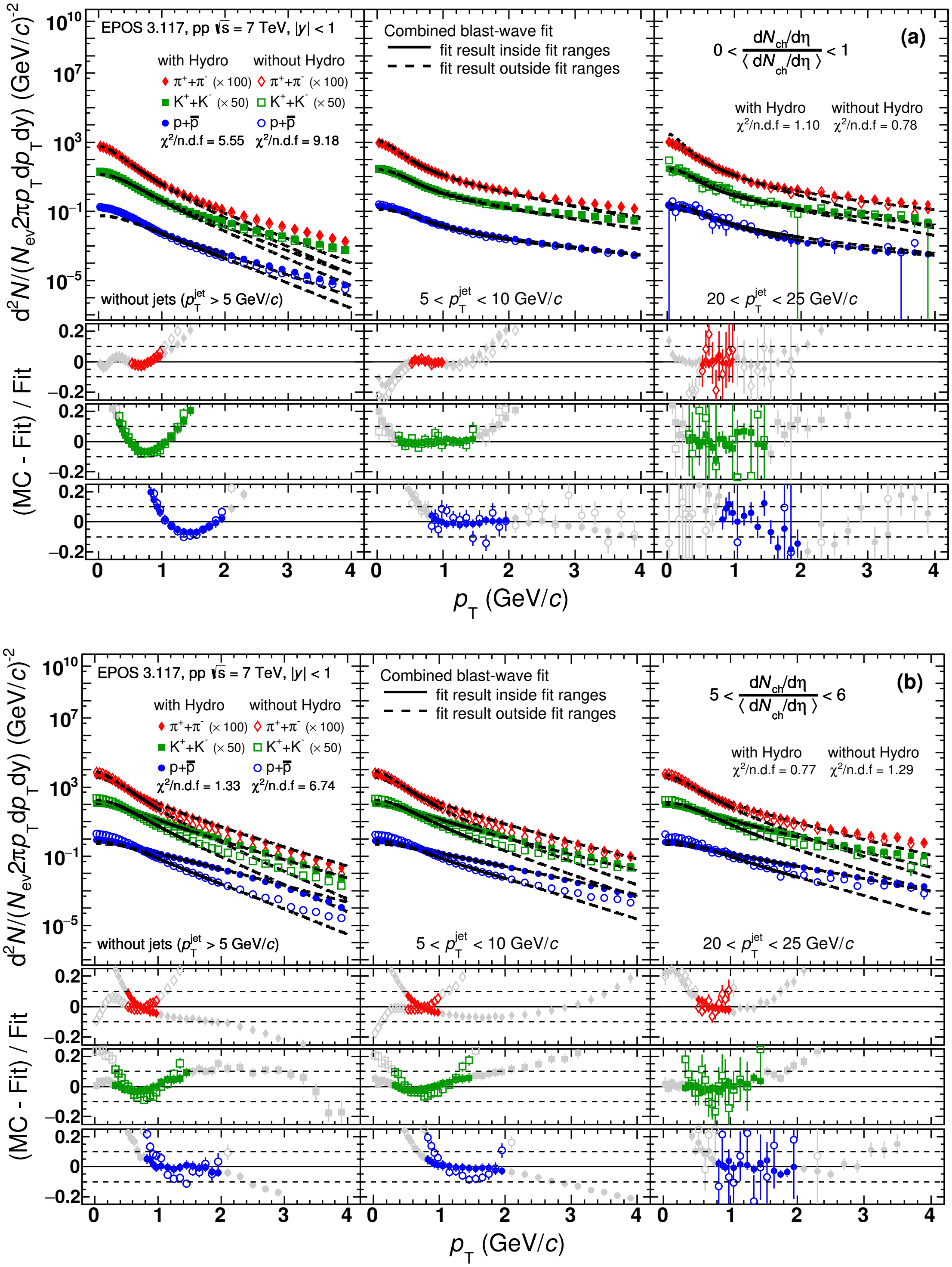

Figure 4.3: (Color online) Transverse momentum distributions of charged pions, kaons and (anti)protons for (a) low- and (b) high-multiplicity pp collisions at $\sqrt{s} = 7\,\mathrm{TeV}$ generated with EPOS 3. For each multiplicity class, three sub-samples are shown. From left to right, events without a leading jet with $p_{\mathrm{T}}^{\mathrm{jet}} > 5\,\mathrm{GeV}/c$, with $5 < p_{\mathrm{T}}^{\mathrm{jet}} < 10\,\mathrm{GeV}/c$ and with $20 < p_{\mathrm{T}}^{\mathrm{jet}} < 25\,\mathrm{GeV}/c$, respectively. Results for the cases with and without hydrodynamics (hydro) are plotted with full and empty markers, respectively.

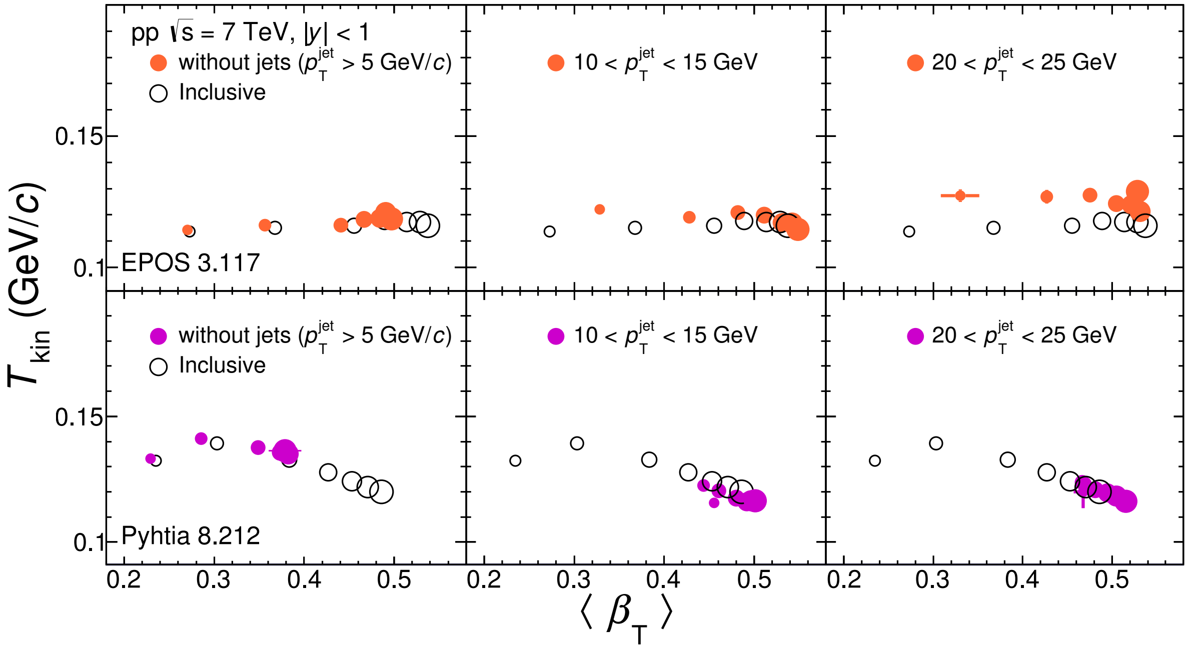

Figure 4.4: (Color online) Correlation between two fit parameters obtained from the blast-wave analysis, the kinetic temperature ($T_{\rm kin}$) and the average transverse expansion velocity ($\langle\beta_{\rm T}\rangle$) of the system. Results for pp collisions at $\sqrt{s}$ = 7 TeV simulated with EPOS 3 and PYTHIA 8 are presented in the top and the bottom rows, respectively. The size of the markers increases with the event multiplicity. Results with (full markers) and without (empty markers) a selection on $p_{\rm T}^{\rm jet}$ are compared.

4.4 The importance to use additional tools to separate jet effects.

In this work, we have presented a study using two event generators, EPOS 3 and PYTHIA 8, exploring an observable which is aimed at ruling out or validating the underlying physics mechanism (hydrodynamics or color reconnection) for generating radial flow patterns in pp collisions. Specifically, we exploit the fact that, by construction, color reconnection produces a strong coupling between the hard (hard partons) and soft (soft and semi-hard partons) components of the interaction. To this end, we have studied the p_{T} spectra of charged pions, kaons and (anti)protons as a function of the event multiplicity and the transverse momentum of the leading jet. Our main findings can be summarized as follows:

- The multiplicity dependence of the proton-to-pion particle ratios show a depletion for $p_{\mathrm{T}} \lesssim 1-2\,\mathrm{GeV}/c$ and an enhancement above, ending up with a bump at around $p_{\mathrm{T}} \approx 3\,\mathrm{GeV}/c$. Apart from the multiplicity selection, a more differential classification was done by using the leading jet transverse momentum ($p_{\mathrm{T}}^{\mathrm{jet}}$). At extremely low multiplicity, it is possible to find a subclass of events where radial flow patterns arise − despite the fact that at very low multiplicity − hydrodynamics cannot be applied and color reconnection effects are small. This feature is present both for PYTHIA 8 and EPOS 3.
- In high-multiplicity events the particle composition is very different in PYTHIA 8 and EPOS 3 which is nicely visible on the proton-to-pion ratios when multiplicity and $p_{\mathrm{T}}^{\mathrm{jet}}$ vary. In EPOS 3 the magnitude of the bump significantly increases with decreasing $p_{\mathrm{T}}^{\mathrm{jet}}$. On the contrary, in PYTHIA 8 the height of the peak does not change with $p_{\mathrm{T}}^{\mathrm{jet}}$.
- Furthermore, the agreement between the blast-wave model and the charged pion, kaon and (anti)proton spectra in events classified using multiplicity and $p_{\mathrm{T}}^{\mathrm{jet}}$, significantly improves with the increase of the leading jet p_{T}. More importantly, this agreement was found to be the best in low-multiplicity events having jets, suggesting the presence of the collective-like behavior caused by jets.
- The multiplicity and jet transverse momentum dependence of the blast-wave fit parameters, i.e. the average transverse expansion velocity ($\langle\beta_{\mathrm{T}}\rangle$) and the kinetic temperature (T_{kin}), also shows effects which can be used to discriminate between different models. It is found that the multiplicity dependence of $\langle\beta_{\mathrm{T}}\rangle$ is more affected by jets in PYTHIA 8 than in EPOS 3.

Chapter 5

Event shapes studies in ALICE

> An expert is a person who has made all the mistakes that can be made in a narrow field
>
> ---
>
> Niels Bohr

As mention in the last chapter from the motivation of the published paper [34], this chapter is fully dedicated to the spherocity analysis for the $\langle p_{\mathrm{T}} \rangle$ vs multiplicity correlations obtained for pp collisions at 13 TeV data, which chapter is also based on the analisis note [32], and which results has been approved to set into an ALICE publication [205].

5.1 Data analysis

For the data analysis the data set, event and track selection, correction procedure and the analysis method will be discused in detail. A total of about 59 million events were used [32] in this analysis.

Dataset

Period LHC15f pass2 (59 million events, 45 million events after selection). We use the following 49 runs [33]. They are marked as good runs in the run condition table (RCT) and have low pile up ($\mu < 1$):

> 226500, 226495, 226483, 226476, 226472, 226468, 226466, 226452, 226445, 226444, 226225, 226220, 226170, 226062, 225768, 225766, 225763, 225762, 225757, 225753, 225719, 225717, 225716, 225710, 225709, 225708, 225707, 225587, 225586, 225582, 225580, 225579, 225578, 225576, 225322, 225314, 225313, 225309, 225307, 225305, 225106, 225052, 225051, 225050, 225043, 225041, 225037, 225035, 225031.

Monte Carlo

In this work we use the MC productions PYTHIA 6 Perugia 2011[1] (36 million events), PYTHIA 8 Monash 2013[2] (55 million events) and EPOS-LHC[3] (39 million events), this are LHC15f pass2 anchored samples.

Event selection

We use the event selection following the recommendations for the analysis of run II data [32]:

---

[1] period LHC15g3c3.

[2] period LHC15g3a3.

[3] period LHC16d3.

- Standard physics selection, for selecting minimum bias (MB) pp events. This selection corresponds to a logical AND between trigger inputs from VZEROA and VZEROC and it is based on VZERO timing signal and the correlation between the number of hits and tracklets in the SPD (kINT7).
- We cut on the correlation between SPD clusters and tracklets: $if(fNofITSClusters0 + fNofITSClusters1 > 65 + 4 * fNofTracklets) \quad return;$
- SPD Pile-up rejection. After finding the first vertex, the tracklets which are not pointing to this "main" vertex are used to check if there are other vertices originating particles. $AliESDevent :: IsPileupFromSPD();$
- Minimum multiplicity, transverse spherocity is defined for events having more than two tracks with transverse momenta above 0.15 GeV/c and within $|\eta| < 0.8$.
- $AliESDEvent :: IsIncompleteDAQ$, removes all the runs which have incomplete data acquisition quality (DAQ).

Track selection for the average p_{T} vs multiplicity analysis

For p_{T} analysis the next track cuts were used:

- Distance of closest approach (DCA) in the z direction, $|DCA_z|$ <2 cm.
- $\mathrm{DCA}_{xy} < 0.0105 + 0.035/p_{\mathrm{T}}^{1.01}$ cm
- number of crossed rows in the TPC>70
- ratio of crossed rows over number of findable clusters in the TPC>0.8
- fraction of shared TPC clusters<0.4
- χ^2 per TPC cluster<4
- no kinks
- TPC refit require
- ITS refit require
- at least one hit in the SPD
- χ^2 per ITS cluster<36

Track selection for transverse spherocity

Global tracks which satisfy the TPC-only track cuts and TPC refit were considered [33]. In addition, the following cuts were imposed: $|\eta|$ <0.8 and p_{T} >0.15 GeV/c.

Multiplicitiy estimator

For the analysis we have used the reference multiplicity estimator described below:

- Reference multiplicity: takes the number of global tracks plus the complement from ITS-SA tracks plus the complement from ITS tracklets to estimate the multiplicity at mid-pseudorapidity, $|\eta| < 0.8$, this is applied using the next snippets:

AliESDtrackCuts::GetReferenceMultiplicity(esdEvent, AliESDtrackCuts::kTrackletsITSTPC, fEtaAbsCutUp); The binning used is the one used in [33, 32], i.e. a bin size one.

Measurements have been reported using the multiplicity estimator based on the VZERO detectors (V0M), however, for the event shape analysis the application of such an estimator would introduce another degree of freedom in the interpretation of the results. Namely, a V0M multiplicity class would give a broad multiplicity distribution at mid-pseudorapidity. Since event shape uses the tracking at mid-rapidity, then events with high spherocity would select the highest mid-rapidity multiplicity events because event shapes have an implicit dependence on multiplicity. Figure 5.1 shows the correlation: spherocity vs mid-pesudorapidity ($|\eta|<0.8$) multiplicity for the 1-5% V0M multiplicity class. The left hand side plot shows the number of entries on the z axis. Clearly, we reach $\langle \mathrm{d}N_{\mathrm{ch}}/\mathrm{d}\eta \rangle \approx 21$, and both two distributions, spherocity and multiplicity, are wide. In order to see the average multiplicity associated to pencil-like and isotropic events, the right hand side plot shows the same correlation, but in this case for each S_0 bin, the multiplicity distribution has been normalized to one. The average mean multiplicity as a function of spherocity is plotted using black markers. We observe that going from pencil-like ($S_0 \to 0$) to isotropic ($S_0 \to 1$) events the average multiplicity increases. Therefore, an analysis using V0M, should consider on top of the spherocity selection, the effect of the second selection on multiplicity. For this reason, we decided to use the estimator at mid-pseudorapidity and also a bin size equal to one, in order to guarantee the same multiplicity but different event shape.

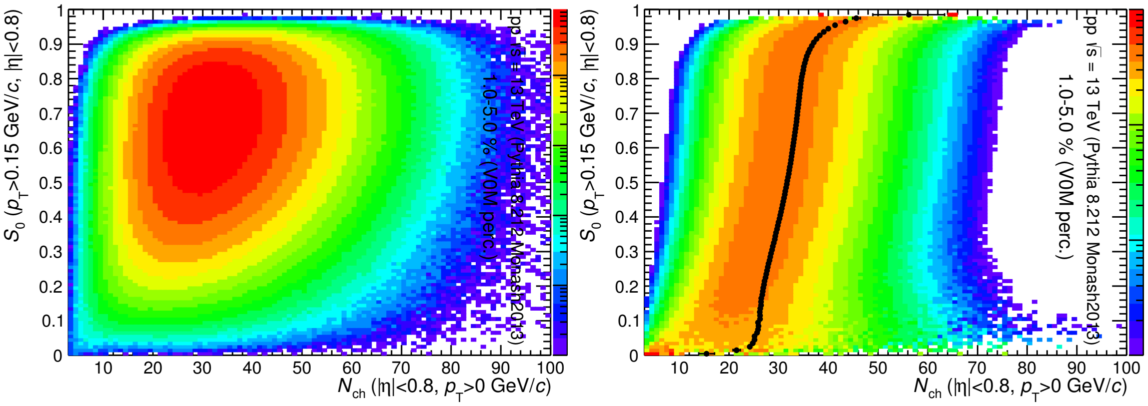

Figure 5.1: Transverse spherocity as a function of the mid-pseudorapidity charged multiplicity for a high multiplicity class defined in close analogy to the ALICE V0M estimator. The left hand side plot shows the number of events on the z axis. The right hand side plot has been normalized in such a way that each spherocity bin has integral one, there, the black markers indicate the average mid-pseduorapididty multiplicity as a function of spherocity.

5.2 Correction procedures

For the analysis some corrections have been applied [32], the corrections were implemented as follows:

1. The p_{T} spectra are obtained in bins of measured multiplicity (N_{m}) and measured spherocity (S_0^{m}).

2. The spectra are further corrected for efficiency and secondaries (we used MB corrections). For corrections we are using the efficiency correction from real particle composition and secondaries from DCA fit.

3. Power law functions are fitted to the spectra (p_{T} >3 GeV/c) in order to avoid statistical fluctuations at high p_{T} . Then, the p_{T} spectra are used to get the average p_{T} ($0.15<p_{\mathrm{T}}<10$ GeV/c) for the specific bins of measured multiplicity and spherocity.

4. The mean p_{T} as a function of multiplicity are corrected by spherocity selection using a weighting average. This correction is inspired in the multiplicity correction developed by the GSI group for the mean p_{T} as a function of multiplicity analysis [32].

5. The new correlations are further corrected by multiplicity using again a weighting average.

5.2.1 Efficiency and Secondaries from Monte Carlo

The correction for the reconstruction (in)efficiency of primary charged particles and for the contamination of our track sample with secondary particles from decays or interaction in the material are based on Monte Carlo information from simulated data using Pythia 6 and Pythia 8 event generators together with the detector simulation and the same reconstruction algorithms that are used for real data.

Figure 5.2 a) shows the efficiency obtained from MC. Different multiplicity classes are displayed. One sees a little or no multiplicity dependence of the tracking efficiency. As discussed above, for data we can not use this efficiency in the analysis of data because we know that particle composition is not well modeled by the generators. Therefore the efficiency that we use is derived from a data driven method discussed below. Also shown in Fig. 5.2 b) the contamination from secondaries obtained from MC. Again, since MC does not describe the strange particle production, we can not use this correction in real data. Instead, another method based on template fits is adopted.

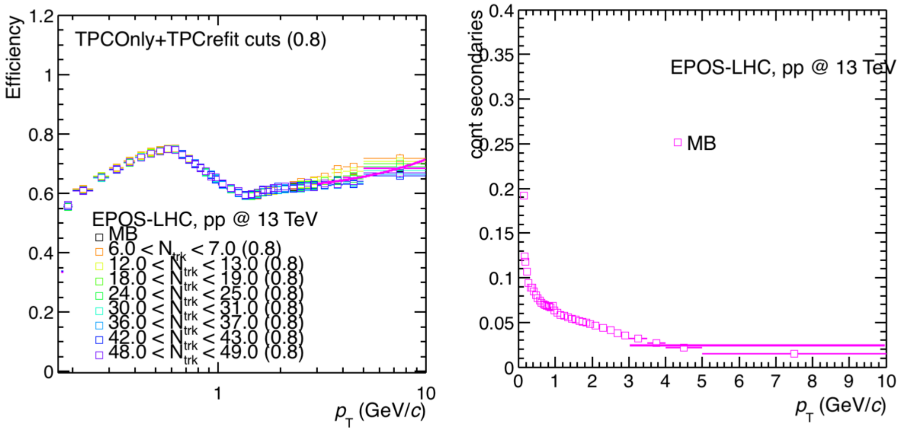

Figure 5.2: a) Transverse momentum efficiency at 13 TeV, using Epos-LHC for different multiplicities, b) secondaries contamination at 13 TeV, using Epos-LHC.

5.2.2 Corrections using data driven approaches

We rescale the MC particle composition according to the the ALICE measurements of identified particles in pp collisions at 7 TeV and use the properly reweighted efficiency to correct the data. This procedure is described in this subsection.

Monte Carlo generators can yet not describe the production of identified charged particles perfectly. Since the detector has different tracking efficiency for all these particle species, the efficiency for inclusive charged particles differ in Monte Carlo simulations and in data. So a data-driven approach is needed to obtain the true tracking efficiency of inclusive charged particles.

The corrected tracking efficiency for inclusive charged particles can be calculated using 5.1:.

$$\epsilon_{\mathrm{PartComp}} = \frac{\sum_{i=\pi,\mathrm{K},\mathrm{p}} \epsilon^{i}_{\mathrm{MC}} \cdot (\mathrm{dN}/\mathrm{d}p^{i}_{\mathrm{T}})_{\mathrm{data}} + \epsilon^{\mathrm{rest}}_{\mathrm{MC}} \cdot (\mathrm{dN}/\mathrm{d}p_{\mathrm{T}})^{\mathrm{rest}}_{\mathrm{MC}}}{\sum_{i=\pi,\mathrm{K},\mathrm{p}} (\mathrm{dN}/\mathrm{d}p^{i}_{\mathrm{T}})_{\mathrm{data}} + (\mathrm{dN}/\mathrm{d}p_{\mathrm{T}})^{\mathrm{rest}}_{\mathrm{MC}}} \tag{5.1}$$

Where ϵ is the efficiency and dN/dp_{T} is denoting the invariant yield per unit of p_{T} and pseudorapidity (this means $(1/N_{ev})(d^2N/dp_{\mathrm{T}}d\eta)$, the upper and lower index denotes the particles species (pions, kaons or protons and the rest for all charged except the ones mentioned before) or if they are from data or Monte Carlo.

In order to proceed, the efficiency also needs to be obtained for different particles species using MC as it is showed in Fig. 5.3, also using the invariant yield from data as seen in Fig. 5.4 a) was used, in order to have the same binning a Levy-Tsallis fit was done (see Fig. 5.4 b)) then the spectra was obtained from extrapolation to the wide p_{T} binning from efficiency (Fig. 5.5 a)) and with this the invariant yield multiplied by the efficiencies for each species (pions, kaons, protons and rest) were also obtained as shown in (Fig. 5.5 b)), then using the expression on equation 5.1, the particle composition efficiency was obtained (black dots in Fig. 5.6 a)) also a comparison from MC efficiency is shown and the ratio between them as shown in Fig. 5.6 b).

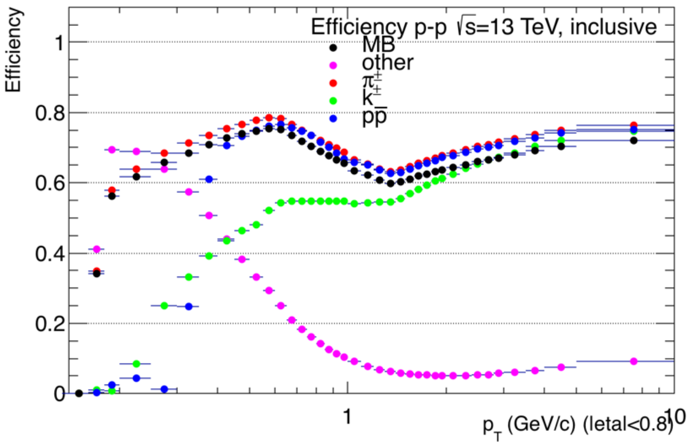

Figure 5.3: Efficiency for particle species pions, kaons protons and rest obtained from Monte Carlo.

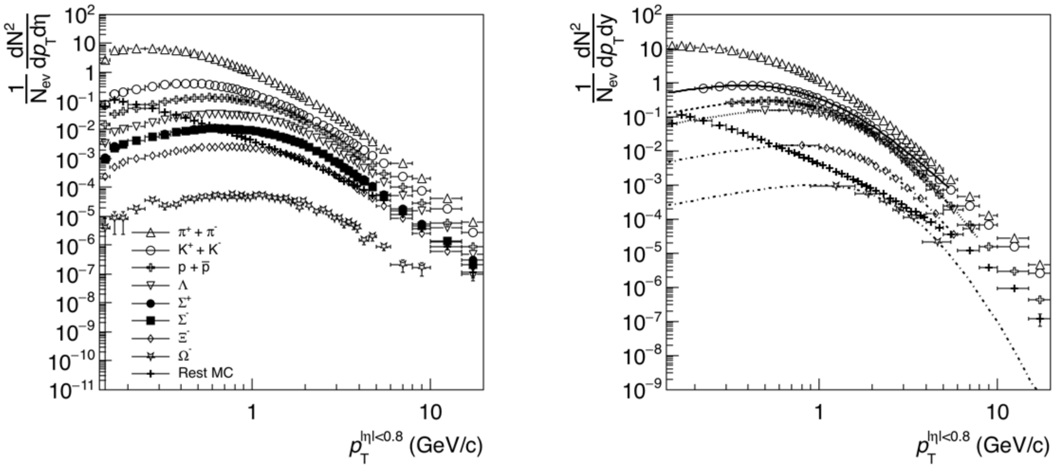

Figure 5.4: a) Invariant yield for different particle species from Monte Carlo PYTHIA 6 Perugia 2011, b) Levy-Tsallis fit for identified particle spectra from data to get the extrapolation for wide p_{T} binning.

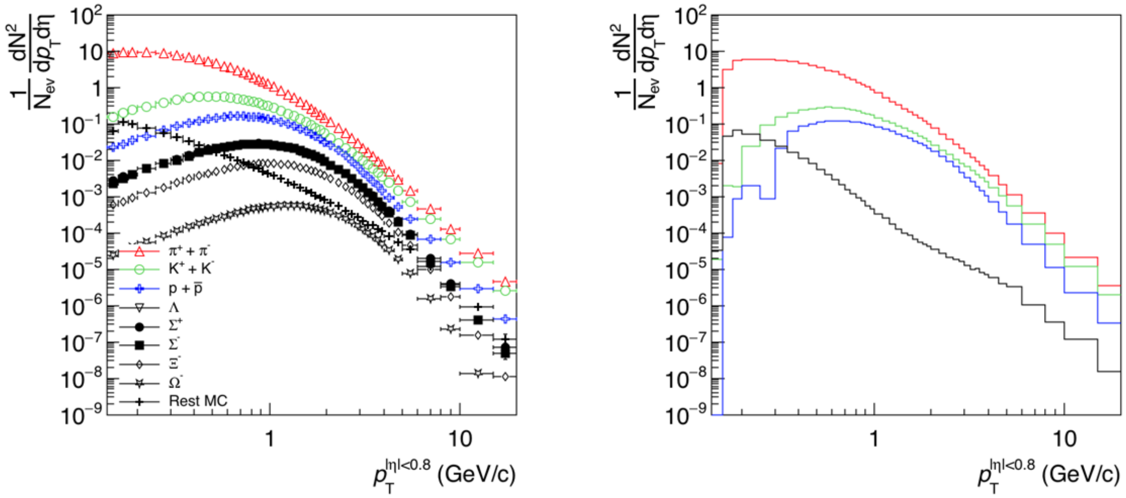

Figure 5.5: a) Invariant yield for different particle species from data extrapolation fit, b) Invariant yield for $\pi^+ + \pi^-$ (red), K$^+$+K$^-$ (green), p+$\bar{p}$ (blue) and rest (black) multiplied by the tracking efficiency (Fig. 5.3).

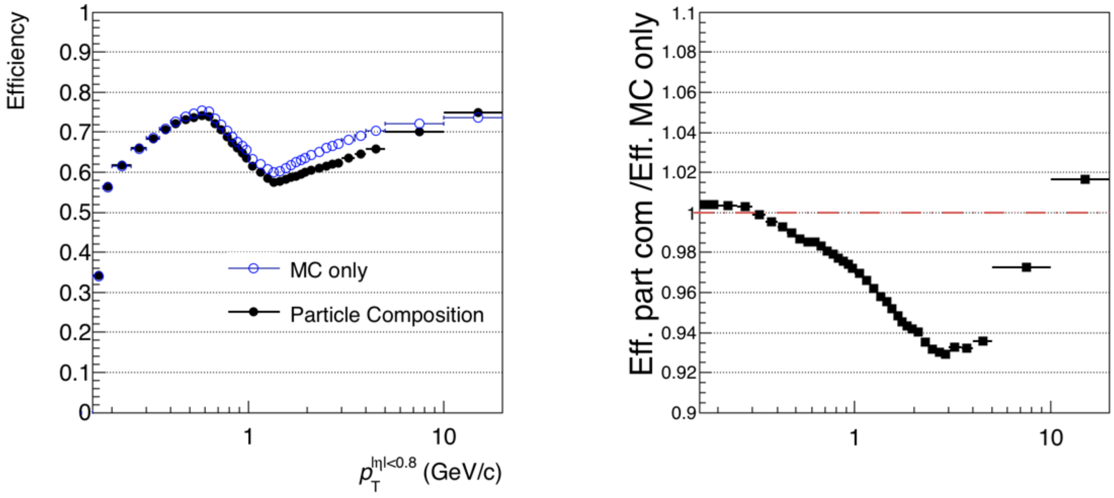

Figure 5.6: a) Efficiency from particle composition (black dots) and from Monte Carlo (blue circles) , b) fraction from both methods

For secondaries contamination a procedure from data was also done, for this we obtain the DCA$_{xy}$ distribution from data, and using MC Pythia 6 Perugia 2011 we get the DCA$_{xy}$ distribution for primaries, secondaries from weak decays and secondaries from material interaction (see Fig. 5.7), then using a multitemplate fit (see Fig. 5.8), which parametrize the DCA$_{xy}$ distribution from data as expresed in equation 5.2, then the factor of primaries particles can be extracted, as can be seen in Fig. 5.9.

$$DCA^{data}{}_{\mathrm{xy}}=\alpha\cdot DCA^{MC}_{\mathrm{XYsec-mat}}+\beta\cdot DCA^{MC}_{\mathrm{XYsec-weakdecay}}+\gamma\cdot DCA^{MC}_{\mathrm{XYprim}}$$

to

(5.3)

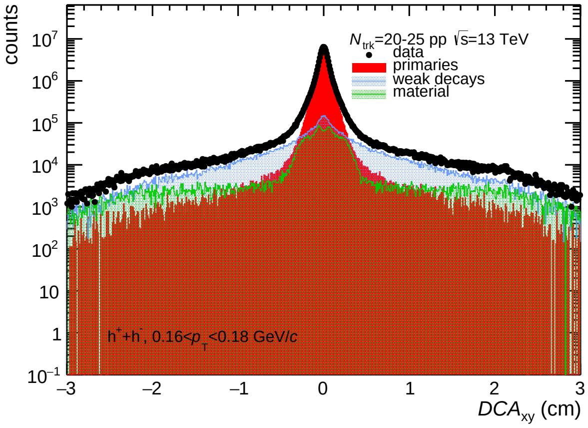

Figure 5.7: DCA distribution for events with $20 \leq N_{ch} \leq 25$ and $0.15 < p_{\rm T} < 0.18$ GeV/c from data and from MC (primaries and secondaries from material and weak decays).

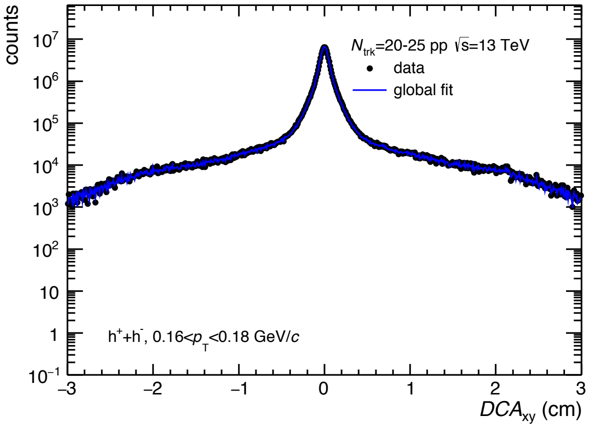

Figure 5.8: Multitemplate fit applied to data in order to extract primaries factor.

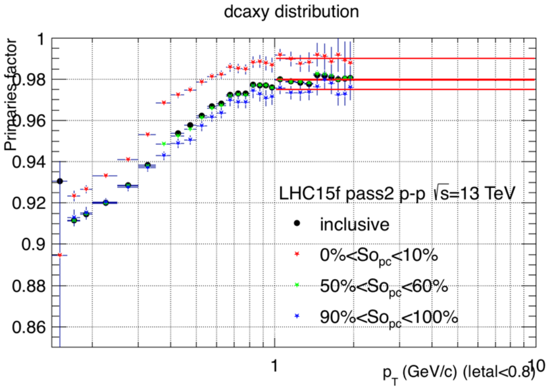

Figure 5.9: Primaries factor, we see a 2% multiplicity dependence same effect is observed for spherocity selection, this will be taken into account for systematics.

5.2.3 Multiplicity and spherocity corrections by weighting procedure

Once the $p_{\rm T}$ spectra are corrected for efficiency and contamination from secondaries, the correlation $\langle p_{\rm T} \rangle$ vs N_m reconstructed multiplicity is first corrected by spherocity as follows.

For a fixed bin of measured multiplicity ($N_{\rm m}$), the average $p_{\rm T}$ in the "corrected" spherocity interval i, $S_0^{\rm c,i}$, is obtained as follows:

$$\langle p_{\rm T}\rangle \left(N_{\rm m}, S_0^{{\rm c},i}\right) = \sum_{j=1}^{10} \langle p_{\rm T}\rangle \left(N_{\rm m}, S_0^{{\rm m},j}\right) \times R^{S_0,N_{\rm m}}(S_0^{{\rm m},j}, S_0^{{\rm t},i}) \tag{5.4}$$

Where, $\langle p_{\rm T}\rangle \left(N_{\rm m}, S_0^{{\rm m},j}\right)$, is the average $p_{\rm T}$ in the measured multiplicity bin $N_{\rm m}$ and measured spherocity bin j: $S_0^{{\rm m},j}$. $R^{S_0,N_{\rm m}}$ is the spherocity response matrix at $N_{\rm m}$. It is worth mentioning that the spherocity binning for the response matrices is defined by data, because we should remember that we cut on S_0 percentiles.

Once the mean $p_{\rm T}$ is corrected for spherocity selection, we used a similar procedure to correct for multiplicity. The multiplicity correction process uses the multiplicity response matrix R($N_{\rm t}$,$N_{\rm m}$), such that the mean transverse momentum ($\langle p_{\rm T}\rangle$) at "corrected" multiplicity $N_{\rm c}$ (bin i) is obtained by:

$$\langle p_{\rm T}\rangle(N_{\rm c}^i) = \sum_j \langle p_{\rm T}\rangle(N_{\rm m}^j) R(N_{\rm m}^j, N_{\rm t}^i) \tag{5.5}$$

where $N_{\rm m}^j$ is the measured multiplicity and $N_{\rm t}^i$ its the "true" (generated) multiplicity for the bins j and i, respectively. Clearly, $R(N_{\rm m}, N_{\rm t})$ is obtained from MC, whereas, $\langle p_{\rm T}\rangle(N_{\rm m})$ comes from the data. It is important to remember that at this stage, $\langle p_{\rm T}\rangle(N_{\rm m})$ has been already corrected for spherocity selection.

Multiplicity response matrix

The correlation between the reconstructed (measured) and generated (true) quantity is called detector response matrix. If we take multiplicity as the quantity, then we name it multiplicity response matrix. For the analysis we obtain the multiplicity response matrix from Monte Carlo simulations, in Fig. 5.10 we show the corresponding multiplicity response matrix for EPOS-LHC for all charged particles. As one can see in the response matrix, we do not have enough statistics, therefore, we extrapolated the behaviour. The procedure to extrapolate the detector response at high multiplicity was as follows. Taking the projection on the reconstructed bins for every true bin of the response matrix, the shape of this was fitted by a Gaussian function. Then for every Gaussian function we obtain the mean and the sigma from the fits, we plotted this as a function of the true multiplicity bins and we fitted to linear functions as can be seen in Fig. 5.11.

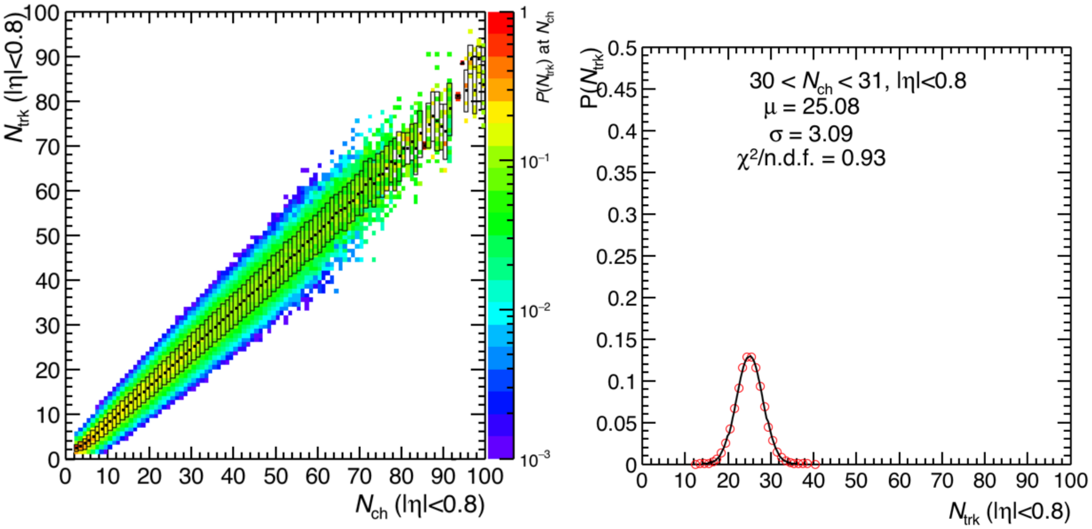

Figure 5.10: a) Multiplicity response matrix for all charged particles at 13 TeV for Epos-LHC, b) projection of the response matrix for a generated multiplicity bin fitted to a gaussian function.

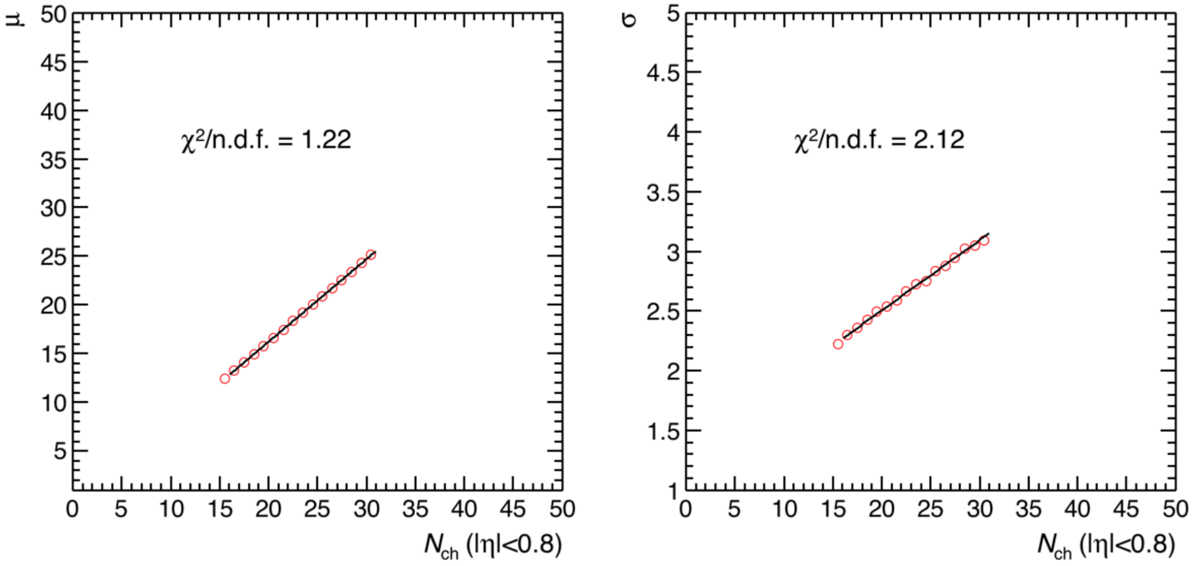

Figure 5.11: a) Mean vs true multiplicity, b) sigma vs true multiplicity fitted to a linear funtion.

With this fits to the mean and the sigma we can get the behaviour for high multiplicity and finally obtain the extrapolated response matrix as can be seen in Fig 5.12. For the multiplicity corrections, we use also the inclusive multiplicity response matrix, because the behaviour of the extrapolated one for jetty and isotropic are the same as for the inclusive.

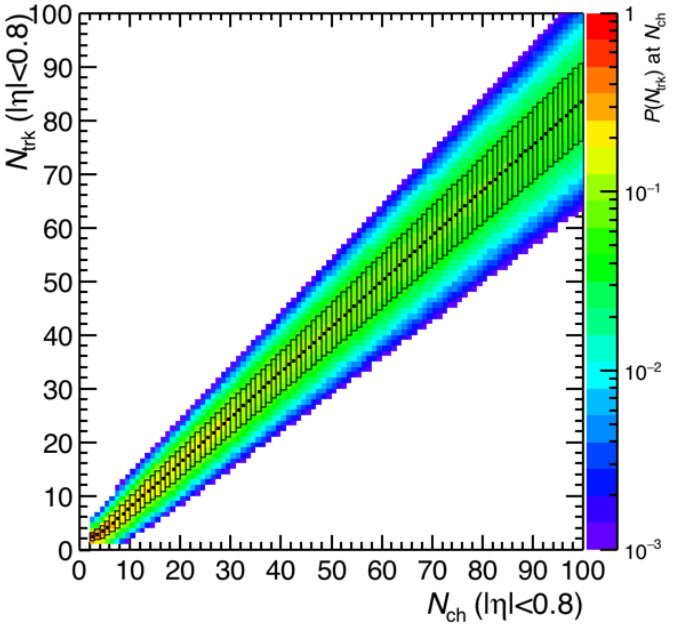

Figure 5.12: Extrapolated multiplicity response matrix for all charged particles generated with EPOS-LHC.

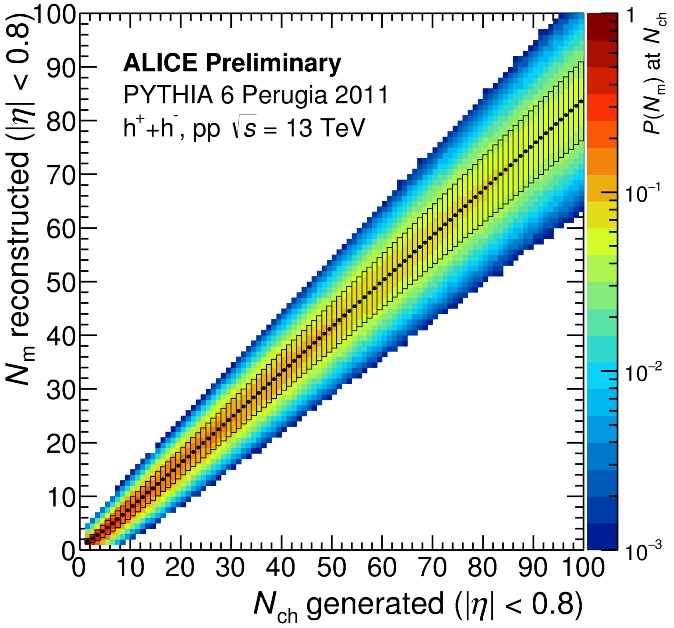

ALI-PREL-136722

Figure 5.13: Extrapolated multiplicity response matrix for all charged particles generated with PYTHIA 6 Perugia 2011 for 13 TeV.

Spherocity response matrix

In order to see the behaviour of the event spherocity generated vs reconstructed and to proceed with the spherocity correction, we get the spherocity response matrix for each multiplicity bin, using the binning from the spherocity percentile selection from data for each measured multiplicity class (see Fig. 5.14).

We can see that at low multiplicity the resolution is not good, at high multiplicity and specially for jetty events (low spherocity) the reconstruction its better.

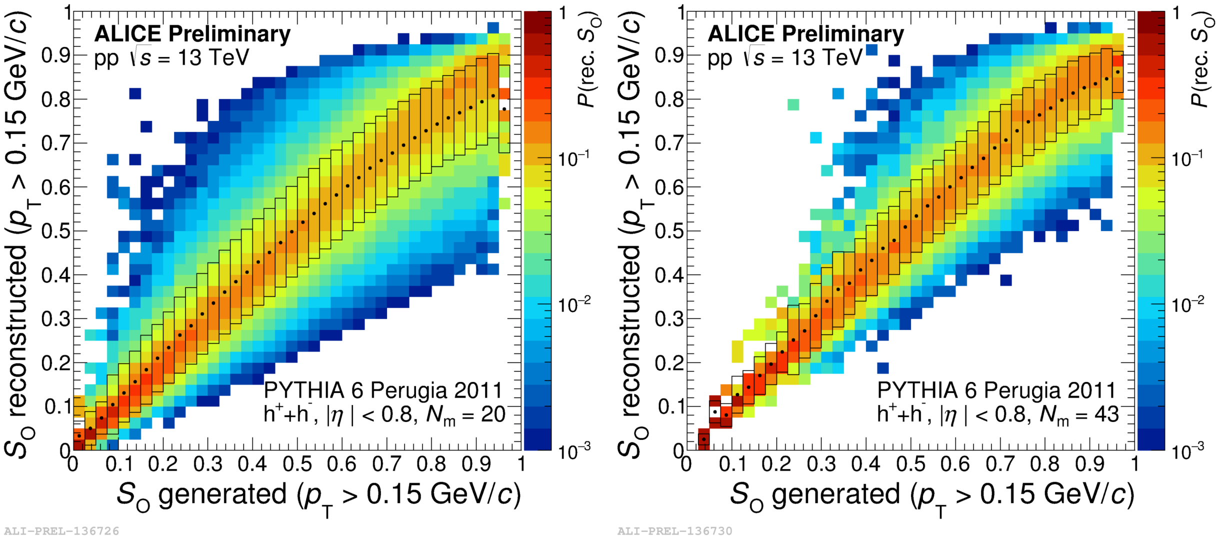

Figure 5.14: Spherocity response matrix for different multiplicity bins: a) N_n=20, b) N_m=43 taken from [32]

In order to correct the spectra for spherocity bins as specified in equation 5.4, we need for each true spherocity bins, the probability of the reconstucted spherocity bins, for all measured multiplicity. For high multiplicity we also apply the extrapolation taking the behaviour of the mid high multiplicity bins using a linear fit (black lines, We also have checked with another function, exponential one, and found a negligible effect section 5.4.3), were the behaviour its not affected by the statistical fluctuations, as can be seen in the next Fig. 5.15,5.16,5.17,5.18,5.19. We see that the greater spherocity correction is done for isotropic events, where the probability of having a reconstructed isotropic event ($90 - 100\%$ So percentil, red stars in Fig. 5.19 right, given a generated isotropic event is of the order of $40 - 50\%$ for most of the multiplicity bins, for jetty events (red full squares in Fig. 5.15 left, $0 - 10\%$ So percentil) the value is of the order of 70%.

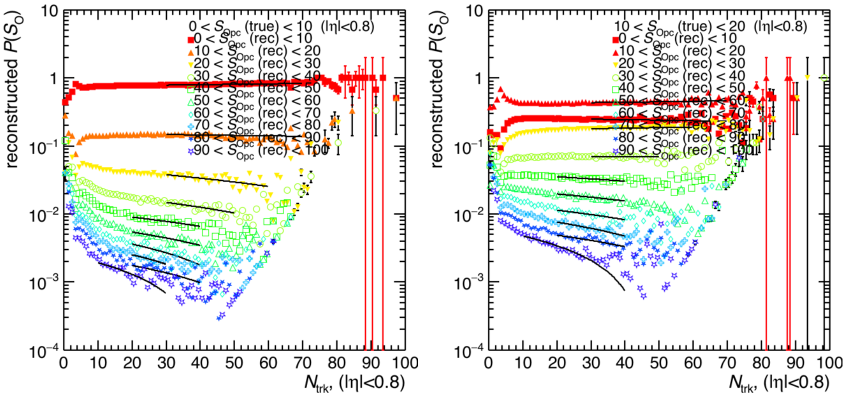

Figure 5.15: Probability of measured spherocity for left) $0-10\%$ S_{0perc}, right) $10-20\%$ S_{0perc}, using PYTHIA 6 Perugia 2011 for 13 TeV.

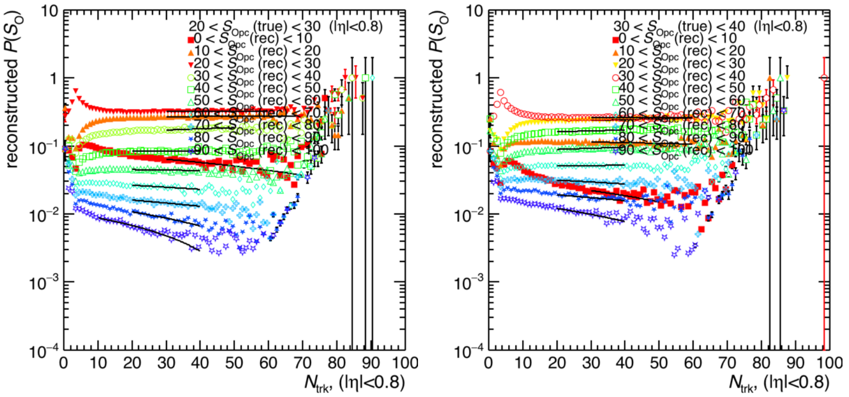

Figure 5.16: Probability of measured spherocity for left) $20-30\%$ S_{0perc}, right) $30-40\%$ S_{0perc}, using PYTHIA 6 Perugia 2011 for 13 TeV.

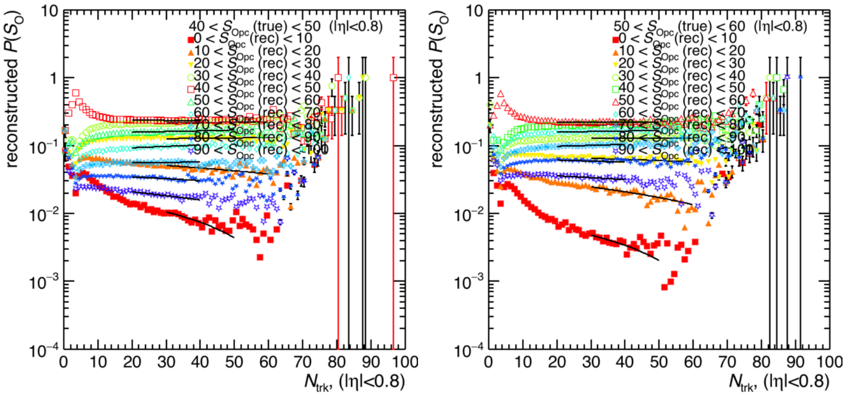

Figure 5.17: Probability of measured spherocity for left) $40-50\%$ S_{0perc}, right) $50-60\%$ S_{0perc}, using PYTHIA 6 Perugia 2011 for 13 TeV.

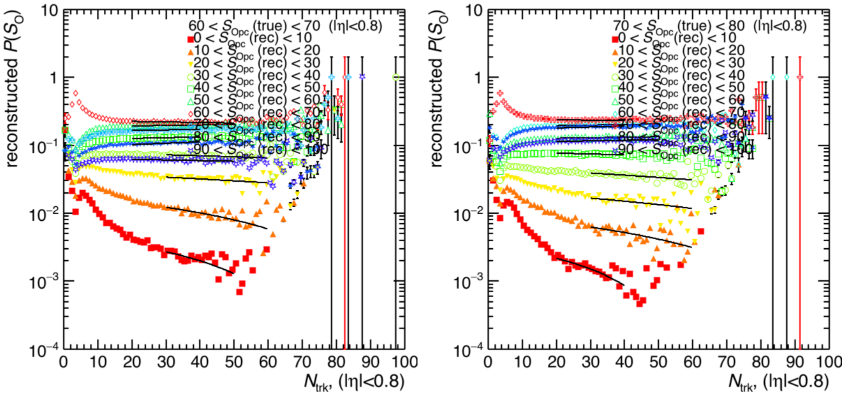

Figure 5.18: Probability of measured spherocity for left) 60−70% S_{0perc}, right) 70−80% S_{0perc}, using Pythia 6 Perugia 2011 for 13 TeV.

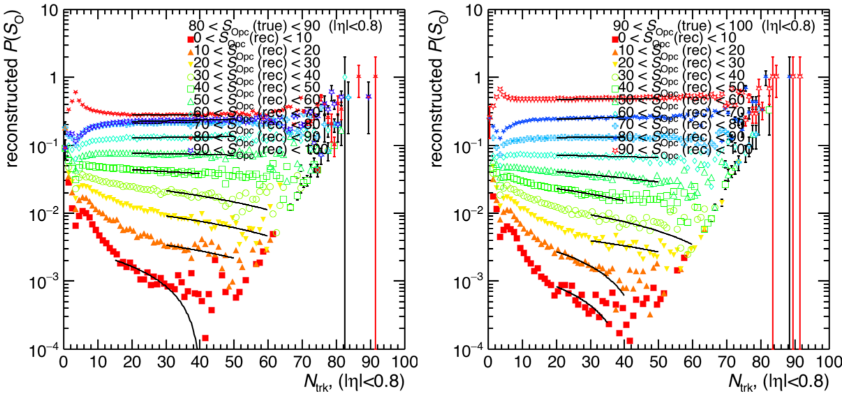

Figure 5.19: Probability of measured spherocity for left) 80 − 90% S_{0perc}, right) 90 − 100% S_{0perc}, using Pythia 6 Perugia 2011 for 13 TeV.

5.2.4 Closure test

To test the method of correction from spherocity and multiplicity, the closure test is done. This consist to use a reconstructed MC as data and correct it with the responses matriz from generated vs reconstructed MC, at the end one would like to recover the result from the generated MC. For this analysis we used the reconstructed Perugia2011 at 13 TeV as data and correct using the same MC, in order to compare with the result from the generated value. First it was done for the inclusive case, without spherocity selection (see Fig. 5.20). We see in the closure test for this sample that the uncertainty from the weighting procedure is within 2% at low and high multiplicity, as expected from the analysis done for mean transverse momentum for charged particles [36]. For the spherocity selection the closure test has been done (see Fig. 5.21), In this case we get a value 4% for jetty events and isotropic events.

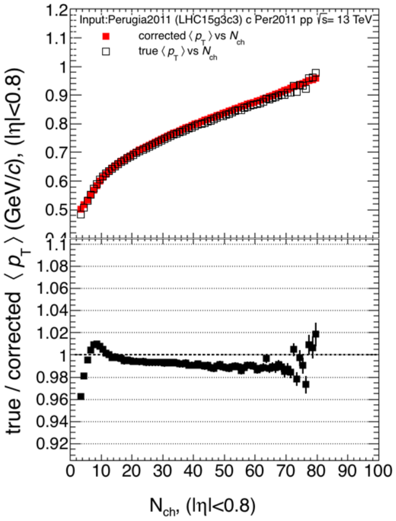

Figure 5.20: Closure test for 13 TeV, Pythia 6 Perugia 2011 corrected with the same MC for inclusive case.

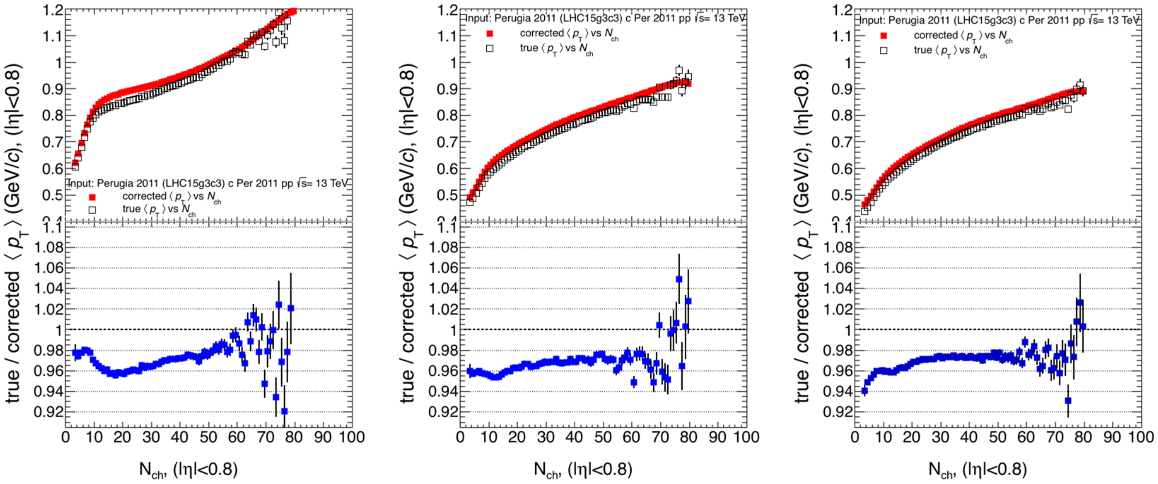

Figure 5.21: Closure test for 13 TeV, Pythia 6 Perugia 2011 corrected with Pythia 6 Perugia 2011 for spherocity selection: a) jetty $10-20\%$ S_{0perc}, b) intermediate $50-60\%$ S_{0perc} and c) isotropic $90-100\%$ S_{0perc}.

5.3 About spherocity selection

For the LHC15f pass2 data sample the following steps (including the ones done from MC) have been followed for the analysis:

- The spherocity selection was done in percentiles as described in the next subsection 5.3.1.

- The mean transverse momentum fully corrected including systematics has been also compared to MC models as Pythia 6, Pythia 8 and Epos-LHC (see subsection 6.0.1).

5.3.1 Spherocity percentile selection

For spherocity selection we get the spherocity for each multiplicity bins, and as described before in section 1.4.1, a percentile binning has to be taken in order to avoid the low number of events (high statistical fluctuations) for a specific shape. For the analysis the selection has been done with a multiplicity bin of 1. In order to give an idea of the evolution of spherocity behaviour for all the different multiplicities, we show in Fig. 5.22 and Fig. 5.23, the probability distribution of spherocity for some ranges of multiplicity using a different binning. Clearly it can be seen that in average the spherocity increase (goes from jetty to isotropic events) while multiplicity increases too.

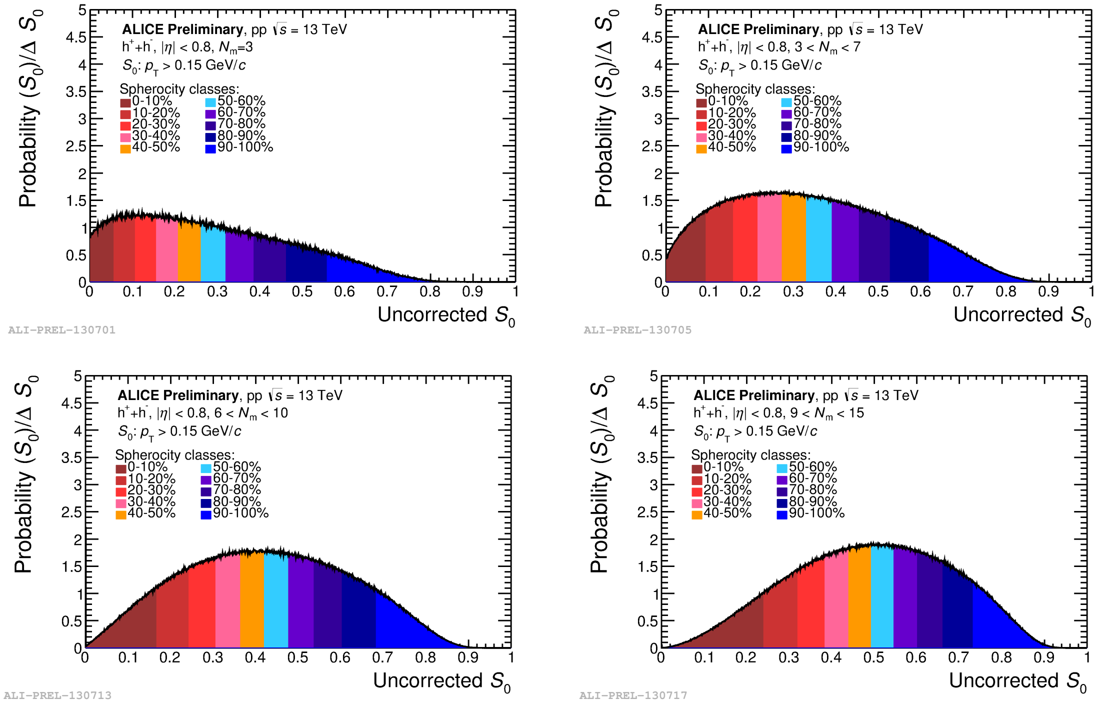

Figure 5.22: Spherocity probability evolution with multiplicity, for a) $N_{ch} = 3$, b) $3 < N_{ch} < 7$, c) $6 < N_{ch} < 10$, d) $9 < N_{ch} < 15$.

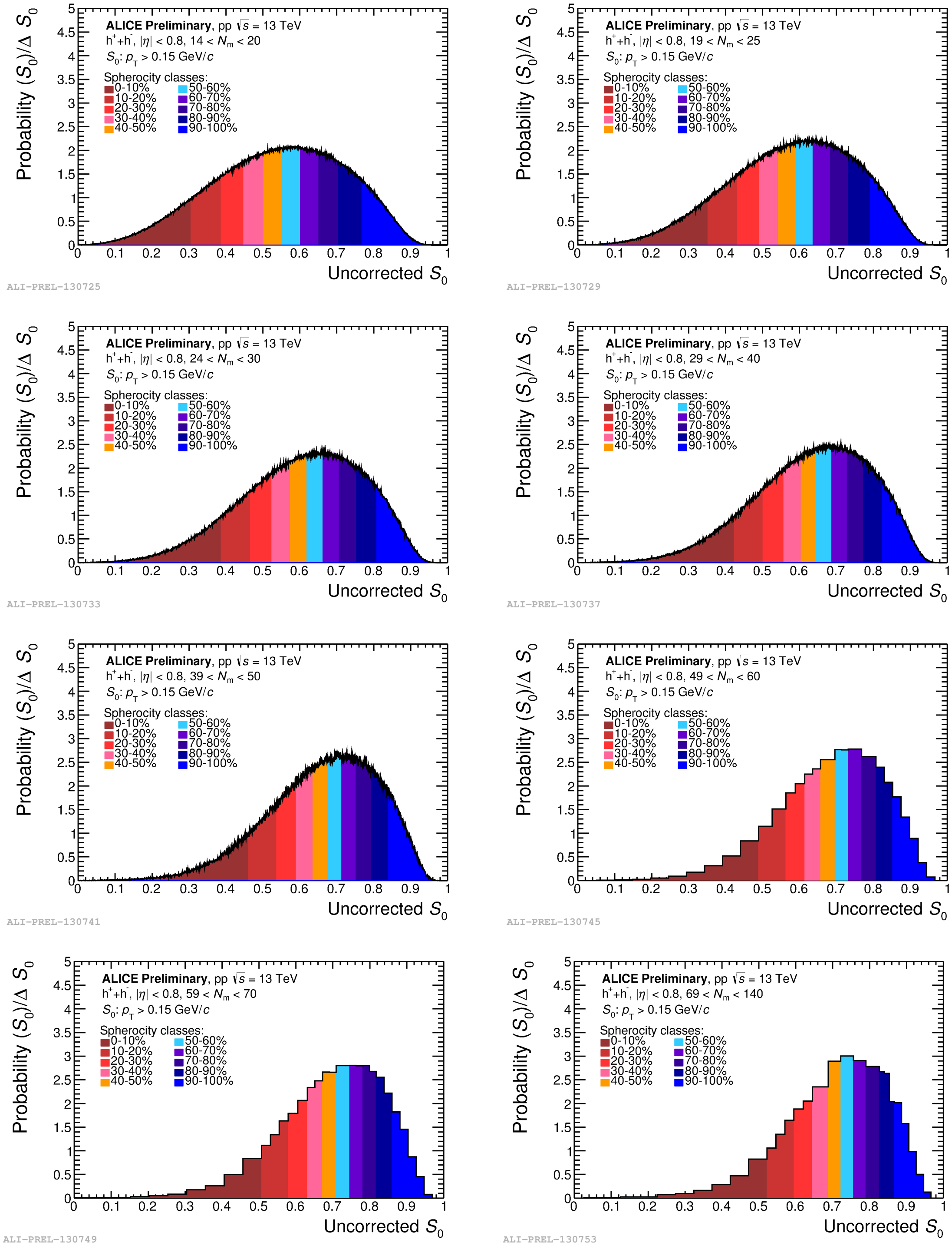

Figure 5.23: Spherocity probability evolution with multiplicity, for e) $14 < N_{ch} < 20$, f) $19 < N_{ch} < 25$, g) $24 < N_{ch} < 30$, h) $29 < N_{ch} < 40$, i) $39 < N_{ch} < 50$, j) $49 < N_{ch} < 60$, k) $59 < N_{ch} < 60$, l) $59 < N_{ch} < 70$ and m) $69 < N_{ch} < 140$.

5.3.2 Raw mean transverse momentum in spherocity percentiles

Following the spherocity selection the next step was to obtain the transverse momentum spectra in bins of measured multiplicity and measured spherocity, with this we get the measured mean transverse momentum vs measured multiplicity for the inclusive case (no spherocity selection) and for bins of spherocity percentile (see Fig. 5.24), we get a cross check comparing the inclusive case with the sum of the mean transverse momentum in spherocity bins weighted by the 10% of the sample

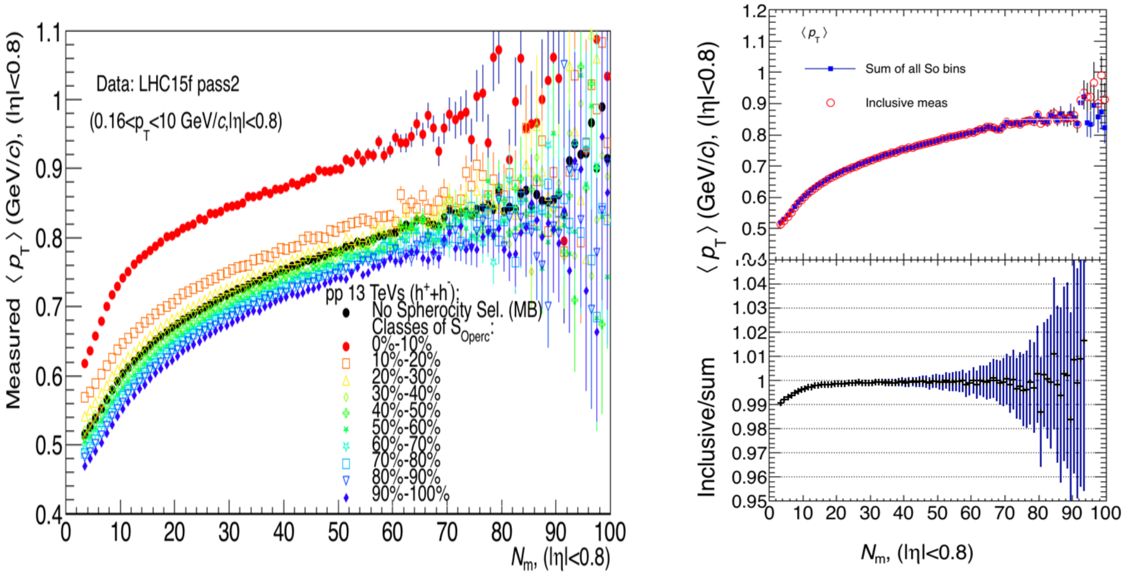

Figure 5.24: a) Mean transverse momentum for data LHC15f pass2 and b) cross check.

Modified Hagedorn and power law fits to spectra

In order to low the fluctuations at high multiplicity due to the statistics, a mean transverse momentum was obtained from the spectra combining two fit functions [38]:

- Modified Hagedorn for low transverse momentum ($p_T < 2$ GeV/c), its described by:

$$\frac{1}{2\pi}\frac{dN_{ch}}{d\eta dp_T} \approx \frac{p_T}{m_T}\left(1+\frac{p_T}{p_{T,0}}\right)^{-b} \tag{5.6}$$

- For high transverse momentum ($p_T > 2$ GeV/c) we use a power law, and its described by:

$$\frac{1}{2\pi}\frac{dN_{ch}}{d\eta dp_T} \approx p_T^{-n} \tag{5.7}$$

This was done for all the multiplicity bins and all the spherocity selections, some plots are shown in Fig. 5.25,5.26,5.27. Here we see that the greater fluctuations are for high multiplicity, and this effect is the one to correct.

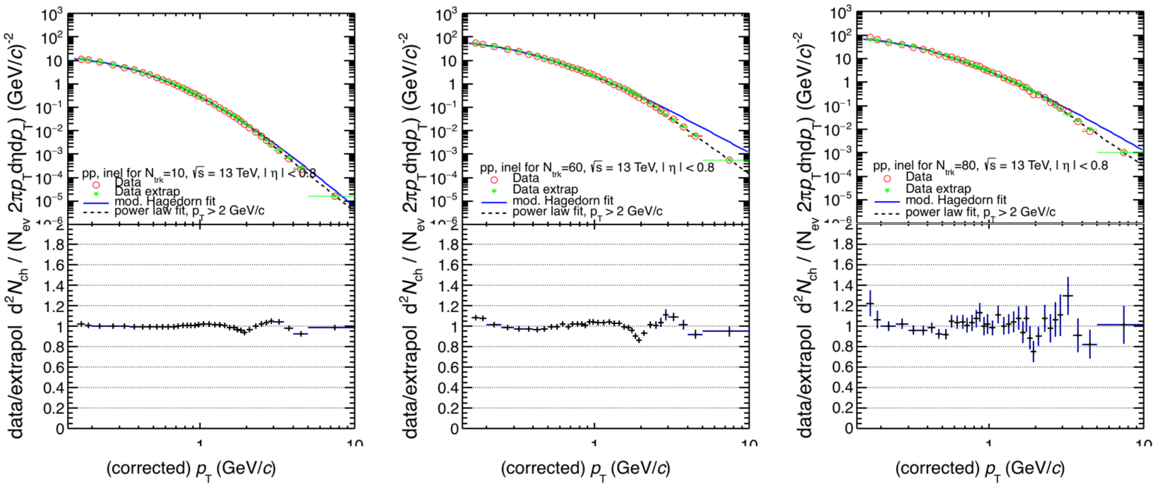

Figure 5.25: Fits for the spectra for inclusive case, a) N_m=10, b) N_m=60, c) N_m=80.

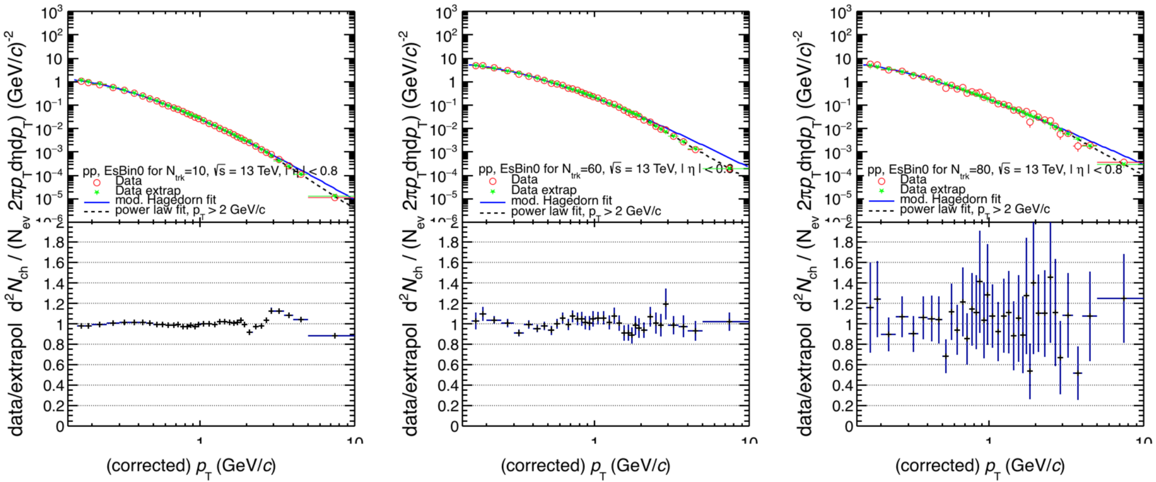

Figure 5.26: Fits for the spectra for jetty case, a) N_m=10, b) N_m=60, c) N_m=80.

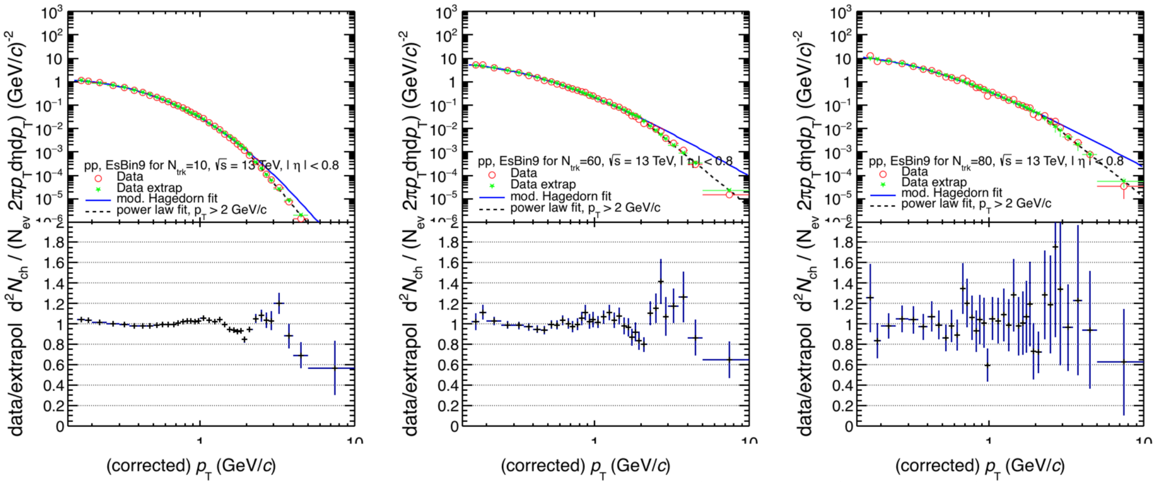

Figure 5.27: Fits for the spectra for isotropic case, a) N_m=10, b) N_m=60, c) N_m=80.

The corresponding comparison of the mean transverse momentum from data and the from the fit is shown in Fig. 5.28, the description is according for low multiplicity and within 0.05% for high multiplicity.

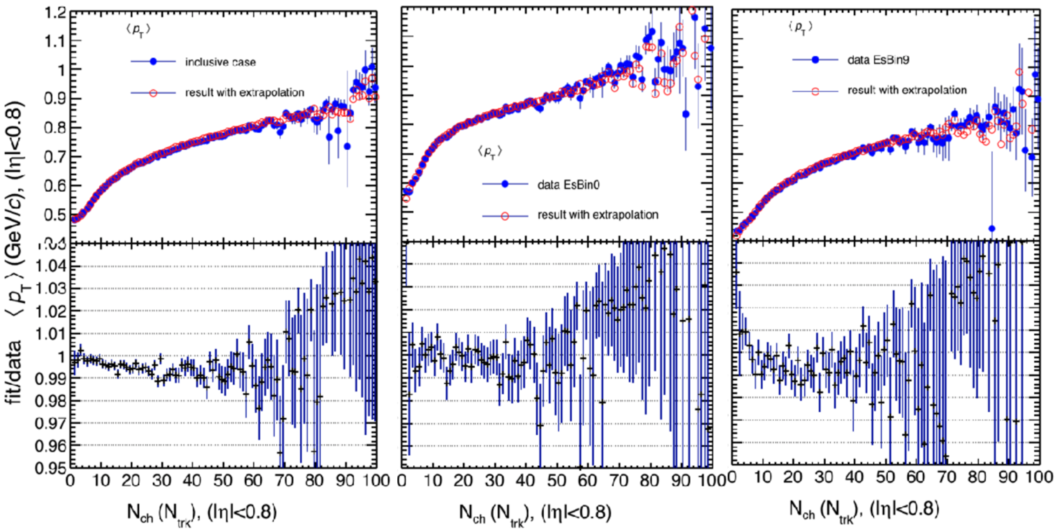

Figure 5.28: Comparison data with mean transverse momentum from the fit for a) inclusive, b) jetty and c) isotropic.

5.3.3 Fully corrected mean transverse momentum in spherocity percentiles

Then the fully corrected mean transverse momentum was obtained using the same procedure done for the closure test, but in this case we use data. The result obtained is shown in Fig. 5.29, here we see results for up to $N_{ch} = \mathit{100}$, due to the fact that for $N_{ch} > \mathit{80}$ the statistical error from data is greater than 10% (as seen in Fig. 5.24) the final results and comparison to models in next section will be given at this limit value. In order to study the behaviour of the mean p_{T} at high multiplicities, a first degree polynomial was fitted to the correlation within the multiplicity range 40-56. The ratios to fitted functions indicate a second rise of the mean p_{T} for jetty-like events, whereas, for isotropic events the mean p_{T} exhibits a saturation as seen in Fig. 5.30.

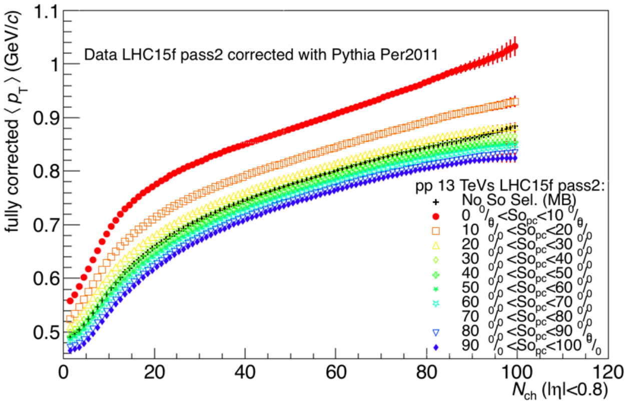

Figure 5.29: Fully corrected mean transverse momentum for inclusive case (black), and spherocity selection (colors).

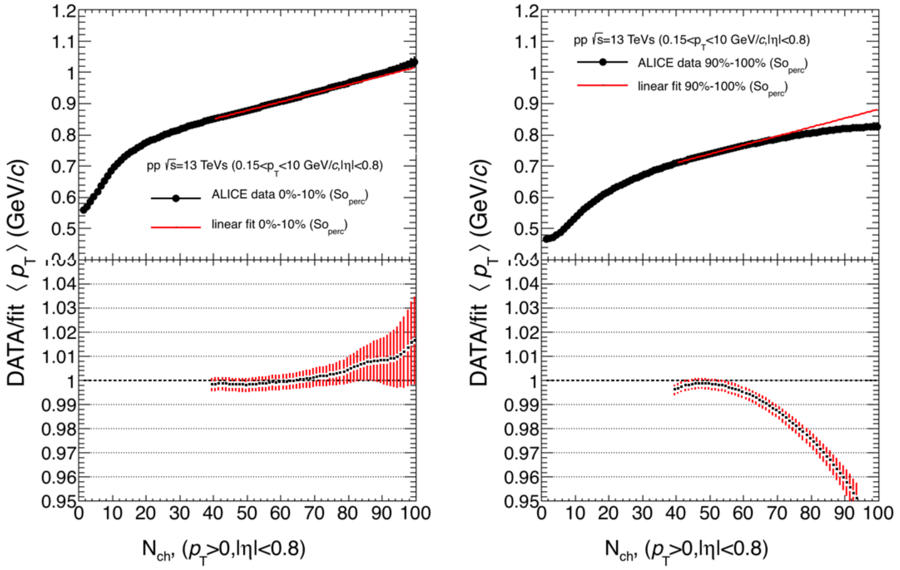

Figure 5.30: Mean transverse momentum comparing data with the fitted functions at high multiplcity for a) jetty and b) isotropic.

5.4 Systematic uncertainties

The systematics uncertainties for the mean transverse momentum vs multiplicity in each spherocity bin, were obtained from the next systematic sources: Method for correction (reweighting procedure), efficiency from particle composition, extrapolation of spherocity response, model dependence, track cuts for $\langle p_{\rm T} \rangle$, spherocity reconstruction and fits to spectra. The listed contributions to systematics are described in the next subsections.

5.4.1 Track cuts for $\langle p_{\rm T} \rangle$

To get the track cuts systematic uncertainties. we take it from the maximun deviation of the $\langle p_{\rm T} \rangle$ comparison from a varied value (lower or higher) to the nominal value. The variation for each track cuts are listed below in table 5.4.1, this was done for different spherocity bins.

Track cut	Nominal value	Lower value	Higher value
Min. num crossed rows	70	60	100
Min. ratio crossed rows over findable TPC cluster	0.8	0.7	0.9
Max χ^2 per cluster in TPC	4	3	5
Max χ^2 per cluster in ITS	36	25	49
SPD point	required	not required	not required
$\rm DCA_{xy}$	7σ	4σ	10σ
$\rm DCA_z$	2	1	5

Table 5.1: Track cuts variations for systematics calculation for mean transverse momentum.

The systematics uncertainty calculation was done taking the maximum deviation from the raw mean transverse momentum calculated with the nominal value and one calculated with the varied (lower or higher) value given in Fig. 5.31 for inclusive and for jetty and isotropic events in Fig. 5.32.

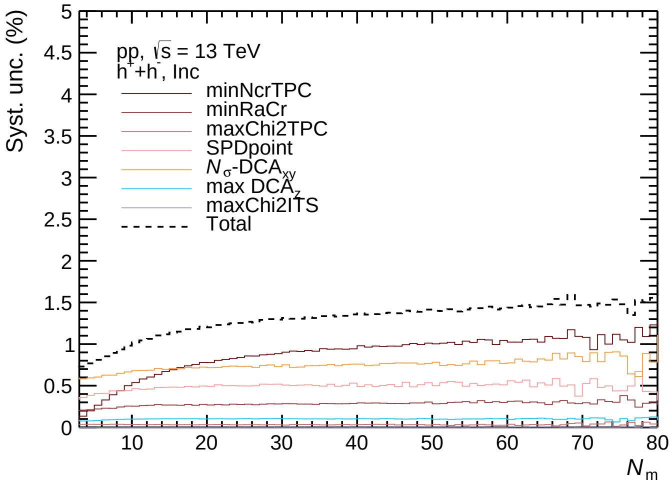

Figure 5.31: Systematics uncertainties from track cuts for inclusive case.

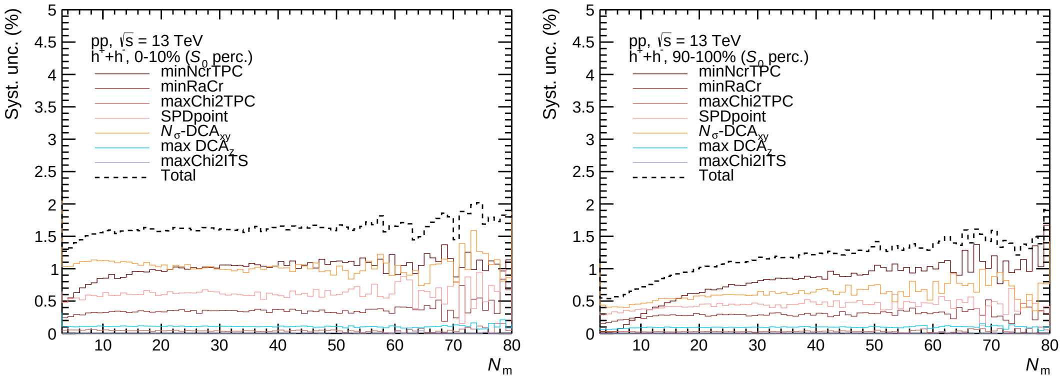

Figure 5.32: Systematics uncertainties from track cuts a) jetty and b) isotropic events.

5.4.2 Spherocity selection

The systematic uncertainty from the different track selection used to measure spherocity was calculated using the comparison from reference (Global tracks passed by TPC-only+TPC-refit track cuts) and the 2011 track cuts (see Fig. 5.39). As can be seen, from the comparison of spherocity from reference cuts and the 2011 track cuts, the variation is less than 1.5%, this value will be assigned as a systematic uncertainty.

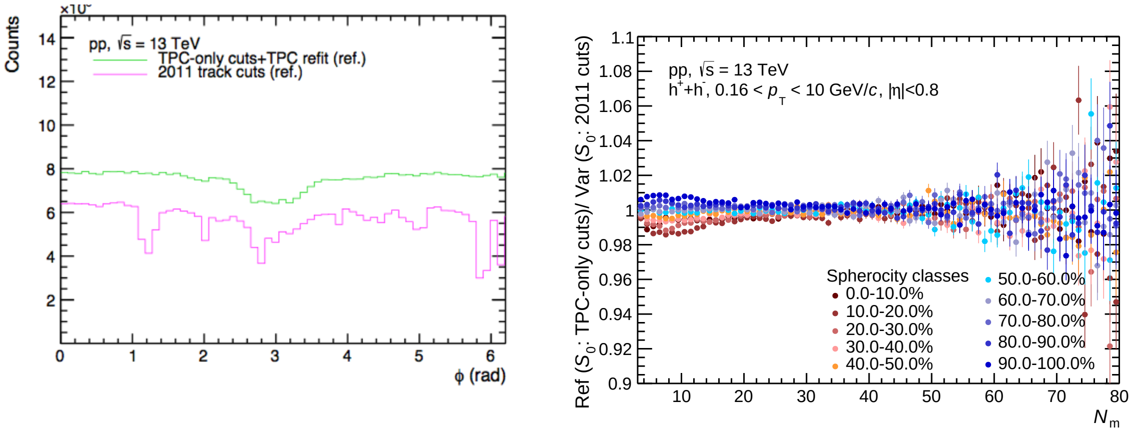

Figure 5.33: a) Azimuthal angular distribution (ϕ) for the two different tracks, b) ratio comparison for the variations on the track cuts.

5.4.3 Spherocity response matrix extrapolation

For the spherocity response matrix a extrapolation for high multiplicity was done using linear fit, but also an exponential fit could be done as can be seen in Fig. 5.34 The comparison in the mean transverse momentum for different spherocity bins is done, and this will be used as a systematic uncertainty, the effect is of the order of 1% as can be seen in Fig. 5.38, the systematics for all spherocity classes are described in Fig. 5.39 .

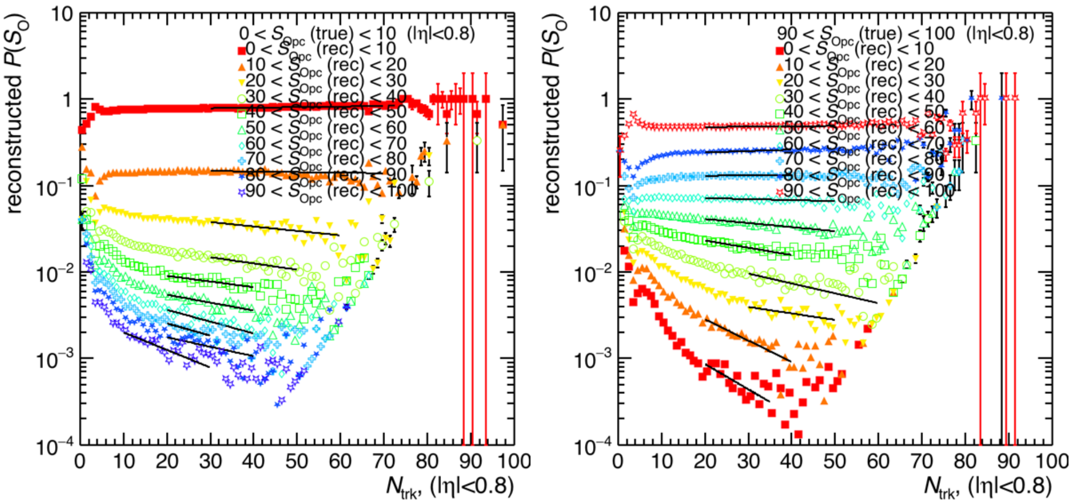

Figure 5.34: Proyections of the spherocity response matrix for different multiplicity bins, the lines in black are exponential fits, this are shown for generated a) jetty and b) isotropic.

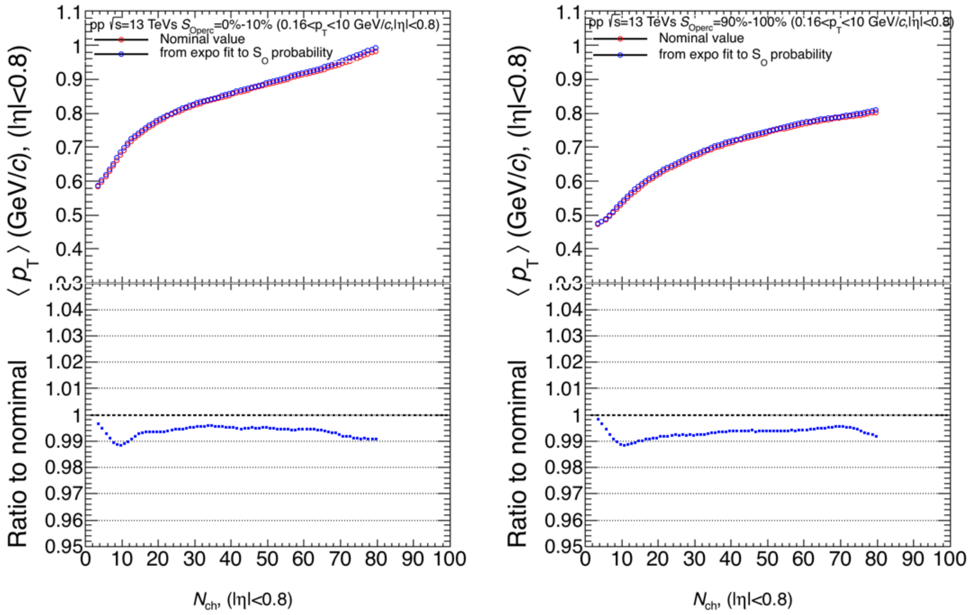

Figure 5.35: Comparison of the fully corrected mean transverse momentum using linear fit and exponential fit for the extrapolation on the proyection of the spherocity response.

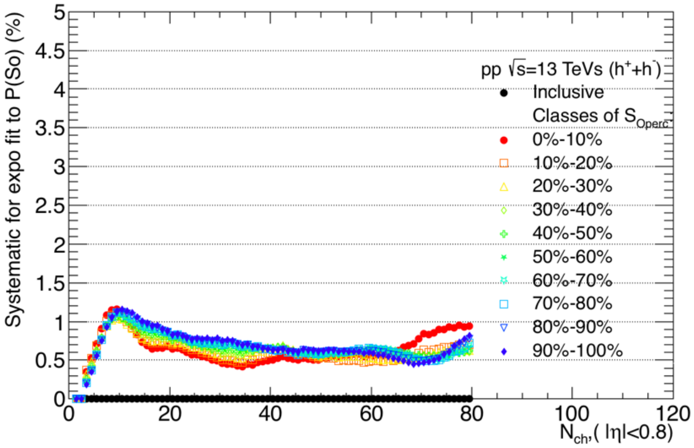

Figure 5.36: Systematics associated with the fit at high multiplicity in spherocity probability.

5.4.4 Multiplicity dependence on efficiency correction

For the efficiency correction was done with MB result, the multiplicity dependence comparison with respect the MB case according with [204] can be seen in Fig. 5.37 a), this varies from 1% ($p_{\mathrm{T}} < 1.5$ GeV/c) up to 3.5% ($p_{\mathrm{T}} > 1.5$ GeV/c). We varied the efficiency within this range and study the effect on the fully corrected $\langle p_{\mathrm{T}} \rangle$ vs N_{ch}, the systematic concerning to this can be seen in Fig. 5.37 b).

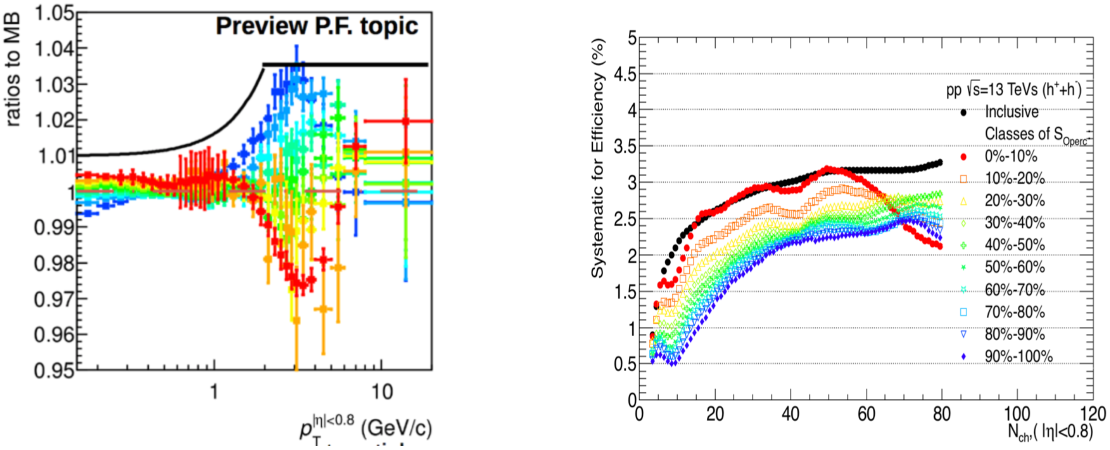

Figure 5.37: a) Efficiency comparison between different multiplicity bins to MB result [204], b) systematic associated with the multiplicity dependence of the efficiency.

5.4.5 Model correction dependence

For the correction procedure (multiplicity and spherocity corrections from response matrix) we have used data from simulations, depending on which MC model we use the correction could be a little different, a comparison between $\langle p_{\mathrm{T}} \rangle$ corrected with Pythia 6 and Epos-LHC corrections are shown in Fig. 5.38. The difference between the results is assigned as systematic uncertainty as shown in Fig. 5.39.

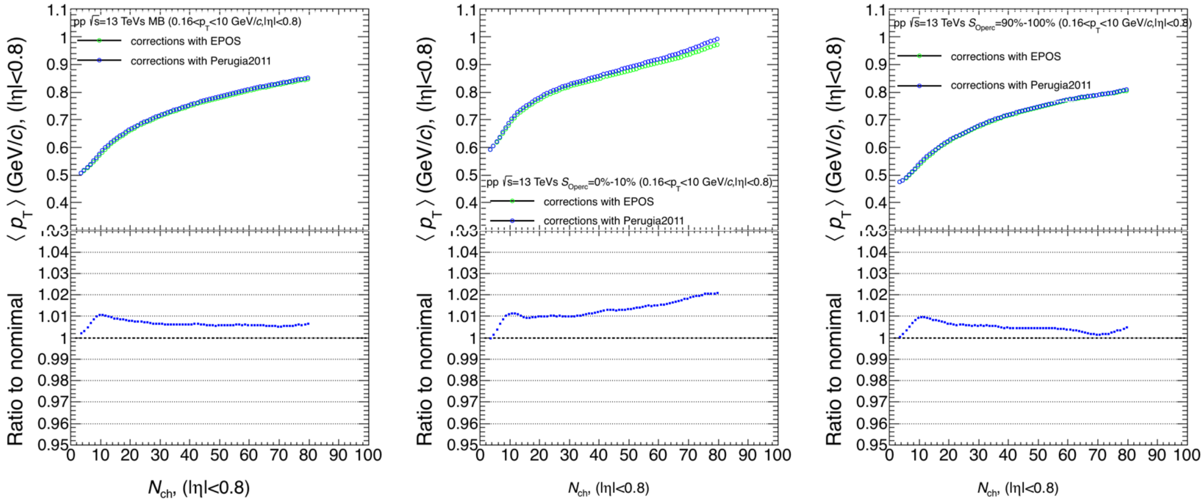

Figure 5.38: Comparison of the fully corrected mean transverse momentum corrected with Pythia 6 and Epos-LHC, for a) inclusive, b) jetty and c) isotropic events.

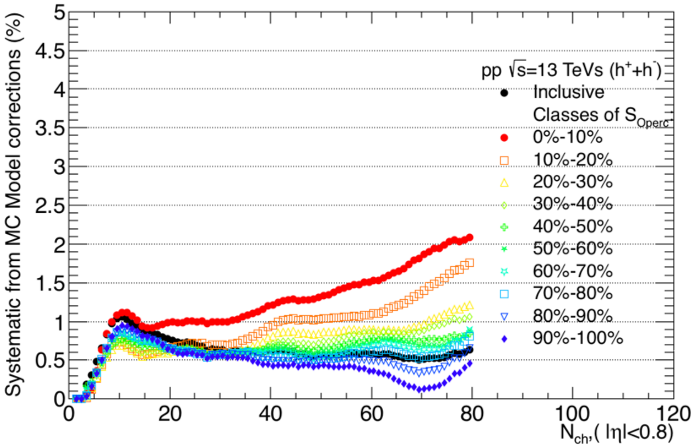

Figure 5.39: Systematics uncertainties associated with the MC models used for correction.

5.4.6 Method for correction procedure (non-closure)

From the closure test developed using Pythia 6 Perugia 2011 we take into account this non-closure as a systematic uncertainty, it has been seen that for almost all bins the closure test is withing the 4% except for the second spherocity bin (S_{0perc} class 10-20%), where due to the contamination of jetty events in the spherocity correction (see Fig. 5.15 right) it's a little higher. The systematic uncertainty can be seen in Fig. 5.40.

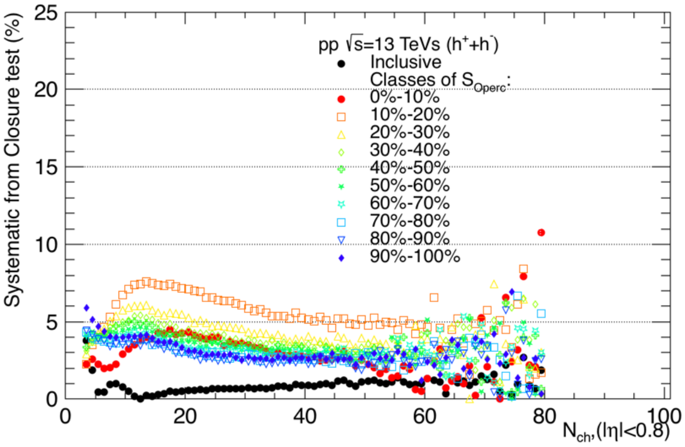

Figure 5.40: Systematics associated with the non-closure of the closure test using Pythia 6 Perugia 2011.

5.4.7 Secondaries contamination from DCA fit

A variation on the DCA_{xy} fit has been considered, varing the fit from the interval (-3,3) cm to the interval fit (-1,1) in order to see how the secondaries contamination is affected, the variation from the fit has been seen from $1-2\%$ for low p_{T} as shown in Fig. 5.41, but the effect in the primaries factor seems to be negligible.

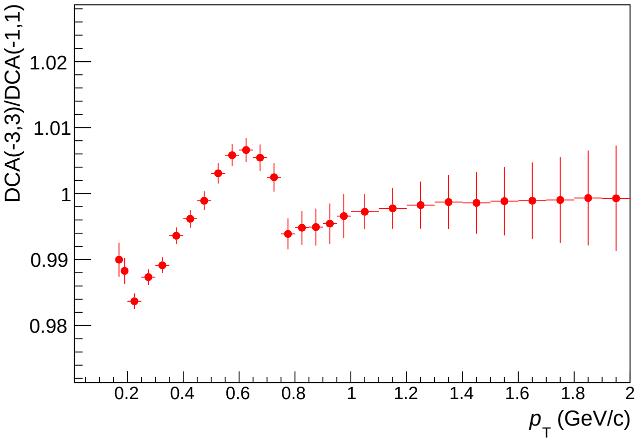

Figure 5.41: a) Comparison from different fit ranges to DCA

5.4.8 Total systematics uncertainties

From the systematics sources listed above, each contribution and the total systematic uncertainties are shown in Fig. 5.425.435.44. The greater systematic uncertainty for inclusive case comes from the multiplicity dependence on efficiency correction, for the case when spherocity selection is done, the main source of systematic uncertainty comes from the method for correction procedure (or the non-closure) and the second source is again the multiplicity dependence on efficiency correction.

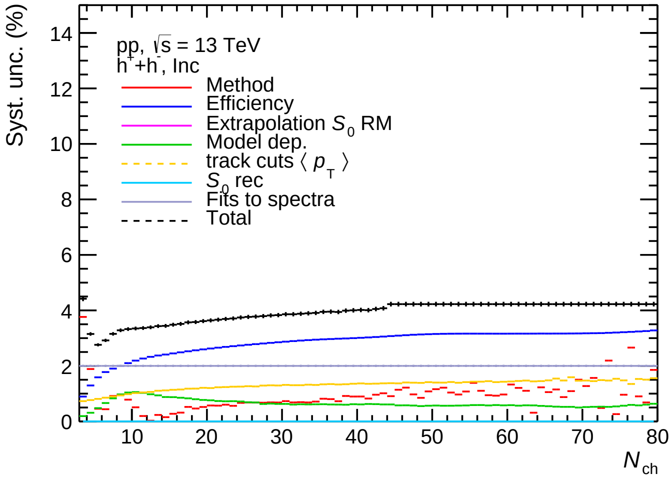

Figure 5.42: Summary of the systematics uncertainties for inclusive case.

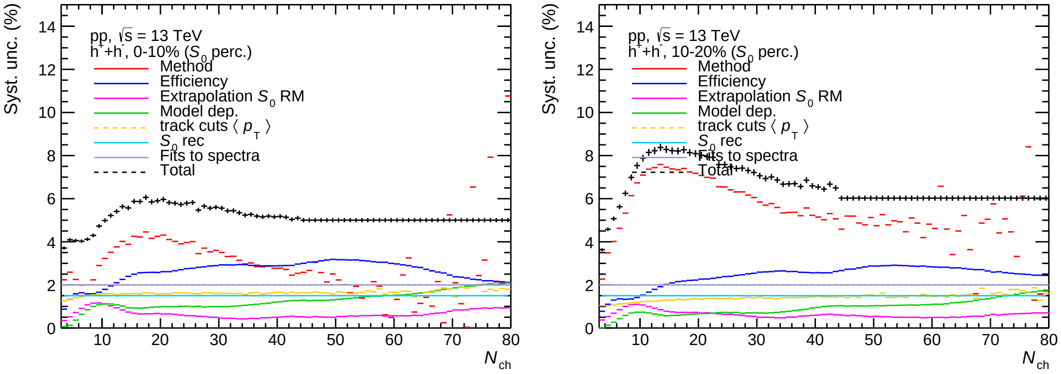

Figure 5.43: Summary of the systematics uncertainties for a) $0-10\%$ S_{0perc}, b) $10-20\%$ S_{0perc},

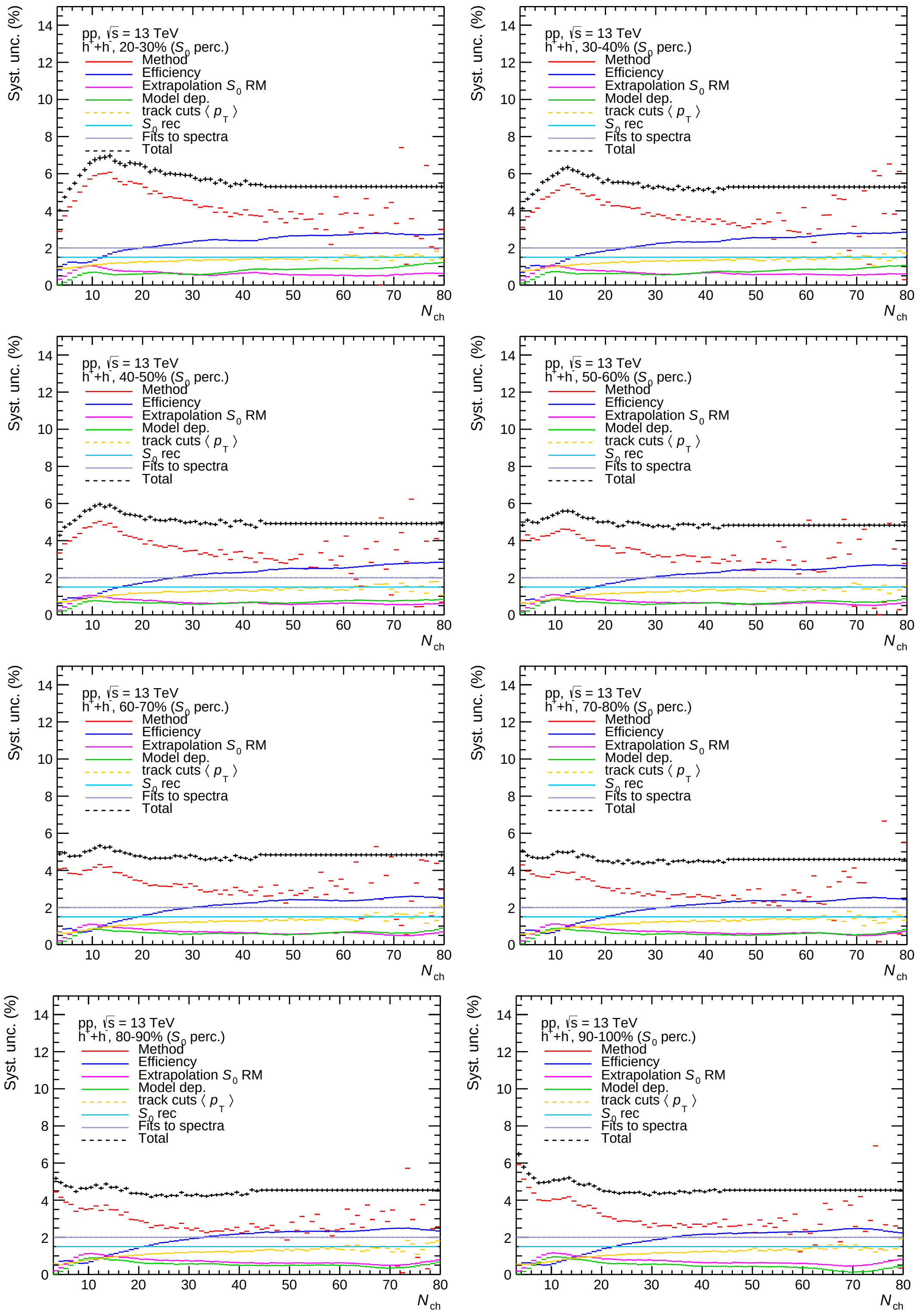

Figure 5.44: Summary of the systematics uncertainties for: c) $20-30\%$ S_{0perc}, d) $30-40\%$ S_{0perc}, e) $40-50\%$ S_{0perc}. f) $50-60\%$ S_{0perc}, g) $60-70\%$ S_{0perc}, h) $70-80\%$ S_{0perc}, i) $80-90\%$ S_{0perc}, j) $90-100\%$ S_{0perc}.

Chapter 6

Results and discussion

> Every act of seeing leads to consideration, consideration to reflection, reflection to combination, and thus it may be said that in every attentive look on nature we already theorise.
>
> (Johann Wolfgang von Goethe)

The observable reported in this thesis is the average transverse momentum as a function of the charged particle multiplicity. This correlation carries information about the underlying particle production mechanism. This has been studied by many experiments at hadron colliders in pp($\bar{\mathrm{p}}$) covering collision energies from $\sqrt{s} = 31\,\mathrm{GeV}$ up to $7\,\mathrm{TeV}$. All experiments observed an increase of $\langle p_{\mathrm{T}} \rangle$ in the central rapidity region, a feature which could be reproduced in the PYTHIA event generator only if a mechanism of hadronization including color reconnection is considered. Although a good description of TEVATRON data was achieved within the PYTHIA 8 model, which also described the early LHC data, full consistency of the data description within models is yet to be achieved. Particularly, ALICE has reported the $\langle p_{\mathrm{T}} \rangle$ as a function of N_{ch} for pp collisions at $\sqrt{s} = 0.9$, 2.76 and $7\,\mathrm{TeV}$. Both two quantities were measured in a very narrow pseudo-rapidity interval, $|\eta| < 0.3$, and for the average p_{T}, only charged particles with transverse momentum between 0.15 and $10\,\mathrm{GeV}/c$ were considered. In pp collisions at $\sqrt{s} = 7\,\mathrm{TeV}$ a strong increase $\langle p_{\mathrm{T}} \rangle$ with N_{ch} is observed for $N_{\mathrm{ch}} > 20$, which is much stronger than that measured in p-Pb collisions. Moreover, the stepper rise than that in p-Pb collisions seems to be center-of-mass energy independent.

Coming back to the discussion of the results for pp collisions at $\sqrt{s} = 7\,\mathrm{TeV}$, it seems that at low multiplicities ($N_{\mathrm{ch}} < 10$) the slope of the $\langle p_T \rangle$ increase is higher than that for "intermediate" multiplicities ($10 < N_{\mathrm{ch}} < 25$). When the multiplicities are very high, $\mathrm{d}N_{\mathrm{ch}}/\mathrm{d}\eta \sim 50$, a second rise of the average p_{T} is appreciated. This could be an indication of either the multiplicity bias towards hard events and/or genuine radial flow effects. As discussed earlier, the spherocity dependent studies can help to unveil whether the nature of this phenomenon is driven by hard or soft physics. The goal of this section is to discuss the first measurement of the event shape dependence of the average transverse momentum as a function of the event multiplicity in pp collisions at $\sqrt{s} = 13\,\mathrm{TeV}$. It is worth noting that the kinematic cuts used here differ from those implemented in the ALICE publication, however, the physics discussion should be the same.

6.0.1 Data and models comparison

The results for the average transverse momentum as a function of the event multiplicity for pp collisions at $\sqrt{s} = 13\,\text{TeV}$ are shown in Fig. 6.1. Spherocity integrated results (0-100%) exhibit similar features to those observed at lower energies, i.e. the changes in the slope in the low, intermediate and high multiplicity regions. It is wroth mentioning that the spherocity integrated class (0-100%) is essentially equal to MB, the only difference between them is observed at low multiplicity and it amounts to 2%. This is expected, since for relatively high multiplicities ($N_{\text{ch}} > 10$) the effect of the event selection based on track multiplicity (more than two particles with transverse momentum above $0.15\,\text{GeV}/c$) becomes negligible. Hereafter, the spherocity integrated event class will be referred as minimum bias.

The analysis as a function of transverse spherocity reveals interesting features. On one hand, for isotropic events the average p_{T} stays systematically below that for MB in the full multiplicity range; on the other hand it is higher for jetty-like events than for MB. Moreover, the functional form of the correlation also exhibits a notorious change. For example, the transition between low and intermediate multiplicities at $N_{\text{ch}} = 15$ shows a more aggressive change in the slope in jetty-like events than that seen in MB. The transition is smother for isotropic events. On the other hand for high multiplicity events, a second rise of the mean p_{T} is observed for jetty-like events. According with a study using PYTHIA 8.212 simulations, where $60\,\text{GeV}/c$ jets were included, N_{ch} around 15 (within $|\eta| < 0.8$) is exactly in the region where the fraction of number of leading jets inside and outside $|\eta| < 0.8$ changes. For example, for the spherocity integrated case, mid-pseudorapidity multiplicities (< 15) are achieved because for those events the most energetic jet in the event is outside the region where the multiplicity is determined. For higher multiplicities, the leading jets concentrate in the pseudorapidity region where the multiplicity is calculated. When one performs an event shape analysis using such a sample, for isotropic events the jets stays always outside the pseudorapidity region where multiplicity and event shape are both determined. For high multiplicity jetty-like events, all the leading jets lie within the pseudorapidity interval used to calculate spherocity and multiplicity, therefore, the mid-rapidity hadrons originated from string boosted due to jets could contribute to the second rise observed in high multiplicity events. Since PYTHIA 8.212 tune Monash 2013 reproduces rather well the LHC data, the observed changes in data could be a consequence of the biases introduced when one impose a spherocity selection on top of the multiplicity one.

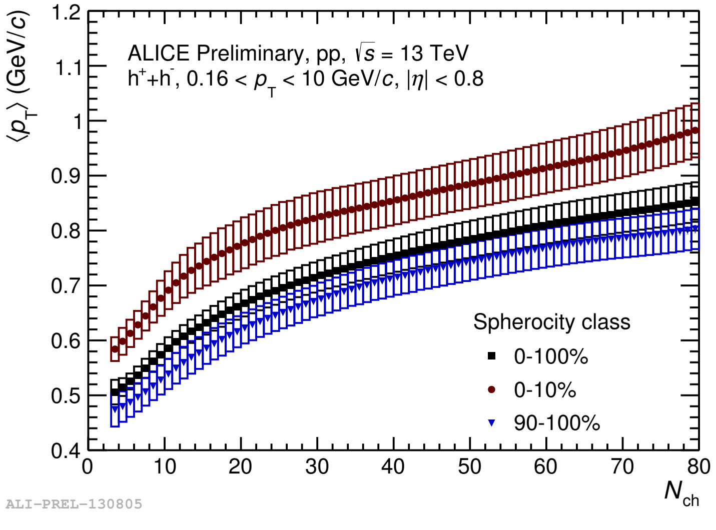

Figure 6.1: Mean transverse momentum as a function of the event multiplicity in pp collisions at $\sqrt{s} = 13\,\text{TeV}$. Results for the spherocity integrated case (0-100%) are shown along the results for the most jetty (0-10%) and most isotropic (90-100%) events. Statistical and systematic uncertainties are displayed as error bars and boxes around the data points, respectively.

Figure 6.2 shows a comparison between data and MC event generators for MB events. PYTHIA 6 and 8 tunes Perugia 2011 and Monash 2013, respectively; as well as EPOS LHC simulations are confronted with data. It is worth mentioning that for PYTHIA to reproduce the rise of the average p_{T} with increasing multiplicity, color reconnection had to be incorporated in the simulations. The model allows the interaction among partons before the hadonization. On one hand, within uncertainties, PYTHIA 8 and EPOS LHC describe the correlation over the full multiplicity interval; on the other hand, a tension between PYTHIA 6 and data is appreciated for $N_{\mathrm{ch}} > 20$. In order to investigate what is causing the discrepancy, figure D.1 shows the correlation for the most jetty (0-10%) and most isotropic (90-100%) events. For isotropic events the three models describe well the correlation, even PYTHIA 6 reduces the size of the discrepancy. Adversely, for for jetty events both PYTHIA 6 and 8 exhibit a larger disagreement with the data. From previous ALICE and CMS studies we know that the production of jets in high pp collisions is smaller in data than that obtained from the MC event generators. If this is the case, the the low momentum partons color connected with higher momentum ones (jets) would produce an overall increase of the hadron transverse momentum. This would affect more the jet enriched samples, which is achieved by requiring low spherocity values. The incorporation of these new observables in the MC tuning could be a bit challenging because, on one hand, the color reconnection has to be reduced to describe the low S_0-data, on the other hand, the variation should be not too large because the good description of the isotropic events could be affected. The evolution of the correlation with spherocity can be found in the Appendix B

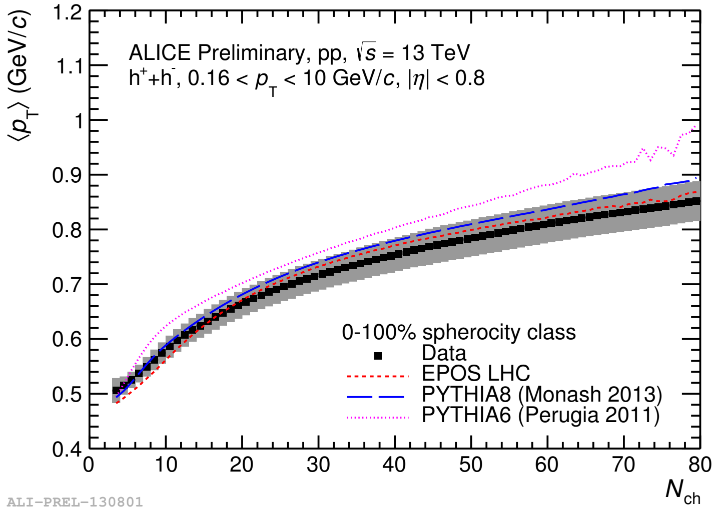

Figure 6.2: Mean transverse momentum comparing data vs MC for inclusive case.

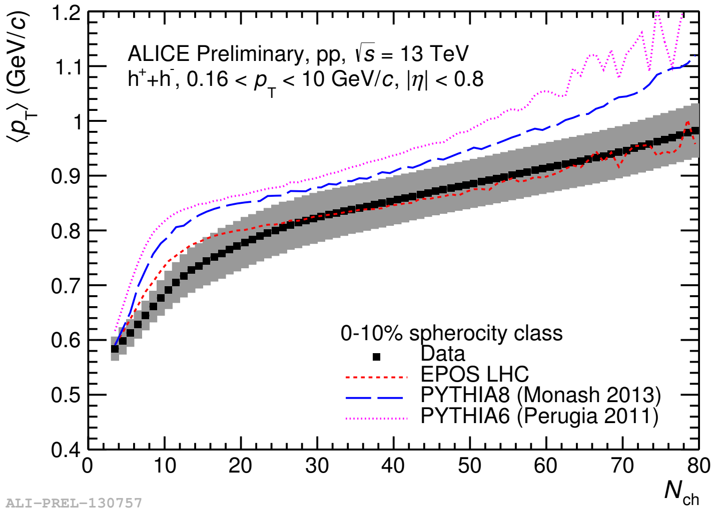

Figure 6.3: Mean transverse momentum comparing data vs MC for spherocity percentile classes $0 - 10\%$.

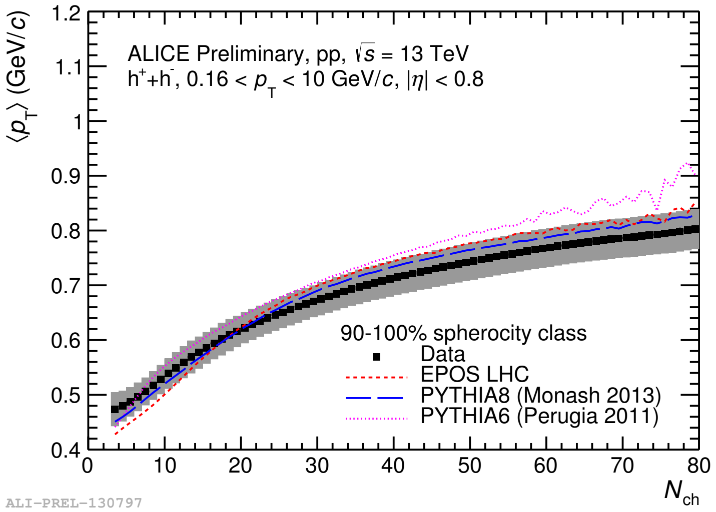

Figure 6.4: Mean transverse momentum comparing data vs MC for spherocity percentile classes $90 - 100\%$.

Chapter 7

Conclusions

> A man should look for what is, and not for what he thinks should be.
>
> (Albert Einstein)

In this thesis we have shown that in small systems flow-like effects have been discovered at the LHC. Also as discused in chapter 4, flow-like effects can be biassed by the jet or produced by QCD interactions among scattered partons. Therefore, we discussed the necessity of developing new tools and ideas to make an event separation which could allow the isolation of the new physics. For this, we have proposed to use spherocity to classify the events essentially in two different classes, jetty and isotropic events, In this way, we are promoting the double differential analysis of run 2 pp data. From the analysis of the mid-rapidity average p_{T} as a function of the event multiplicity for different event classes selected using transverse spherocity we can conclude that:

- In non-isotropic (jet-like) events the average p_{T} exhibits a steeper rise with multiplicity than in isotropic events.
- For the inclusive spherocity integrated, within systematics uncertainties, all models (Epos-LHC, Pythia 6 and 8) seem to reproduce the data.
- The behavior for jet-like events is well modelled by Epos-LHC up to systematics uncertainties, but all other models as Pythia fails, clearly, the model significantly overestimate the mean p_{T} .
- The results for isotropic events show a saturation of the average p_{T} at high multiplicity, the behavior is quantitatively well modeled by Pythia 8.

Mean p_{T} vs multiplicity is a measurement which is useful to constrain the phenomenological models of particle production, e.g. color reconnection models can be tuned. The double differential analysis shown here allows to test the models where underlying event (or core contribution) is enhanced or suppressed with respect to the multiplicity dependent case. The largest tension between data and Pythia (6 and 8) is observed for non-isotropic events, where color reconnection can affect the low p_{T} part of the spectrum due to the presence of a hard parton. This can be used to study the soft-hard interaction.

Appendix A

ALICE coordinate system and some Lorentz invariants from kinematic variables

A particle with energy E, rest mass m_0 and momentum $\vec{p}$, is described by the cuadrimomentum $(E, \vec{p}) = (E, p_x, p_y, p_z)$. The momentum of a particle can be divided into its longitudinal momentum p_l and its transverse momentum p_{T} . Using the ALICE coordinate system shown in Fig. A.1, with the ϑ the polar angle and ϕ the azimuthal angle, we can define the lineal, longitudinal and transverse momentum as $p = |vecp| = \sqrt{p_l^2 + p_{\mathrm{T}}^2}$, $p_l = p\cos\vartheta = p_z$, $p_{\mathrm{T}} = p\sin\vartheta = \sqrt{p_x^2 + p_y^2}$.

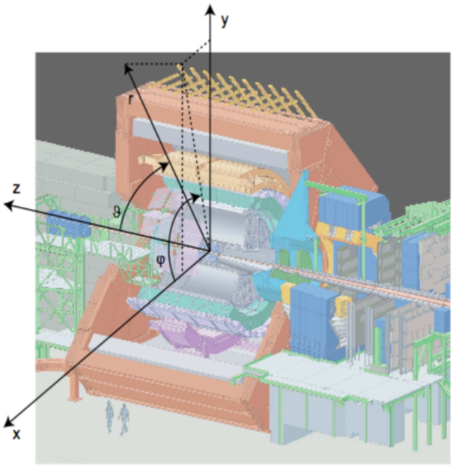

Figure A.1: ALICE coordinate system.

The mandelstam variables that are used to describe the reactions 2 → 2 are described as follow. Suppose that P_1 and P_2 (P_3 and P_4) are the cuadrimomentums of the incoming (outgoing) particles, the variables are defined as:

$$\begin{aligned} s &= (P_1+P_2)^2 = (P_3+P_4)^2, && \text{(A.1)}\\ t &= (P_1-P_3)^2 = (P_2-P_4)^2, && \text{(A.2)}\\ u &= (P_1-P_4)^2 = (P_2-P_3)^2, && \text{(A.3)}\\ & && \text{(A.4)} \end{aligned}$$

where $\sqrt{s}$ is the energy of a collision in the center of mass of the colliding particles, and $\sqrt{t}$ is recognized as the transfered momentum in the reacction. It can be shown that

$$s+t+u = m_1^2+m_2^2+m_3^2+m_4^2 \tag{A.5}$$

Thus, for a mass less particle we have $s+t+u=0$. In case of ion collisions, the energy collision is given by the pairs of nucleons and is denoted as $\sqrt{s_{NN}}$, more details how to calculated will be given feww lines after. As we know, the transverse momentum is a Lorentz invariant, while the longitudinal momentum is not, another Lorentz invariant is the "rapidity" y, which is defined as

$$y = \frac{1}{2} ln\left(\frac{E+p_l}{E-p_l}\right), \tag{A.6}$$

the determination of this rapidity sometimes is complicated, due to the fact that E can not be easily measured without the determination of the kind of particle. In order to avoid some issues, it is ussually defined the pseudorapidity η (another Lorentz invariant) which is alway used when $E >> m_0$ and this is defined as:

$$\eta = \frac{1}{2} ln\left(\frac{p+p_l}{p-p_l}\right) = \ln(tan(\frac{\vartheta}{2})), \tag{A.7}$$

for ultrarelativistic particles ($v \sim c$) the rapidity can be approximate to the pseudorapidity.

For the measurement of particle spectra, a triple diferential yield can be expressed with the help of the variables $(y, p_{\mathrm{T}}, \phi)$ in the form

$$E\frac{d^3N}{dp^3} = \frac{d^3N}{d\phi dy p_{\mathrm{T}} dp_{\mathrm{T}}} = \frac{1}{2\pi p_{\mathrm{T}}}\left(\frac{d^2N}{dy dp_{\mathrm{T}}}\right), \tag{A.8}$$

where N correspond to the number of produced or generated (for MC) particles. Experimentally the transverse momentum can be measured with the track curvature, but the rapidity is not accessible, so in most cases for the measurement of unidentified particles the results are present using $\frac{d^2N}{d\eta dp_{\mathrm{T}}}$. For identified particles the difference between η and y takes into account the mass, to see this, we use the fact that:

$$\frac{dN}{d\eta} = \left(\frac{dy}{d\eta}\right)\frac{dN}{dy}, \tag{A.9}$$

with the jacobian $dy/d\eta = \frac{cosh(\eta)}{\sqrt{cosh^2(\eta)+m_0^2/p_{\mathrm{T}}^2}}$

As consecuence the acceptance rapidity region depends on the mass and the momentum of the particle. This dependence is illustrated in Fig A.2

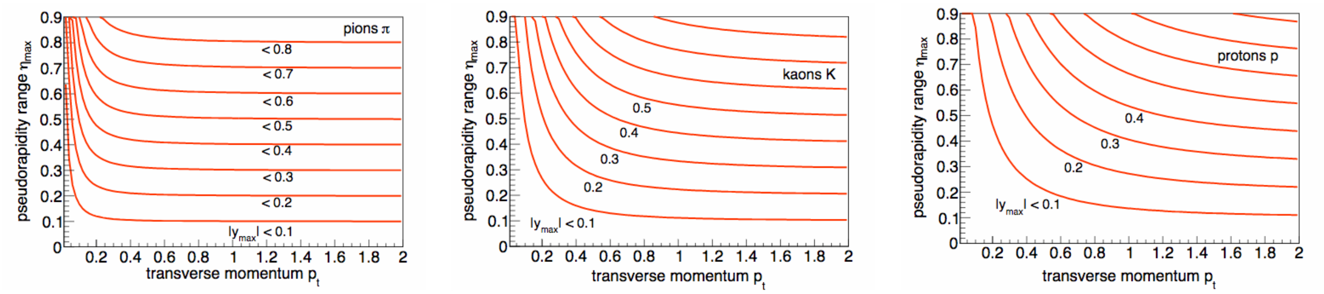

Figure A.2: Pseudorapidity range η as function of transverse momentum p_{T} for different rapidity ranges and particle masses [76].

Sometimes the reference system of laboratory is taken as the center of mass energy, for the cases where we have assimetric colliding systems, it occurs that the laboraroty sistem does not coincide with the center of mass system, and then $\eta_{NNcms} = \eta_{lab} + \Delta y_{NN}$ as an approximation for massless particles or large p_{T} . Actually the proper transformation of pseudorapidity under a boost along the beam direction is:

$$sinh(\eta_{cms}) = sinh(\eta_{lab} - y_{cms}) - \left(\sqrt{\frac{m^2}{p_{\mathrm{T}}^2} + cosh^2(\eta_{lab})} - cosh(\eta_{lab}) \right) \tag{A.10}$$

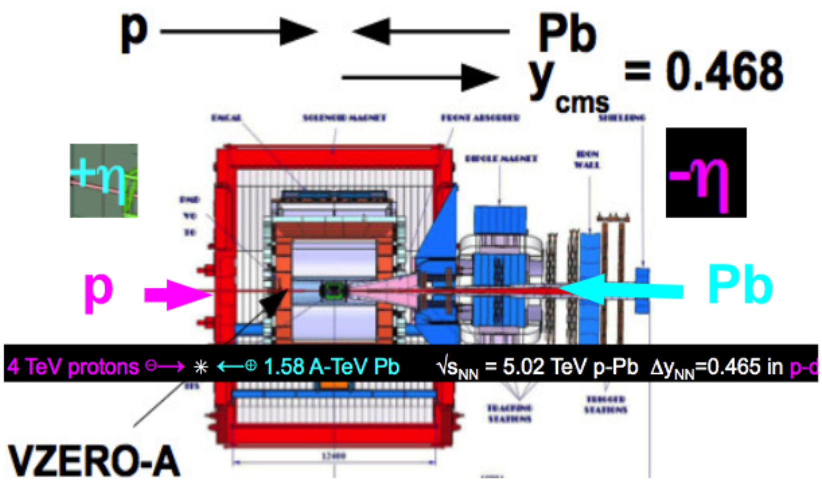

Figure A.3: Schematic draw for an assymetric colliding system.

To calculate the center of mass energy ($\sqrt{s}$) there are some considerations, for example when the proton are colliding with led ions (other colliding systems can be used), there is a relation taking into account that the magnetic field is equal in the two beam appertures using equal magnetic rigidity, between the momenta of the proton and the momenta of the lead ion given by [198] $p_{lead} = Qp_{proton}$, where $Q = Z = 82$ tha atomic number of the ion, if we assume that the atomic weight is $Aw = 208$ for fully stripped Pb ions, then the center of mass energy and the central rapidity shift for colliding nucleon pair within ions (Z_1, Aw_1) and (Z_2, Aw_2) will be:

$$\sqrt{s} \approx 2cp_{proton}\sqrt{\frac{Z_1, Z_2}{Aw_1, Aw_2}}, \tag{A.11}$$

$$\Delta y \approx (1/2)log\left(\frac{Z_1 Aw_2}{Aw_1 Z_2}\right), \tag{A.12}$$

which are direct consequence of the magnet design via the relation above mentioned. In the next table A you can see the colliding energy at center of mass and the rapidity shift for different colliding systems

	p+p	Pb+Pb	p+Pb	d+Pb
E_v [TeV]	7 (3.5)	2.76	7+2.76 (4+2.76)	3.5+2.76
$\sqrt{S_{NN}}$ [TeV]	14 (7)	5.52	8.79 (5.02)	6.22
Δy	0	0	0.46)	0.12

Table A.1: Beam energy per nucleon (E_v), colliding energy at center of mass ($\sqrt{S_{NN}}$) and rapidity shift (Δy), inside parentesis for other energies [198].

Appendix B

Quark Gluon Plasma

Following the definition proposed by the STAR collaboration at RHIC the quark gluon plasma is defined as a (locally) thermally equilibrated state of matter in which quarks and gluons are deconfined from hadrons, so that color degrees of freedom become manifest over nuclear, rather than merely nucleonic, volumes [10]. Note the two essential ingredients of this definition, (a) the constituents of the matter should be quarks and gluons, and (b) the matter should have attained (local) thermal equilibrium. Any claim of discovery of QGP can follows only after these two requirements are shown to be fulfilled unambiguously. The existence of a phase of deconfined quarks and gluons at high temperature and/or large net baryon density has been theoretically predicted early on and assumed to exist in neutron stars and the early universe.

The phase diagram of nuclear matter, QCD phase transition

Strongly interacting matter can exist in different phases characterized by given temperatures and densities, as summarised by the phase diagram of QCD in the plane of temperature (T) and baryonic chemical potential (μ_B) see Fig.B.1, where the baryo-chemical potential is defined as the energy needed to increase the total number of baryons and anti-baryons in a system ($\mu_B = \partial E/\partial N_B$, with N_B the number of baryons, so this potential measures the net baryon density of the system and corresponds to the conservation of the baryon number as defined in 1.2). Cold nuclear matter, such as in the interior of a Pb nucleus, sits a $T = 0$ and $\mu_B \sim m_N = 940$ MeV[1]. The black curved arrow-line emerging from this point indicates the nuclear liquid-gas phase transition, with a critical endpoint at a temperature of about 7.5 MeV[75]. The red curved arrow-lines also indicates a few typical trajectories through the phase diagram which we can follow in relativistic heavy-ion collisions, this can go through for example hadron resonance gases at high temperature, then if the temperature is greater or the baryo-chemical potential is greater near the critical energy density limit ($e_c \approx 0.6$), the system can goes from a confined phase (where the chiral symmetry is broken) to a deconfinement phase (where QGP exist and where the restoration of the spontaneously broken chiral symmetry) in two different ways:

1. One is going through the crossover; which is a phase transition of second order, At this region, around the critical temperature T_c the energy density increases signaling an increase in the number of degrees of freedom. This is due to the confinement-deconfinement (crossover) phase transition. The Stefan-Boltzmann limit for an ideal gas is not reached even at temperatures of several times T_c, showing that in the QGP quarks and gluons are interacting, this phase is called a second order phase transition[2].
2. The other is to go through a first order phase transition in a Quarkyonic state [81] (where is approximately confined, but has a large baryon number density, and also a large energy density $e > e_c$) and then to the

---

[1] 931 MeV[80]

[2] In lattice QCD the order parameter of the phase transition to deconfinement is the expectation value of the Polyakov loop $\langle L \rangle$, which is related to the energy of a free quark. It vanishes for a confined phase ($\langle L \rangle = 0$), and is finite in the deconfined phase ($\langle L \rangle \neq 0$) [84]

QGP phase.

The point where the first and second order transition finds, it's called the triple critical point, where theoretically, the matter can be in three states (Hadron gas, QGP and Quarkyonic)[3], some methods to calculate this triple critical point can be seen in [82]. This has been challenging to find for different experiments at different colliding energies, for example LHC or SPS, at CERN in the France-Switzerland border, RHIC (BES I-II) or AGS at BNL in the USA, or SIS at GSI in Germany, other prominents future experiments as for example FAIR also at GSI and NICA in JINR at Dubna in Russia are designed also to look for this critical point, some results of the QCD phase diagram form experiments can be seen in Fig.B.2, some studies determine that the possible region where this critical point can be is at $\mu_{Bc} \sim 350 - 400$ MeV, at $T_c \sim 150 - 160$ [81][4] .

From QCD lattice calculations we know the phase structure along the temperature axis, with the deconfinement transition from a hadron resonance gas to a quark-gluon plasma at $T_{cr} \sim 170$ MeV[5]. Lattice QCD tells us that even for realistically small up and down quark masses the transition at $B = 0$ is most likely not a sharp phase transition but a rapid crossover.

Phenomenological models have long indicated that at non-zero μ_B the QGP and hadron gas are separated by a critical line of roughly constant critical energy density[6] $e_{cr} \sim 1$ GeV$/fm^3$.

At low temperatures and asymptotically large baryon densities quarks are also deconfined, although not in a quark-gluon plasma state but rather in a color superconductor. The superconducting state is separated from the QGP by a first order transition at a critical temperature estimated to be of order $30 - 50$ MeV. Whether it has a direct transition to normal nuclear matter or if other phases (e.g. involving pion or kaon condensates) intervene is presently not known.

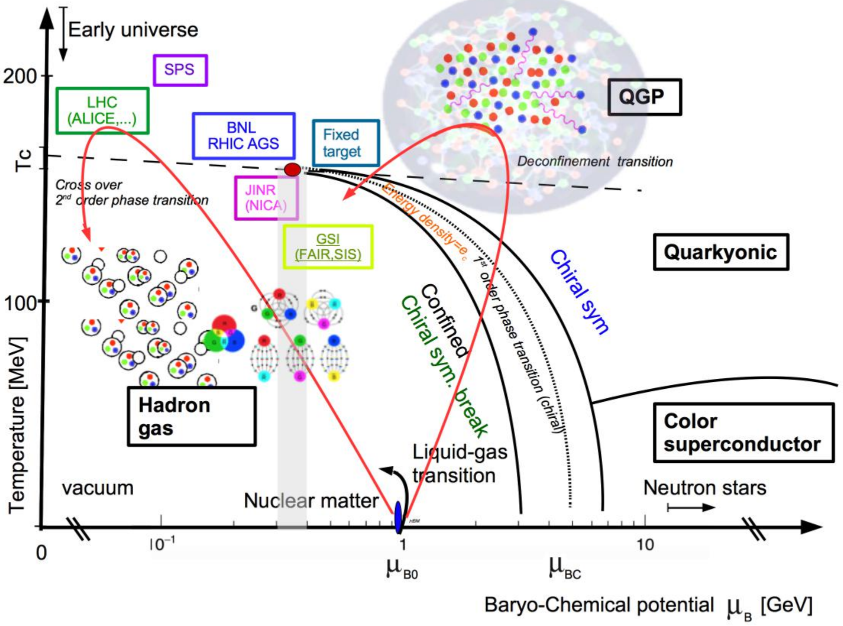

Figure B.1: Illustration of the QCD phase diagram.

---

[3] This triple point is located where the temperature is reaching its limiting value and, hence, is naturally also situated in the vicinity of the peaks in the observed hadron production ratios [81]

[4] Some studies reveal that below $\mu_B \sim 400$ GeV the temperature is approximately constant at 160 MeV [81]

[5] $T_{cr} \sim 165$ MeV [85], or $T_{cr} \sim 175 \pm 15$ MeV [84] at a critical energy density $e_{cr} \sim 0.3 - 1.3$ GeV/fm^3, from a review [87] some other values of critical temperature are: $T_{cr} \sim 169$ MILC collaboration, $T_{cr} \sim 147$ Wuppertal-Budapest Collaboration, $T_{cr} \sim 154$ Hot QCD collaboration, and a recently value of $T_{cr} \sim 155$

[6] Some citations mention that $e_{cr} \approx 0.6$ GeV [75]

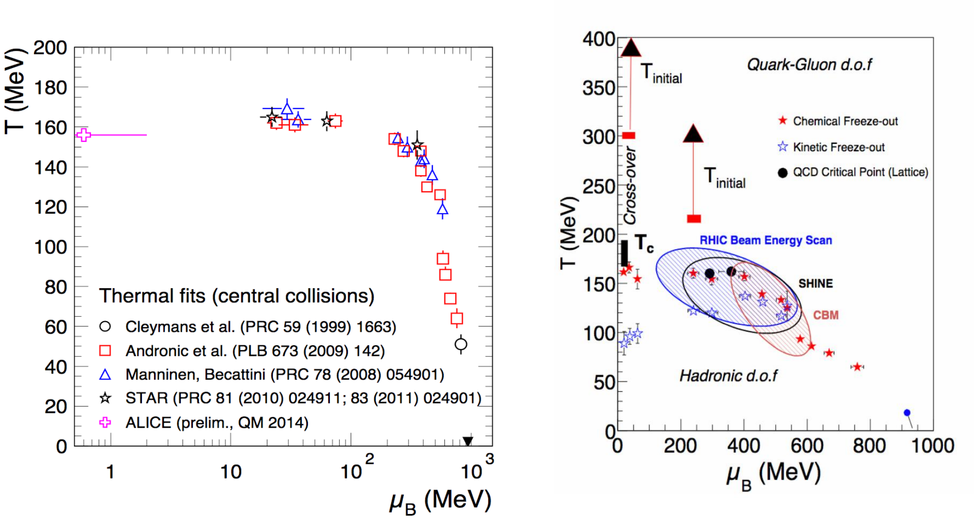

Figure B.2: QCD phase diagram from data a) showing results of ALICE ($\sqrt{s_{NN}} \sim 5-39$ GeV), STAR, SIS-GSI [9], b) from RHIC (collider, $\sqrt{s_{NN}} \sim 5-39$ GeV), SHINE (fixed target, $\sqrt{s_{NN}} \sim 5-17$ GeV) and CBM (fixed target, $\sqrt{s_{NN}} \sim 4-10$ GeV) [83].

The thermal model

In a system with many interacting particles the interesting quantities are macroscopic ones describing the system in terms of thermodynamic state variables. The observed yields of identified particles in heavy-ion collisions can be correctly described within hadro-chemical equilibrium models over a wide range of beam energies and collision systems. Similar to hydrodynamical calculations, thermal models rely on the fact that the system produceed in relativistic heavy-ion collisions behaves like a medium and that concepts, from statistical physics can be applied. To start we know that the grand canonical partition function for an ideal relativistic quantum gas of the particle species i is [78, 80, 76]:

$$ln(Z_{GK_i}) = \pm g_i \frac{V}{2\pi^2} \int_0^\infty p^2 ln\left(1 \pm exp\left(-\frac{E_i-\mu_i}{T_{chem}}\right)\right) dp \tag{B.1}$$

where g_i corresponds to the spin degeneracy factor, V to the volume of the system, T_{chem} to the chemical freeze-out temperature of the system, μ_i the chemical potential and $E_i = \sqrt{p^2+m_i^2}$. The chemical potential which is given by $\mu_i = \mu_B B_i + \mu_S S_i + \mu_{I_3} I_3 + \mu_C C_i$, consist of several components corresponding to the conserved quantum numbers in QCD like the baryon number B_i, the strangeness number S_i, the isospin I_3 and the charm number C_i. With this partition function, all relevant thermodynamic quantities can be calculated, in particular: the pressure $P = \frac{\partial TlnZ_{GK}}{\partial V}$, the entropy $S = \frac{\partial TlnZ_{GK}}{\partial T}$, the energy $E = T^2 \frac{\partial lnZ_{GK}}{\partial T}$ and the particle yield $N = \frac{\partial TlnZ_{GK}}{\partial \mu}$.

If the baryo-chemical potential is set to zero, the partition function is given for fermions by [80]:

$$(TlnZ)_{fermions} = \frac{g_f V}{12}\left(\frac{7\pi^2}{30}T^4 + (\mu T)^2 + \frac{1}{2\pi}\mu^4\right) \tag{B.2}$$

and for bosons by:

$$(TlnZ)_{bosons} = \frac{g_b V \pi^2}{90} T^4 \tag{B.3}$$

Energy density, presure and entropy density

Assuming the equation of state for an ideal gas given by $\rho = \epsilon/3$, where ρ is the density usually corresponding to the baryo-chemical potential μ_B, and ϵ is the energy density, and assuming that the hadronic phase is composed only of pions, the following equations are obtained for the energy densities of hadronic and QGP phases respectively [80].

$$\epsilon_h/T^4 = \frac{\pi^2}{10}, \tag{B.4}$$

$$\epsilon_{QGP}/T^4 = (32+21)N_f \frac{\pi^2}{60} \tag{B.5}$$

where N_f is the number of flavors. For $N_f = 3$, $\epsilon_{QGP}/T^4 = 15.6$, denoted as the Stefan-Boltzmann limit. In Fig. B.3 is interesting to note that the calculated values are well below the values for non-interacting gases, indicating that the QGP is far from an ideal gas at temperatures as high as several times T_c. From these relations we can see that in the QGP phase there is a huge increase in the number of degrees of freedom caused by the asymptotically free quarks and gluons.

In Fig B.3 also we see the lattice QCD calculation of ϵ/T^4 for 2 and 3 flavours QCD with light quarks and for 2 light plus 1 heavier (strange) quark (indicated by the central line) as a function of temperature is reported. The number of flavours and the masses of the quarks constitute the main uncertainties in the determination of the critical temperature and the critical energy density.

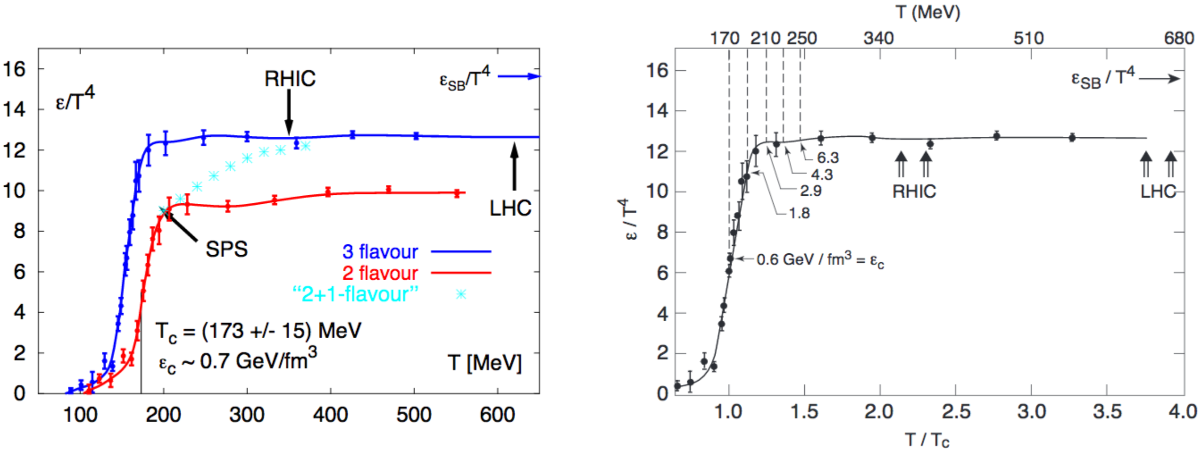

Figure B.3: Energy density in units of T^4 for QCD with two and three dynamical quark flavors. For 2 and 2+1 flavors the critical temperature is $T_c = 173 \pm 15$ MeV. The right figure indicates, for the case of 3 light flavors, absolute values for the energy density ϵ at several temperatures [75].

The interesting quantities are macroscopic ones describing the system in terms of thermodynamic state variables. In Figure B.4 shows the scaled energy density, pressure and entropy density as a function of temperature from lattice QCD calculations [86]. At the crossover region, around the critical temperature T_c the energy density increases signaling an increase in the number of degrees of freedom. To get some of the thermodynamics quantities from data, it is usual to extract the information from fits to the particle yields by using a Blast-Wave Analysis.

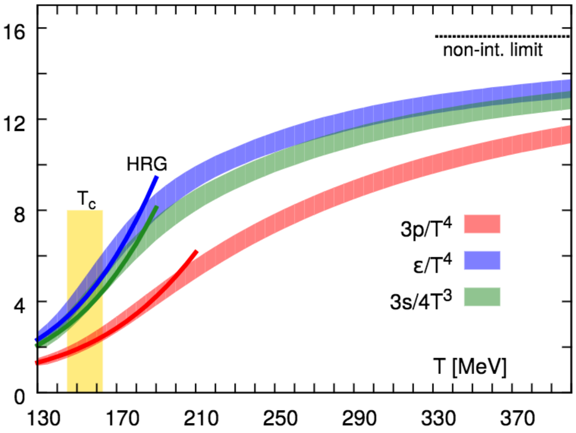

Figure B.4: Temperature dependence of the scaled energy density ϵ/T^4, pressure $3p/T^4$ and entropy density $3s/(4T^3)$ of QCD matter obtained from lattice QCD calculations with two light quarks and a heavier strange quark (2+1 flavor). The dark curves show the predictions from the hadron resonance gas model (HRG). The Stefan-Boltzmann limit for three flavors is indicated as horizontal line on the right. The crossover region, $T_c = (154 \pm 9)$ MeV [86].

Appendix C

QCD factorization theorem

The general description of the final stage hadron production it's obtained by mean of the QCD factorization theorem [61, 62], which can be summarized as:

$$\frac{d\sigma}{dX} = \sum_{j,k} \int_{\hat{X}} f_j(x_1, Q_i) f_k(x_1, Q_i) \frac{d\hat{\sigma}_{jk}(Q_i, Q_j)}{d\hat{X}} D_l^h(X, Q_l^{'}) \tag{C.1}$$

The factorization theorem is separated in two parts: the partonic cross section $\left(\frac{d\hat{\sigma}_{jk}(Q_i,Q_j)}{d\hat{X}}\right)$, that incorporates the short range process that are calculables in pQCD, and the universal functions that describe the non perturbative process, the parton distribution functions (PDFs) denoted as $f_j(x_1, Q_i)$ and the fragmentation functions (FFs) denoted as $D_l^h(X, Q_l^{'})$. The hard part of the process it's well described by pQCD, however the particle production at low momentum can be very difficult described by an analogous theory to QCD, rather than this, phenomenological models are used to describe some particular experimental measurements, but they fail in other measurements.

PDF's in proton proton collisions

As discused in the QCD factorization theorem, one important fact is to considere that in QCD processes, a proton can carry a probability of momentum fraction of certain kind of partons, that will dominate in the production processes. The Parton Distribution Functions, PDF[1] expressed as $f_i(x, Q^2)$ [61, 64, 65, 66], represents the effective density of partons of type/flavor i, as a function of the momentum fraction x (Björken-x), when a hadron of type is tested at the factorization scale Q^2 [43]

This quantity can't be obtained from pQCD calculations, and are obtained from fits to the cross section from experimental data as HERA (at DESY in Hamburg Germany) or TEVATRON (in Fermilab at USA), for example in Fig. C.1 it can be seen different PDFs obtained from HERA data for different partons and at different energy scale, as can be seen in the first plot there is a big difference between the NLO and NNLO PDF for gluons at low Q^2, which means that measurements at low momentum scale are important.

---

[1] also called Parton Densities or structure functions [43]

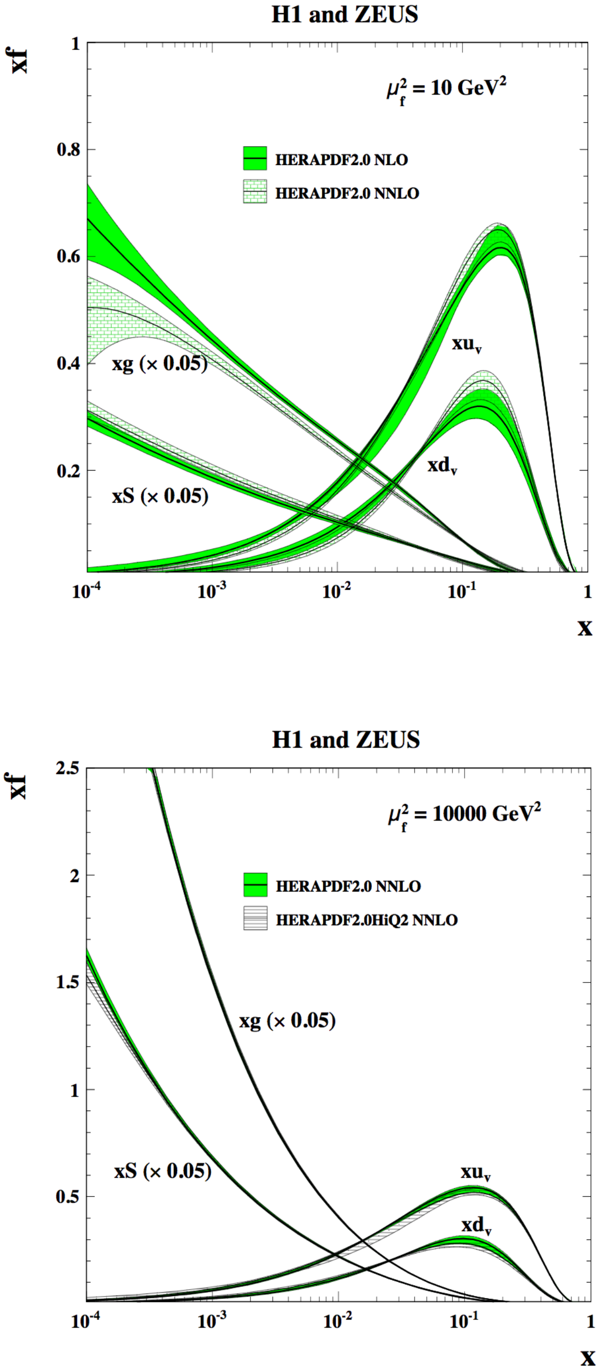

Figure C.1: Parton distribution function from HERAPDF2.0 at a) 10 GeV^2 at NLO and NNLO and b) 10 000 GeV^2 with no HiQ2 and with HiQ2 [65].

From this figure we can see that at low $Q = 10$ GeV (left), the proton structure is dominated by a few hard quarks (a “valence bump” is clearly visible around $x \approx 0.2$), while at higher scales Q= 10000 GeV (right) predominantly resolves fluctuations within fluctuations, leading to an increasingly large gluon and sea-quark distributions with rather small x values, while the valence quarks play a progressively smaller role [43].

As the PDF's depends on both x or Q^2, one can get the evolution of this functions with respect Q^2 by using the DGLAP[2] evolution equations or with respect to x, by using the BFKL[3] evolution equations [61, 68].

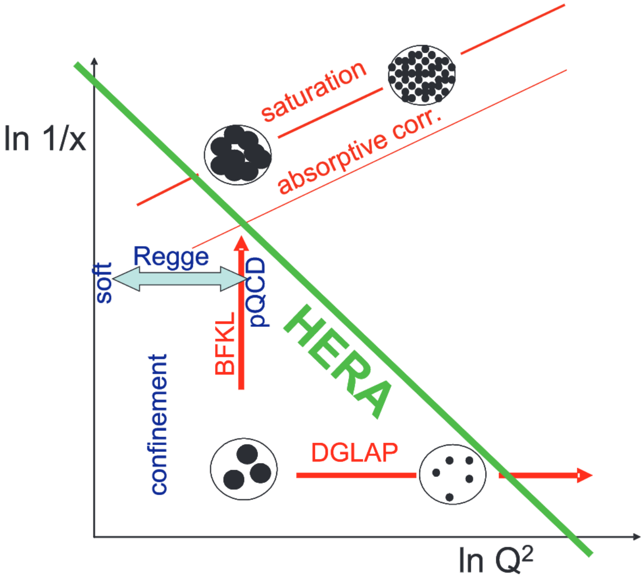

Figure C.2: Schematic sketch of the evolution of parton densities in various regions of the $log(1/x)$-$log(Q^2)$ plane, compared to the kinematic reach of HERA. DGLAP evolution takes us up in Q^2 and so the partonic constituents are resolved more finely. The BFKL equation takes us to small x, As x decreases, the partonic content increases, and at some stage the partons recombine, and eventually saturate [68].

Fragmentation functions (FFs)

This constitute one of the most important free inputs required for a comprehensive description of most collider processes to which perturbative QCD is applicable, being a necessary ingredient in any sufficiently complete calculation of processes involving detected hadrons in the final state. The fragmentation functions $D_l^h(X, Q_l^{'})$ represents the probability that a parton l fragments (or hadronize) in to a hadron h which carries a fraction of the partons momentum X, evaluated at a fragmentation scale $Q_l^{'}$, see for example [62, 63]. A high virtuality (i.e. large Q) parton develops into a parton shower containing many partons with smaller virtualities moving in approximately the same direction. Two processes contribute to this evolution: the splitting of a gluon into a quark-antiquark pair (gluon splitting) and the emission of a gluon by a parton (gluon emission). These processes are similar to the evolution of the PDFs and can be, as long as the Q is large, calculated in the framework of pQCD.

The FFs incorporate effects of large range (low Q^2), this means, not perturbative physics of the hadronization process where the observed hadrons are formed of final stages partons of the hard scattering processes and their scale dependence is drived by the DGLAP equation (similar to the PDFs). Models of hadronization employ different mechanisms, like cluster fragmentation (as used by the Monte Carlo event generator HERWIG) or string fragmentation (used in PYTHIA).

---

[2] Due to Dokshilzer, Gribov, Lipatov, Altarelli and Parisi [67].

[3] In honor to the authors who first wrote the QCD evolution equation Balitsky, Fadin, Kuraev and Lipatov

Appendix D

Average transverse momentum evolution with spherocity

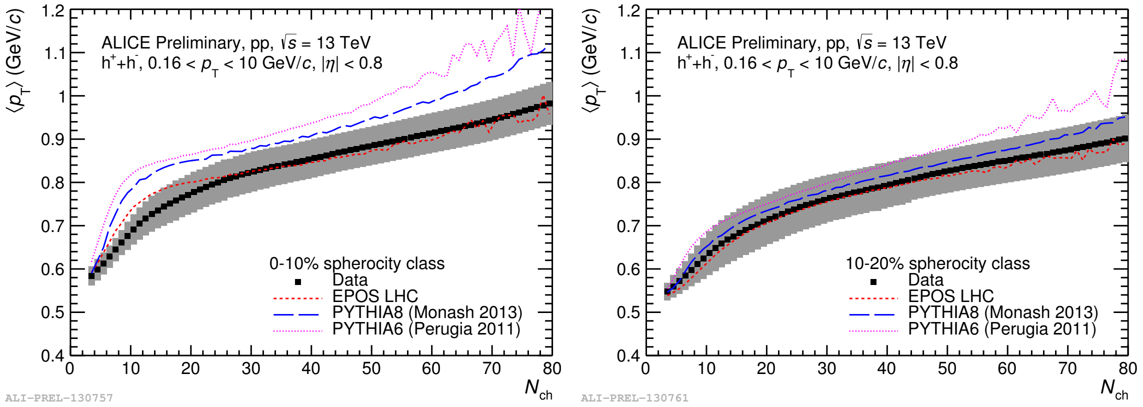

Figure D.1: Mean transverse momentum comparing data vs MC for spherocity percentile classes $0 - 10\%$ and $10 - 20\%$.

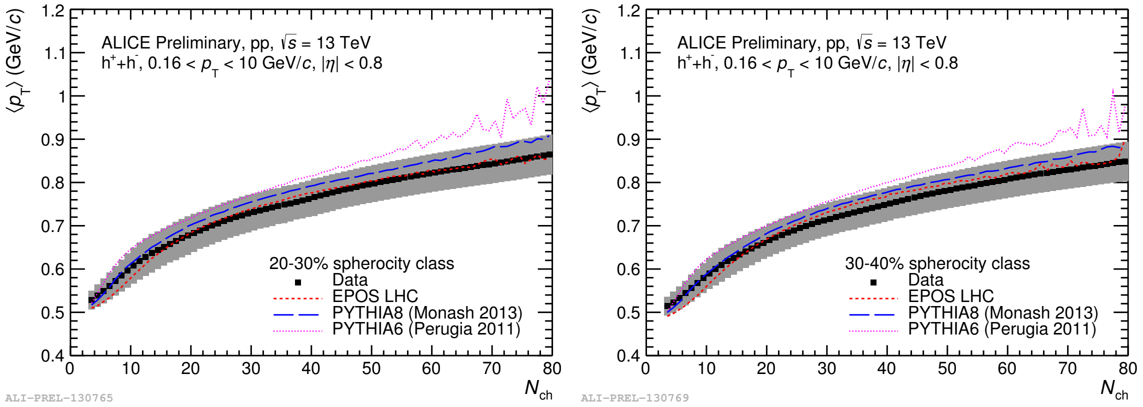

Figure D.2: Mean transverse momentum comparing data vs MC for spherocity percentile classes $20 - 30\%$ and $30 - 40\%$.

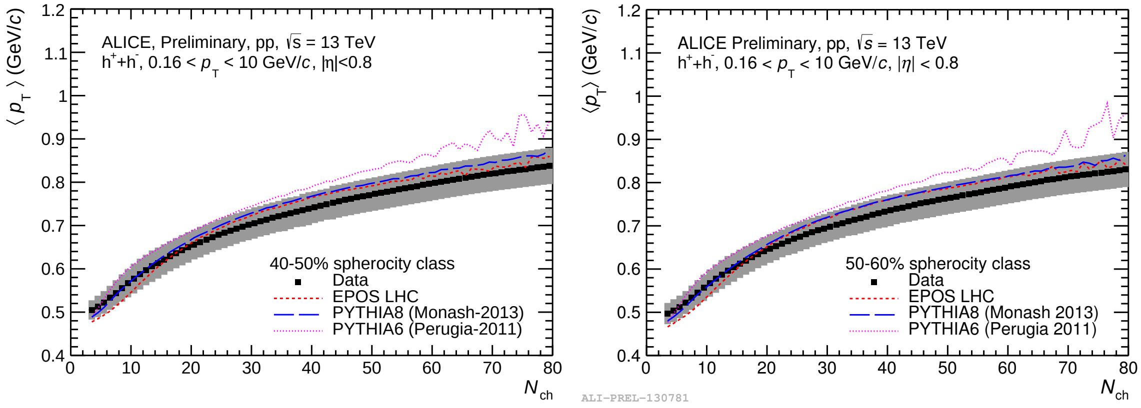

Figure D.3: Mean transverse momentum comparing data vs MC for spherocity percentile classes $40-50\%$ and $50-60\%$.

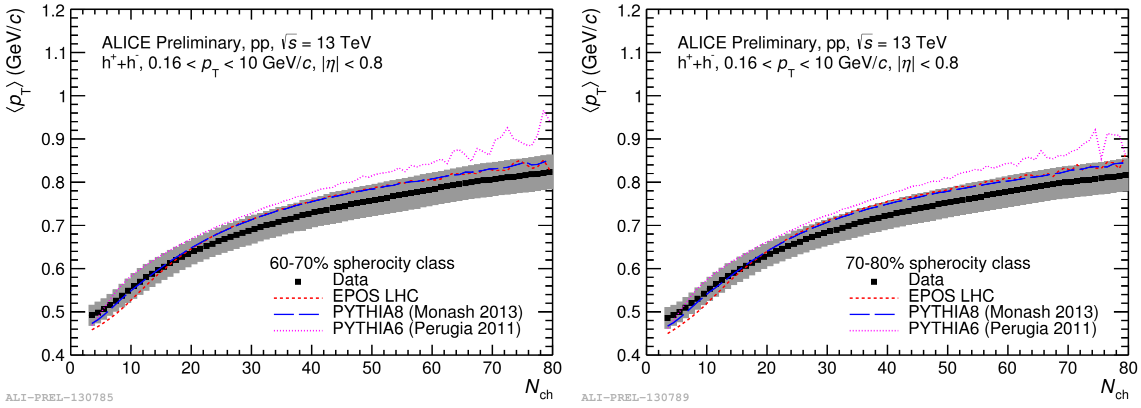

Figure D.4: Mean transverse momentum comparing data vs MC for spherocity percentile classes $60-70\%$ and $70-80\%$.

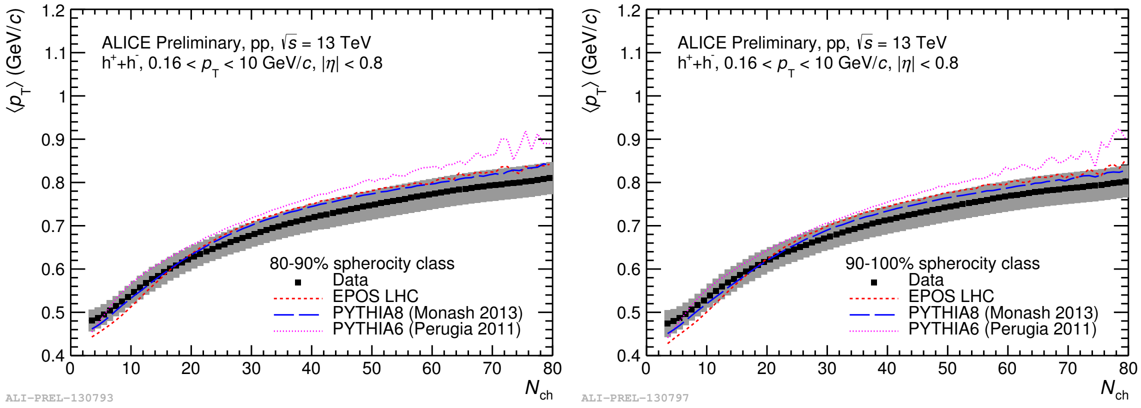

Figure D.5: Mean transverse momentum comparing data vs MC for spherocity percentile classes $80-90\%$ and $90-100\%$.

Appendix E

Technicalities for the track cuts

About the track cuts, the following definitions has been used:

For ITSTPC2011 golden:

```
AliAnalysisFilter* trackFilterGolden = new AliAnalysisFilter(“trackFilter”);
AliESDtrackCuts* esdTrackCuts = new AliESDtrackCuts(“AliESDtrackCuts”);
esdTrackCuts→SetRequireTPCRefit(kTRUE);
esdTrackCuts→SetAcceptKinkDaughters(kFALSE);
esdTrackCuts→SetMinNCrossedRowsTPC(120);
esdTrackCuts→SetMinRatioCrossedRowsOverFindableClustersTPC(0.8);
esdTrackCuts→SetMaxChi2PerClusterTPC(4.0);
esdTrackCuts→SetMaxFractionSharedTPCClusters(0.4);
esdTrackCuts→SetRequireITSRefit(kTRUE);
esdTrackCuts→SetClusterRequirementITS(AliESDtrackCuts::kSPD,AliESDtrackCuts::kAny);
esdTrackCuts→SetMaxChi2PerClusterITS(36.);
esdTrackCuts→SetDCAToVertex2D(kFALSE);
esdTrackCuts→SetRequireSigmaToVertex(kFALSE);
esdTrackCuts→SetMaxDCAToVertexZ(2.0);
esdTrackCuts→SetMaxDCAToVertexXYPtDep(“0.0182 + 0.0350/pt^1.01”);
esdTrackCuts→SetMaxChi2TPCConstrainedGlobal(36.);
trackFilterGolden→AddCuts(esdTrackCuts);
```

For TPC Only + TPC refit cuts:

```
AliAnalysisFilter* trackFilterTPCOnly = new AliAnalysisFilter(“trackFilter”);
AliESDtrackCuts* esdTrackCuts = new AliESDtrackCuts(AliESDtrackCuts”);
esdTrackCuts→SetAcceptKinkDaughters(kFALSE);
esdTrackCuts→SetMinNClustersTPC(70);
esdTrackCuts→SetMaxChi2PerClusterTPC(4);
esdTrackCuts→SetRequireTPCRefit(kTRUE);
esdTrackCuts→SetDCAToVertex2D(kTRUE);
esdTrackCuts→SetRequireSigmaToVertex(kFALSE);
esdTrackCuts→SetMaxDCAToVertexZ(3.2);
esdTrackCuts→SetMaxDCAToVertexXY(2.4);
trackFilterTPCOnly→AddCuts(esdTrackCuts);
```

List of Figures

Index of tables

Bibliography

[1] *M. Herrero.* THE STANDARD MODEL, arXiv:hep-ph/9812242 v1 3 Dec 1998.

[2] *Donald H. Perkins,* An introduction to High Energy Physics. Cambridge, cuarta edición pag 273.

[3] *D. Griffiths,* Introduction to Elementary Particles (2nd ed.). Wiley-VCH (2008). ISBN 978-3-527-40601-2.

[4] *C. Amsler (Particle Data Group); et al.* Review of Particle Physics (2008), Physics Letters B. 667 (1): 1-1340.

[5] *M. Gell-Mann*, A Schematic of Baryons and Mesons. Physics Letters. 8 (3): 214-215 (1964).

[6] *F. Carminati et. al.*, ALICE Physics Performance Report I, J. Phys. G: Nucl. Part. Phys. 30 No 11 (November 2004) 1517-1763.

[7] *F. Carminati et. al.*, ALICE Physics Performance Report II, J. Phys.G: Nucl. Part. Phys. 32 1295-2040.

[8] *K. Yagi, T. Hatsuda, Y. Miake*, Quarkâ“Gluon Plasma - From Big Bang to Little Bang, Cambridge University Press, 2005.

[9] *A. Andronic*, An overview of the experimental study of quark-gluon matter in high-energy nucleus-nucleus collisions, Int. J. Mod. Phys. A, 29, 1430047 (2014) arXiv:1407.5003 [nucl-ex]

[10] *STAR Collaboration: J. Adams, et al*, Experimental and Theoretical Challenges in the Search for the Quark Gluon Plasma: The STAR Collaboration's Critical Assessment of the Evidence from RHIC Collisions, Nucl.Phys.A757:102-183,(2005), arXiv:nucl-ex/0501009

[11] *K. Schweda, X. Zhu, M. Bleicher, S.L. Huang, H. Stoecker, N. Xu, P. Zhuang*, D-Dbar Correlations as a sensitive probe for thermalization in high-energy nuclear collisions Phys.Lett. B647 (2007) 366-370, arXiv:hep-ph/0604178.

[12] *Andrea Banfi, G. Salam and G. Zanderighi*, Phenomenology of event shapes at hadron colliders, JHEP 1006 (2010) 038, arxiv:1001.4082

[13] *Antonio Ortiz*, Experimental results on event shapes at hadron colliders, arXiv:1705.02056 2017.

[14] *Renu Bala, Irais Bautista, Jana Bielcikova, Antonio Ortiz*, Heavy-ion physics at the LHC: Review of Run I results, Int.J.Mod.Phys. E25 (2016) no.07, 1642006, arXiv:1605.03939

[15] *I. Bautista, Arturo Fernández, Premomoy Ghosh*, Collectivity in high-multiplicity events of proton-proton collisions in the framework of String Percolation, CONFERENCE ICPAQGP 2015, arXiv:1505.00924v2 [hep-ph] 6 May 2015.

[16] *Antonio Ortiz, Eleazar Cuautle, Guy Paić,* MC study of the mid-rapidity charged hadron transverse spherocity of the pp collisions, Nucl. Phys. A941, 78-86 (2015) arXiv:1503.03129 1 jun. 2015.

[17] *Ortiz, Antonio and Valencia Palomo, Lizardo*, Universality of the underlying event in pp collisions, arXiv 1710.04741 [hep-ex]

[18] *E. Cuautle, R. Jimenez, I. Maldonado, A. Ortiz, G. Paić, E. Perez*, Disentangling the soft and hard components of the pp collisions using the sphero(i)city approach, arXiv:1404.2372 [hep-ph] 9 apr. 2014.

[19] *P. Bozek, W. Broniowski, G. Torrieri*, Mass hierarchy in identified particle distributions in proton lead collisions, Phys. Rev. Lett. 111 (2013) 172303., arXiv:1307.5060,

[20] *T. Sjöstrand, M. van Zijl*, A Multiple Interaction Model for the Event Structure in Hadron Collisions, Phys. Rev. D36 (1987) 2019.

[21] `http://cepa.fnal.gov/psm/simulation/mcgen/lund/pythiamanual/pythia6.3/pythia6301/node213.html.`

[22] *T. Sjöstrand, S. Ask, J. R. Christiansen, R. Corke, N. Desai, P. Ilten, S. Mrenna, S. Prestel, C. O. Rasmussen, P. Z. Skands*, An Introduction to PYTHIA 8.2, Comput. Phys. Commun. 191 (2015) 159–177, arXiv:1410.3012.

[23] *P. Skands, S. Carrazza, J. Rojo*, Tuning PYTHIA 8.1: the Monash 2013 Tune,Eur. Phys. J. C74 (8) (2014) 3024. `arXiv:1404.5630`.

[24] *A. Ortiz Velasquez, P. Christiansen, E. Cuautle Flores, I. Maldonado Cervantes and G. Paić*, Color Reconnection and Flowlike Patterns in pp Collisions, Phys. Rev. Lett. **111**, no. 4, 042001 (2013), arXiv:1303.6326.

[25] *T. Lappi, B. Schenke, S. Schlichting, R. Venugopalan*, Tracing the origin of azimuthal gluon correlations in the color glass condensate, JHEP 01 (2016) 061., arXiv:1509.03499.

[26] *B. Schenke, S. Schlichting, P. Tribedy and R. Venugopalan*, Mass ordering of spectra from fragmentation of saturated gluon states in high multiplicity proton-proton collisions, Phys. Rev. Lett. 117, no. 16, 162301 (2016), arXiv:1607.02496.

[27] *G.-L. Ma, A. Bzdak*, Long-range azimuthal correlations in proton–proton and proton-nucleus collisions from the incoherent scattering of partons, Phys. Lett. B739 (2014) 209–213, arXiv:1404.4129.

[28] *C. Bierlich, G. Gustafson, L. Lonnblad, A. Tarasov*, Effects of Overlapping Strings in pp Collisions, JHEP 03 (2015) 148, arXiv:1412.6259.

[29] *ALICE collaboration, J. Adam et al.*, Multiplicity-dependent enhancement of strange and multi-strange hadron production in proton-proton collisions at $\sqrt{s}$ = 7 TeV, Nature Physics 13 (2017) 535-539, arXiv:1606.07424.

[30] *S. Chatrchyan, et al.*, Study of the inclusive production of charged pions, kaons, and protons in *pp* collisions at $\sqrt{s} = 0.9$, 2.76, and 7 TeV, Eur. Phys. J. C72 (2012) 2164, arXiv:1207.4724.

[31] *A. Ortíz, G. Bencédi, H. Bello, S. Jena*, Jet effects in high-multiplicity pp events, Proceedings of the 7th International Workshop on Multiple Partonic Interactions at the LHC, Trieste, Italy. arXiv:1603.05213.

[32] *Héctor Bello, Arturo Fernández, Antonio Ortiz and Guy Paić*, Spherocity analysis for the average transverse momentum versus multiplicity in pp colisions at 13 TeV, ALICE-ANA-3959 Mayo 2017.

[33] *Antonio Ortiz*, Event clasification using transverse spherocity and event multiplicity for the analysis of pp data, ALICE-ANA-3321 September 12, 2016.

[34] *A. Ortíz, G. Bencédi, H. Bello*, Revealing the source of the radial flow patterns in proton-proton collisions using hard probes, J. Phys. G: Nucl. Part. Phys. 44 (2017) arXiv:1608.04784 [hep-ph].

[35] *Héctor Bello, A. Fernandez Téllez, Antonio Ortiz*, Review of recent results on heavy-ion physics and astroparticle physics in ALICE at the LHC, J.Phys.Conf.Ser. 761 (2016) no.1, 012033, arXiv:1609.00692 [hep-ex] .

[36] *A. Andronic, J. Gronefeld, M. Knichel, P. Lüttig, M. Marquard, D. Miskowiec, J. Otwinowski, K. Schweda* Multiplicity Dependence of the Average Transverse Momentum in pp, p-Pb and Pb-Pb Collisions, ALICE-ANA-777.

[37] *The ALICE Collaboration* Multiplicity dependence of the average transverse momentum in pp, pPb, and PbPb collisions at the LHC, Phys. Lett. B 727 (2013) 371-380, arXiv:1307.1094, 25 oct 2013.

[38] *ALICE Collaboration*, Transverse momentum spectra of charged particles in proton-proton collisions at $\sqrt{s} = 900$ GeV with ALICE at the LHC, Phys. Lett. B 693 (2010) 53-68 arXiv:1007.0719.

[39] *A. Andronic, J. Gronefeld, M. Knichel, P. Luettig and J. Otwinowski*, Nuclear Modification Factor of Charged Particles in p-Pb 2013 Data, PRL110,082302 (2013), arXiv:1210.4520v1, ALICE-ANA-1343.

[40] *J Anielski, D.D. Chinellato, M. Floris, A. Kalweit, R Preghenella*, Analysis of π, K, K_s^0, p(p) and Λ in p-Pb collisions at $\sqrt{s}_N N = 5.02$ TeV. Phys.Lett. B728 (2014), arXiv:1307.6796 [nucl-ex] jan 2014, ALICE-ANA-738.

[41] *M. Floris, L. Milano, M. Tangaro*, Pions, Kaons and Proton production with the Event Shape Engineering technique in Pb-Pb collisions at $\sqrt{s}_{NN} = 2.76$ TeV, Phys. Rev. C 93 (2016) 034916, arXiv:1507.06194 [nucl-ex], ALICE-ANA-2012.

[42] *S. Bethke, G. Dissertori, and G.P. Salam*, QUANTUM CHROMODYNAMICS, (Particle Data Group), Chin. Phys. C, 40, 100001 (2016).

[43] *Peter Skands*, Introduction to QCD, Lecture notes from a course given at TASI 2012, arXiv:1207.2389, CERN-PH-TH-2012-196.

[44] *H. Fritzsch*, The history of QCD, CERN Courier October2012.

[45] *H. Fritzsch*, History of QCD, Subnucl.Ser. 50 (2014) 23-27.

[46] *M. Shifman*, Understanding Confinement in QCD: Elements of a Big Picture, Int.J.Mod.Phys.A25:4015-4031,2010, arXiv:1007.0531.

[47] *Siegfried Bethke*, Experimental Tests of Asymptotic Freedom, Prog.Part.Nucl.Phys.58:351-386,2007, arXiv:hep-ex/0606035.

[48] *Guido Altarelli*, The QCD Running Coupling and its Measurement, RM3-TH/13-3; CERN-PH-TH/2013-059 Proceedings of the Corfu Summer Institute 2012.

[49] *Jochen Schieck, Siegfried Bethke, Stefan Kluth, Christoph Pahl, Zoltan Trocsanyi, the JADE Collaboration*, Measurement of the strong coupling α_S from the three-jet rate in e^+e^- annihilation using JADE data, Eur. Phys. J. C (2013) 73: 2332 arXiv:1205.3714 [hep-ex].

[50] *David d'Enterria, Peter Z. Skands, et al.*, High-precision α_s measurements from LHC to FCC-ee, CERN-PH-TH-2015-299, CoEPP-MN-15-13, arXiv:1512.05194 [hep-ph].

[51] *H. David Politzer*, Reliable Perturbative Results for Strong Interactions?, Phys. Rev. Lett. 30, 1346 (1973).

[52] *David J. Gross and Frank Wilczek*, Asymptotically Free Gauge Theories. Phys. Rev. D 8, 3633 (1973).

[53] *Arthur Jaffe and Edward Witten*, QUANTUM YANG-MILLS THEORY, official problem one of the seven Millenium Prize Problems in Mathematics.

[54] *Dennis Sivers*, The Adventure and the Prize, arXiv:1109.2521 [hep-ph].

[55] *A.G. Williams*, QCD, Gauge Fixing, and the Gribov Problem, Nucl.Phys.Proc.Suppl.109A:141-145,2002, arXiv:hep-lat/0202010.

[56] *L.D.Faddeev and V.N.Popov*, Feynman diagrams for the Yang-Mills field. Physics Letters B 25, Issue 1, (1967), Pages 29-30.

[57] *Ed Kearns*, Grand Unified Theories and Proton Decay, Boston University, 2009, page 15, seventh NEPPSR talk

[58] *Griffiths, David* Introduction to Elementary Particles (2nd ed.). New York: John Wiley & Sons. p. 77. ISBN 9783527618477.

[59] *H. Nishino et al. (Super-Kamiokande Collaboration)* Search for Proton Decay via $p \to e{+}\pi^0$ and $p \to \mu{+}\pi^0$ in a Large Water Cherenkov Detector, Phys. Rev. Lett. 102, 141801, Published 8 April 2009.

[60] *Y. L. Dokshitzer, V. Khoze, A. Mueller, and S. Troyan*, Basics of Perturbative QCD, Editions Frontieres, (1991).

[61] *S. Albino*, Hadronization of partons, Rev. Mod. Phys. 82, 2489 (2010), arXiv:0810.4255 [hep-ph].

[62] *David d'Enterria, Kari J. Eskola, Ilkka Helenius, Hannu Paukkunen* Confronting current NLO parton fragmentation functions with inclusive charged-particle spectra at hadron colliders, Nuclear Physics B Volume 883, June 2014, Pages 615-628 arXiv:1311.1415 [hep-ph].

[63] *Andreas Metz, Anselm Vossen,* Parton Fragmentation Functions, Progress in Particle and Nuclear Physics (2016) pp. 136-202, arXiv:1607.02521 [hep-ex].

[64] *Ringaile Placakyte, for the H1 Collaboration, for the ZEUS Collaboration*, Parton Distribution Functions, arXiv:1111.5452 [hep-ph].

[65] *H1, ZEUS Collaborations*, Combination of Measurements of Inclusive Deep Inelastic $e^{\pm}p$ Scattering Cross Sections and QCD Analysis of HERA Data, arXiv:1506.06042 [hep-ex].

[66] *Hannes Jung, Aleksandra Lelek and Tania Martinez Cortes*, Transverse momentum dependent parton distribution functions from parton shower in pythia. DESY, September 2016. report.

[67] *Dmitri Diakonov* QCD scattering: from DGLAP to BFKL. CERN Courier July 2010.

[68] *Alan D. Martin*, Proton structure, Partons, QCD, DGLAP and beyond, Acta Phys.Polon.B39:2025-2062,(2008), arXiv:0802.0161.

[69] *E. Fermi*, High-energy nuclear events, Prog.Theor.Phys., vol. 5, pp. 570-583, 1950.

[70] *I. Y. .Pomeranchuk*,On the theory of multiple particle production in a single collision, Dokl. Akad. Nauk Ser. Fiz.78, 889 (1951)

[71] *L. Landau*, On the multiparticle production in high-energy collisions, Izv.Akad.Nauk Ser.Fiz., vol. 17, pp. 51â“64, 1953.

[72] *R. Hagedorn*, Statistical thermodynamics of strong interactions at high energies, Nuovo Cim. Suppl.3, 147 (1965).

[73] *Johann Rafelski*, Melting Hadrons, Boiling Quarks From Hagedorn temperature to ultra-relativistic heavy-ion collisions at CERN, Springer Open, DOI 10.1007/978-3-319-17545-4.

[74] *J. Björken*, Highly Relativistic Nucleus-Nucleus Collisions: The Central Rapidity Region, Phys.Rev., vol. D27, pp. 140-151, 1983.

[75] *Ulrich W. Heinz*, Concepts of Heavy-Ion Physics, CERN Yellow Report CERN-2004-001, pp.127-178 arXiv:hep-ph/0407360.

[76] *Kalweit, Alexander*, Production of light flavor hadrons and anti-nuclei at the LHC CERN-THESIS-2012-424.

[77] *Bianchin, Chiara*, Charm production at the LHC via $D^0 \rightarrow K^- \pi^+$ reconstruction in ALICE: cross section in pp collisions and first flow measurement in Pb-Pb collisions, CERN-THESIS-2012-033.

[78] *J. Cleymans, R.V. Gavai, E. Suhonen*, Quarks and gluons at high temperatures and densitiesReview Article, Pages 217-292.

[79] *E. Schnedermann, J. Sollfrank, U. W. Heinz* Thermal phenomenology of hadrons from 200-A/GeV S+S collisions, Phys. Rev. C48 (1993) 2462-2475, arXiv:nucl-th/9307020.

[80] *A. Andronic and P. Braun-Munzinger*, Ultrarelativistic nucleus-nucleus collisions and the quark-gluon plasma, The Hispalensis Lectures on Nuclear Physics Vol. 2. Lecture Notes in Physics, vol 652. Springer, Berlin, Heidelberg, arXiv:hep-ph/0402291.

[81] *A. Andronic, D. Blaschke, P. Braun-Munzinger, J. Cleymans, K. Fukushima, L.D. McLerran, H. Oeschler, R.D. Pisarski, K. Redlich, C. Sasaki, H. Satz, J. Stachel*, Hadron Production in Ultra-relativistic Nuclear Collisions: Quarkyonic Matter and a Triple Point in the Phase Diagram of QCD, Nucl.Phys.A837:65-86,2010, arXiv:0911.4806 [hep-ph].

[82] *M. A. Stephanov*, QCD phase diagram: an overview, PoS LAT2006:024,2006, arXiv:hep-lat/0701002.

[83] *Bedangadas Mohanty*, QCD Phase Diagram: Phase Transition, Critical Point and Fluctuations, Nucl.Phys.A830:899c-907c,2009, arXiv:0907.4476 [nucl-ex].

[84] *Frithjof Karsch*, Lattice QCD at High Temperature and Density, Lect.Notes Phys. 583 (2002) 209-249, arXiv:hep-lat/0106019.

[85] *F. Karsch*, Lattice results on QCD thermodynamics, Nucl.Phys., vol. A698, pp. 199â“208, 2002., Nucl.Phys.A698:199-208,2002, arXiv:hep-ph/0103314.

[86] *HotQCD Collaboration, A. Bazavov, et al.*, The equation of state in (2+1)-flavor QCD, Phys. Rev. D 90, 094503, (2014), arXiv:1407.6387 [hep-lat].

[87] *Alejandro Ayala, Adnan Bashir, J.J. Cobos-Martinez, Saul Hernandez-Ortiz, Alfredo Raya* The effective QCD phase diagram and the critical end point, Nucl. Phys.,B897,2015, pages 77-86, Arxiv:1411.4953.

[88] *Giovannini y Ugoccioni*, Possible scenarios for soft and semi-hard components structure in central hadron-hadron collisions in the TeV region, Phys.Rev. D 59: 094020 (1999), arXiv:hep-ph/9810446.

[89] *Berger et al.*, Evidence for Gluon Bremsstrahlung in e^+e^- Annihilations at High-Energies, Phys. Lett. B, Volume 86, pp. 418-425.

[90] *Manouk Rijpstra*, Power Corrections to Event Shapes, thesis. 2006.

[91] *Partha Konar and Probir Roy* Event shape discrimination of supersymmetry from large extra dimensions at a linear collider, Phys.Lett. B634 (2006) 295-301, arXiv:hep-ph/0509161.

[92] *ALICE Collaboration, B. Abelev, et al.*, Transverse sphericity of primary charged particles in minimum bias proton-proton collisions at $\sqrt{s} = 0.9$, 2.76 and 7 TeV, Eur. Phys. J. C 72 (2012) 2124, arXiv:1205.3963 [hep-ex].

[93] *UA1 Collaboration, G. Arnison et al.*, Transverse Momentum Spectra for Charged Particles at the CERN Proton anti-Proton Collider, Phys. Lett. B 118, 167 (1982).

[94] *ABCDHW Collaboration, A. Breakstone et al.*, Multiplicity dependence on the average transverse momentum and of the particle source size in pp interactions at $\sqrt{s}$ = 62, 44 and 31 GeV, Z. f. Physik C 33(3), 333 (1987).

[95] *UA1 Collaboration, C. Albajar et al.*, A Study of the General Characteristics of p$\bar{p}$ Collisions at $\sqrt{s}$ =0.2-TeV to 0.9-TeV, Nucl. Phys. B335, 261 (1990).

[96] *E735 Collaboration, T. Alexopoulos et al.*, Multiplicity dependence of the transverse-momentum spectrum for centrally produced hadrons in antiproton-proton collisions at $\sqrt{s}$ =1.8 TeV, Phys.Rev. Lett. 60, 1622 (1988).

[97] *STAR Collaboration, J. Adams et al.*, The Multiplicity dependence of inclusive p_T spectra from pp collisions at $\sqrt{s}$ =200 GeV, Phys. Rev. D 74, 032006 (2006), arXiv:nucl-ex/0606028.

[98] *J.D. Björken and S.J. Brodsky*, Statistical Model for electron-Positron Annihilation Into Hadrons, Phys. Rev. D1 (1970) 1416.

[99] *G. Hanson, et all* Evidence for jet structure in hadron production by e^+e^- annhilation , SLAC-m-1655-LBL-4287, October 1975.

[100] *W. Kittel y E. A De Wolf*, Soft Multihadron Dynamics, world scientific 2005.

[101] *K. Werner, B. Guiot, I. Karpenko, T. Pierog*, Analysing radial flow features in p-Pb and p-p collisions at several TeV by studying identified particle production in EPOS3, Phys. Rev. C89 (6) (2014) 064903, arXiv:1312.1233.

[102] *K. Werner, I. Karpenko, T. Pierog, M. Bleicher, K. Mikhailov*, Evidence for hydrodynamic evolution in proton proton scattering at 900 GeV. Phys. Rev. C83 (2011) 044915, arXiv:1010.0400.

[103] *S. Porteboeuf, T. Pierog, K. Werner*, Producing Hard Processes Regarding the Complete Event: The EPOS Event Generator, Proceedings, 45th Rencontres de Moriond on Electroweak Interactions and Unified Theories, 2010, 135–140, vol. 2, arXiv:1006.2967.

[104] *Iu.A. Karpenko, Yu.M. Sinyukov, K. Werner*, Uniform description of bulk observables in the hydrokinetic model of A+A collisions at RHIC and LHC, Phys. Rev. C 87, 024914 (2013), arXiv:1204.5351.

[105] *Maria Stefaniak,* Examination of heavy-ion collisions using EPOS model in the frame of BES program, Proc. SPIE. 10445, Photonics Applications in Astronomy, Communications, Industry, and High Energy Physics Experiments 2017, 104454M (7 August 2017).

[106] *K. Werner, Iu. Karpenko, M. Bleicher, T. Pierog, S. Porteboeuf-Houssais*, Jets, Bulk Matter, and their Interaction in Heavy Ion Collisions at Several TeV, Phys. Rev. C 85, 064907 (2012) arXiv:1203.5704.

[107] *T. Martin, P. Skands, S. Farrington*, Probing Collective Effects in Hadronisation with the Extremes of the Underlying Event, Eur. Phys. J. C76 (5) (2016) 299, arXiv:1603.05298,

[108] *P. Z. Skands* Tuning Monte Carlo generators: The perugia Tunes, may 2011.

[109] *T. Sjostrand et al.*, Comput. Phys. Commun., 82:74, 1994.

[110] *Public.web.cern.ch.* Retrieved 20 November 2010.

[111] *ALICE Collaboration, K Aamodt et al.*, The ALICE experiment at the CERN LHC, JINST 3 (2008) S08002.

[112] *ATLAS Collaboration, G. Aad et al.*, The ATLAS Experiment at the CERN Large Hadron Collider, JINST 3 (2008) S08003.

[113] *CMS Collaboration, S Chatrchyan et al*, The CMS experiment at the CERN LHC, JINST 3 (2008) S08004.

[114] *LHCb Collaboration, A.Augusto Alves, Jr. et al* The LHCb Detector at the LHC, JINST 3 (2008) S08005.

[115] *ALICE Collaboration*, ALICE Technical Design Report of the Inner Tracking System (ITS), CERN-LHCC 99-12 ALICE TDR 4,18 June 1999.

[116] *ALICE Collaboration*, ALICE Technical Design Report of the Time Projection Chamber. CERN/LHCC 2000â“001 ALICETDR7, 7 January 2000.

[117] *Acharya Shreyasi, Adam Jaroslav, Adamova Dagmar, Adler Clemens, Adolfsson Jonatan, Aggarwal Madan Mohan, Aglieri Rinella Gianluca, Agnello Michelangelo, Agrawal Neelima, Ahammed Zubayer.*, The ALICE Transition Radiation Detector: construction, operation, and performance, CERN-EP-2017-222, arXiv:1709.02743 [physics.ins-det].

[118] *ALICE Collaboration*, ALICE Addendum to the Technical Design Report of the Time of Flight System (TOF), CERN-LHCC 2002-016 Addendum to ALICE TDR 8 24 April 2002.

[119] *ALICE Collaboration, Piuz Francois et al.*, Technical Design Report of the High Momentum Particle Identification Detector, ALICE-TDR-1 ; CERN-LHCC-98-019.

[120] *ALICE Collaboration, Manko, V I et al.*, ALICE Photon Spectrometer (PHOS) : Technical Design Report, ALICE-TDR-2 ; CERN-LHCC-99-004.

[121] *ALICE Collaboration, Cormier Tom*, ALICE Electromagnetic Calorimeter Technical Design Report, CERN-LHCC-2008-014 ; ALICE-TDR-14.

[122] *Allen J, Bernard C, Bourrion O, Chala M, Del Franio M, Driga O, Fichera F, Giudice N, Grimaldi A,* ALICE DCal: An Addendum to the EMCal Technical Design Report Di-Jet and Hadron-Jet correlation measurements in ALICE, CERN-LHCC-2010-011 ; ALICE-TDR-14-add-1.

[123] *ALICE Collaboration, Cortese, P et al.*, ALICE Technical Design Report on Forward Detectors: FMD, T0 and V0, CERN-LHCC-2004-025

[124] *ALICE Collaboration, E. Abbas et al.*, Performance of the ALICE VZERO system, JINST 8 (2013) P10016, arXiv:1306.3130 [nucl-ex].

[125] *ALICE Collaboration, Abraham Villatoro Tello,* AD, the ALICE diffractive detector, AIP Conf.Proc. 1819 (2017) no.1, 040020 (2017-03-03).

[126] *ALICE webpage*, More details on the ALICE Diffractive Detector, http://alice.web.cern.ch/detectors/more-details-alice-diffractive-detector.

[127] *ALICE Collaboration, Fabjan, Christian Wolfgang et al.*, ALICE Photon Multiplicity Detector (PMD) : addendum to the Technical Design Report, ALICE-TDR-6-add-1 ; CERN-LHCC-2003-038.

[128] *ALICE Collaboration, Martinez-Garcia Gines et al.*, Technical Design Report for the Muon Forward Tracker, CERN-LHCC-2015-001 ; ALICE-TDR-018.

[129] *ALICE Collaboration* ALICE dimuon forward spectrometer : Technical Design Report, ALICE-TDR-5 ; CERN-LHCC-99-022.

[130] *ALICE Collaboration* ALICE dimuon forward spectrometer : addendum to the Technical Design Report, ALICE-TDR-5-add-1,CERN-LHCC-2000-046.

[131] *Gines Martinez for the ALICE Collaboration,* The Muon Spectrometer of the ALICE experiment for the ALICE collaboration Nucl.Phys.A749:313-319,2005, arXiv:hep-ex/0410061.

[132] *ALICE Collaboration, Gallio, M et al.,* ALICE Zero-Degree Calorimeter (ZDC) : Technical Design Report, ALICE-TDR-3 ; CERN-LHCC-99-005

[133] *Biolcati, Emanuele.* Distribution of hadrons identified with the Inner Tracking System of the ALICE experiment for p-p data, Ph.D Thesis, Universita degli Studi di Torino, Italia, 2011.

[134] *W. Blum and L. Rolandi* Particle Detection with Drift Chambers, Springer, Berlin, 1998.

[135] *Claus Grupen and Boris Shwartz,* Particle detectors 2nd ed Cambrige University Press, ISBN-13 978-0-511-38866-8.

[136] *Preghenella, Roberto* The Time-Of-Flight detector of ALICE at LHC: construction, test and commissioning with cosmic rays.CERN-THESIS-2009-206 - Bologna : Bologna U., 2009.

[137] *I. Foster and C. Kesselmann*, The Grid, Blueprint for a New Computing Infrastructure, 2nd edition, Morgan Kaufmann Publishers (2004).

[138] *S. Bagnasco et al.*, AliEn: ALICE environment on the GRID, J. Phys.: Conf. Ser. 119 Volume 119 (2008) 062012.

[139] *R. Brun and F. Rademakers*, ROOT: An object oriented data analysis framework, Nucl. Instrum. Meth. A 389 (1997) 81.

[140] *C. Legrand, H. B. Newman, R. Voicu, C. Cirstoiu, C. Grigoras, M. Toarta and C. Dobre*, MonALISA: An agent based, dynamic service system to monitor, control and optimize Grid based applications, Conference Proceedings of Computing in High-Energy and Nuclear Physics (CHEP), Interlaken, Switzerland (2004).

[141] *Jan Fiete Große-Oetringhaus*, Measurement of the Charged-Particle Multiplicity in Proton-Proton Collisions with the ALICE Detector, CERN-THESIS-2009-033.

[142] *ALICE Collaboration*, Pseudorapidity and transverse-momentum distributions of charged particles in proton-proton collisions at $\sqrt{s} = 13$ TeV, Phys. Lett. B 753 (2016) 319-329 arXiv:1509.08734 [nucl-ex].

[143] *Pierre Billoir*, Progressive track recognition with a Kalman like fitting procedure. Comput.Phys.Commun. 57 (1989) 390-394.

[144] *ALICE collaboration, Adam, et al.*, Direct photon production in Pb-Pb collisions at $\sqrt{s}_{NN} = 2.76$ TeV, Phys. Lett. B754 2016, 235-248, arXiv:1509.07324 [nucl-ex].

[145] *PHENIX Collaboration, Adare et al.* Centrality dependence of low-momentum direct-photon production in Au-Au collisions at $\sqrt{s}_{NN} = 200$ GeV, Phys.Rev.C91,2015,6,Arxiv:1405.3940.

[146] *ALICE collaboration, Aamodt, K et al.*, Centrality Dependence of the Charged-Particle Multiplicity Density at Midrapidity in Pb-Pb Collisions at $\sqrt{s}_{NN} = 2.76$ TeV, Phys. Rev. Lett.106, pages 032301, 2011, Arxiv:1012.1657.

[147] *Floris, M.* Hadron yields and the phase diagram of strongly interacting matter, Proceedings, 24th International Conference on Ultra-Relativistic Nucleus-Nucleus Collisions (Quark Matter 2014), Nucl. Phys.A931, 2014, pages 103-112, Arxiv:1408.6403.

[148] *ALICE collaboration, Aamodt, K et al.*, Two-pion Bose-Einstein correlations in central PbPb collisions at $\sqrt{s}_{NN} = 2.76$ TeV, Phys. Lett.,B696, 2011,pages 328-337, Arxiv:1012.4035.

[149] *STAR Collaboration, B.I. Abelev, et al.*, Hadronic resonance production in d+Au collisions at $\sqrt{s}_{NN} = 200$ GeV at RHIC, Phys.Rev.C78:044906,2008, arXiv:0801.0450 [nucl-ex].

[150] *Hanbury Brown, R. Twiss, R. Q.* A test of a new type of stellar interferometer on Sirius. Nature 178, 1046-1048 (1956).

[151] *Rainer J. Fries, Vincenzo Greco, Paul Sorensen*, Coalescence Models For Hadron Formation From Quark Gluon Plasma, Ann. Rev. Nucl. Part. Sci.,58, pages 177-205,2008, Arxiv:0807.4939.

[152] *Sebastian Sapeta, Urs Achim Wiedemann*, Jet hadrochemistry as a characteristics of jet quenching, Eur. Phys. J.,C55, pages 293-302,2008, Arxiv:0707.3494.

[153] *R. Bellwied, C. Markert*, In-medium hadronization in the deconfined matter at RHIC and LHC, Phys. Lett.,B691,pages 208-213, 2010, Arxiv:1005.5416.

[154] *ALICE collaboration, Abelev, B. et al.*, Centrality dependence of π, K, p production in Pb-Pb collisions at $s_{NN} = 2.76$ TeV. Phys. Rev. C 88, 044910 (2013), arXiv:1303.0737.

[155] *ALICE collaboration, Abelev, B. et al.*, Centrality determination of Pb-Pb collisions at $\sqrt{s}_{NN} = 2.76$ TeV with ALICE, Phys. Rev. C 88 (2013) 044909, arXiv:1301.4361 [nucl-ex].

[156] *ALICE collaboration, Abelev, B. et al.*, Production of charged pions, kaons and protons at large transverse momenta in pp and Pb-Pb collisions at $s_{NN} = 2.76$ TeV PLB 736 (2014) 196-207 arXiv:1401.1250 [nucl-ex].

[157] *ALICE collaboration, J. Adam et al.*, Centrality dependence of the nuclear modification factor of charged pions, kaons, and protons in Pb-Pb collisions at $s_{NN} = 2.76$ TeV, Phys. Rev. C 93, 034913 (2016), arXiv:1506.07287 [nucl-ex].

[158] *Piotr Bozek, Iwona Wyskiel-Piekarska*, Particle spectra in Pb-Pb collisions at 2.76 TeV, Phys.Rev.C85:064915,2012arXiv:1203.6513.

[159] *Chun Shen, Ulrich W. Heinz, Pasi Huovinen, Huichao Song*, Radial and elliptic flow in Pb+Pb collisions at the Large Hadron Collider from viscous hydrodynamic, Phys.Rev. C84, 044903 (2011), arXiv:1105.3226 [nucl-th].

[160] *Antonio Ortiz*, Mean pt scaling with m/nq at the LHC: Absence of (hydro) flow in small systems?, Nucl. Phys. A 943, 9-17 (2015), arXiv:1506.00584.

[161] *ALICE Collaboration, B.I. Abelev, et al.*, Elliptic flow of identified hadrons in Pb-Pb collisions at $\sqrt{s}_{NN} = 2.76$ TeV, JHEP 06 (2015) 190 arXiv:1405.4632.

[162] *ALICE Collaboration, B.I. Abelev, et al.*, Measurement of the inclusive differential jet cross section in pp collisions at $\sqrt{s}_{NN} = 2.76$ TeV, Phys. Lett. B 722 (2013) 262-272, arXiv:1301.3475.

[163] *ALICE Collaboration, J. Adam, et al.*, Measurement of jet suppression in central Pb-Pb collisions at $\sqrt{s_{\mathrm{NN}}}$ = 2.76 TeV, Phys. Lett. **B746** (2015) 1–14., arXiv:1502.01689.

[164] *Korinna C. Zapp, Frank Krauss, Urs A. Wiedemann*, A perturbative framework for jet quenching, J. High Energ. Phys. (2013) 2013: 80.

[165] *Thorsten Renk*, The Physics probed by the P_T Dependence of the Nuclear Suppression Factor, Phys. Rev. C 88, 014905 (2013), arXiv:1302.3710 [hep-ph].

[166] *ALICE collaboration, J. Adam et al.*, Azimuthal anisotropy of charged jet production in $\sqrt{s}_{NN} = 2.76$ TeV Pb-Pb collisions, Phys.Lett. B 753 (2016) 511-525, arXiv:1509.07334.

[167] *ALICE collaboration, J. Adam et al.*, Measurement of jet quenching with semi-inclusive hadron-jet distributions in central Pb-Pb collisions at $\sqrt{s}_{NN} = 2.76$ TeV, JHEP 09 (2015) 170 arXiv:1506.03984.

[168] *ALICE collaboration, Aamodt, K et al.*, Particle-yield modification in jet-like azimuthal di-hadron correlations in Pb-Pb collisions at $\sqrt{s}_{NN} = 2.76$ TeV, Phys. Rev. Lett. 108 (2012) 092301arXiv:1110.0121.

[169] *ALICE Collaboration, B.I. Abelev, et al.*, Anisotropic flow of charged hadrons, pions and (anti-)protons measured at high transverse momentum in Pb-Pb collisions at $\sqrt{s}_{NN} = 2.76$TeV, Phys. Lett. B 719 (2013) 18 arXiv:1205.5761

[170] *CMS Collaboration, S. Chatrchyan et al.*, Azimuthal anisotropy of charged particles at high transverse momenta in PbPb collisions at $\sqrt{s}_{NN} = 2.76$ TeV, Phys. Rev. Lett. 109 (2012) 022301, arXiv:1204.1850.

[171] *ATLAS Collaboration, G. Aad et al.*, Measurement of the Azimuthal Angle Dependence of Inclusive Jet Yields in Pb+Pb Collisions at sqrt(s(NN))= 2.76 TeV with the ATLAS detector, Phys. Rev. Lett.111 152301 (2013) arXiv:1306.6469.

[172] *Antonio Ortiz and Omar Vázquez*, Energy density and path-length dependence of the fractional momentum loss in heavy-ion collisions at $\sqrt{s_{\rm NN}}$ from 62.4 to 5020 GeV, arXiv:1708.07571 [hep-ph].

[173] *S A Bass*, Signatures of quark-gluon plasma formation in high energy heavy-ion collisions: a critical review, J. Phys. G: Nucl. Part. Phys. 25 R1.

[174] *L. G. Gutay, A. S. Hirsch, C. Pajares, R. P. Scharenberg, B. K. Srivastava*, De-Confinement in small systems: Clustering of color sources in high multiplicity pp collisions at $\sqrt{s} = 1.8$ TeV, Int. J. Mod. Phys. E 24, (1550101) 2015 arXiv:1504.08270.

[175] *I. Bautista, A. Fernandez Téllez, Premomoy Ghosh*, Indication of change of phase in high-multiplicity proton-proton events at LHC in String Percolation Model, Phys. Rev.,**D92**,2015,7,071504, arXiv:1509.02278 [nucl-th].

[176] *Kevin Dusling, Raju Venugopalan*, Azimuthal collimation of long range rapidity correlations by strong color fields in high multiplicity hadron-hadron collisions, Phys. Rev. Lett. 108, 262001 arXiv:1201.2658 [hep-ph].

[177] *Kevin Dusling, Raju Venugopalan*, Evidence for BFKL and saturation dynamics from di-hadron spectra at the LHC, Phys. Rev. D 87, 051502,2013 arXiv:1210.3890.

[178] *Kevin Dusling, Prithwish Tribedy, Raju Venugopalan*, Energy dependence of the ridge in high multiplicity proton-proton collisions, Phys. Rev. D 93, 014034 (2016)arXiv:1509.04410 [hep-ph].

[179] B.Alver, G.Roland, Collision geometry fluctuations and triangular flow in heavy-ion collisions, Phys.Rev.C81:054905,2010, arXiv:1003.0194 [nucl-th].

[180] CMS Collaboration (V. Khachatryan et al.), Observation of Long-Range Near-Side Angular Correlations in Proton-Proton Collisions at the LHC, JHEP1009, 091 (2010). arXiv:1009.4122.

[181] *CMS Collaboration, S.Chatrchyan et. al.*, Observation of long-range near-side angular correlations in proton-lead collisions at the LHC, Phys. Lett. B 718 (2013) 795 arXiv:1210.5482 [nucl-ex].

[182] *ALICE Collaboration, B. Abelev, et al.*, Long range angular correlations on the near and away side in p-Pb collisions at $\sqrt{s}_{NN} = 5.02$ TeV, Phys.Lett. B719 (2013) 29-41, arXiv:1212.2001 [nucl-ex].

[183] *ATLAS Collaboration, G. Aad et al.*, Observation of Associated Near-side and Away-side Long-range Correlations in $\sqrt{s_{NN}} = 5.02$ TeV Proton-lead Collisions with the ATLAS Detector, Phys. Rev. Lett. 110, 182302 (2013) arXiv:1212.5198.

[184] ALICE Collaboration, B. Abelev, et al., Long range angular correlations of π, K and p in p-Pb collisions at $\sqrt{s_{\rm NN}} = 5.02\,$TeV, Phys. Lett. B726,164-177,2013, arXiv:1307.3237.

[185] *ALICE collaboration, J. Adam et al.*, Multiplicity dependence of charged pion, kaon, and (anti)proton production at large transverse momentum in p-Pb collisions at $\sqrt{s_{\rm NN}} = 5.02\,$TeV, Phys. Lett. B728 (2014) 25–38., arXiv:1307.6796.

[186] *ALICE collaboration, J. Adam et al.*, Centrality dependence of the nuclear modification factor of charged pions, kaons, and protons in Pb-Pb collisions at $\sqrt{s_{\rm NN}} = 2.76$ TeV, Phys. Rev. C93 (3) (2016) 034913, arXiv:1506.07287.

[187] *ALICE Collaboration, B. Abelev, et al.*, Multiplicity dependence of pion, kaon, proton and lambda production in p–Pb collisions at $\sqrt{s_{\rm NN}} = 5.02\,$TeV, Phys. Lett. B728 (2014) 25-38, arXiv:1307.6796.

[188] *Richard Corke, Torbjörn Sjöstrand*, Interleaved Parton Showers and Tuning Prospects, JHEP,03,2011,032, arXiv:1011.1759 [hep-ph].

[189] *ALICE Collaboration, B. Abelev, et al.*, Multiplicity dependence of two-particle azimuthal correlations in pp collisions at the LHC, JHEP 09 (2013) 049, arXiv:1307.1249 [nucl-ex].

[190] *ALICE Collaboration, B. Abelev, et al.*, Multiplicity dependence of jet-like two-particle correlations in p-Pb collisions at $s_{NN} = 5.02$ TeV, Phys. Lett. B 741 (2015) 38, arXiv:1406.5463 [nucl-ex].

[191] *ALICE collaboration, J. Adam et al.*, Multi-strange baryon production in p-Pb collisions at $\sqrt{s_{\rm NN}} = 5.02\,$TeV, Phys. Lett. B758 (2016) 389-401, arXiv:1512.07227.

[192] *E. Cuautle, G. Paić*, The energy density representation of the strangeness enhancement from p+p to Pb+Pb, arXiv:1608.02101 [hep-ph].

[193] *CMS Collaboration, V. Khachatryan et al.*, Evidence for collectivity in pp collisions at the LHC, Phys. Lett. B **765**, 193 (2017), arXiv:1606.06198.

[194] *CMS Collaboration, V. Khachatryan et al.*Multiplicity and rapidity dependence of strange hadron production in pp, pPb, and PbPb collisions at the LHC, Phys. Lett. B **768**, 103 (2017), arXiv:1605.06699,

[195] *R. Bala, I. Bautista, J. Bielcikova, A. Ortiz*, Heavy-ion physics at the LHC: Review of Run I results, Int. J. Mod. Phys. E25 (2016) 1642006, arXiv:1605.03939.

[196] *J. Adam, et al.*, Measurement of charged jet production cross sections and nuclear modification in p-Pb collisions at $\sqrt{s_{\rm NN}} = 5.02\,$TeV, Phys. Lett. **B749** (2015) 68–81., arXiv:1503.00681.

[197] *B. G. Zakharov*, Flavor dependence of jet quenching in pp collisions and its effect on $\rm R_{AA}$ for heavy mesons, JETP Lett. 103 (6) (2016) 363–368, arXiv:1509.07020.

[198] *C. A. Salgado et. al.*, Proton-Nucleus Collisions at the LHC: Scientific Opportunities and Requirements, Journal of Physics G: Nuclear and Particle Physics, Volume 39, Number 1 (2011), arXiv:1105.3919 [hep-ph].

[199] *X. Lu*, Measurement of hadron composition in charged jets from pp collisions with the ALICE experiment, Nucl. Phys. A931 (2014) 428–432, arXiv:1407.8385.

[200] M. Veldhoen, p/π Ratio in Di-Hadron Correlations, Nucl. Phys. A910-911 (2013) 306–309, arXiv:1207.7195.

[201] *X. Zhang,* $\rm K^0_S$ *and* Λ *production in charged particle jets in p–Pb collisions at* $\sqrt{s_{\rm NN}} = 5.02$ *TeV with ALICE*, Nucl. Phys. A931 (2014) 444–448., arXiv:1408.2672.

[202] *S. Floerchinger and K. Zapp*, Hydrodynamics and Jets in Dialogue, Eur. Phys. J. C74 (2014) 12., arXiv:1407.1782v1.

[203] *M. Cacciari, G. P. Salam, G. Soyez*, FastJet User Manual, Eur. Phys. J. C72 (2012) 1896, arXiv:1111.6097.

[204] *Sergio Arturo Iga Buitron, Guy Paic, Eleazar Cuautle, Edgar Perez*, Measurement of the transverse momentum spectra of charged particles in function of charged multiplicity in pp collisions at $\sqrt{s} = 13$ and 5.02 TeV. ALICE-ANA-3450.

[205] *ALICE collaboration*, Insight into inclusive charged particle production using multiplicity and transverse spherocity in pp collisions at $\sqrt{s} = 5$ and 13 TeV, To be published in European Physical Journal C, approved in the ALICE Physics FORUM.

From left to right: Antonio Ortiz, Héctor Bello, Arturo Fernández.

Kung fu means the supreme hability for the hard work,
a great poet has achieved the kung fu,
a painter, the calligrapher, it can be said that has the kung fu,
even the chef or those who sweep the ladders
or a servant can has the kung fu,
practice, preparation and endless repetition,
until your mind be tired and the bones hurt,
until you be enough tired to perspire,
too exhausted to breathe,
this is the way, the only way which one gets the kung fu,
unfortunately youngster, you dont have it.
"one hundred eyes" character of the series Marco Polo (2014).

Reconocer no es bifronte como Roma a mí ...
Ciencia madre, hecha está de errores y aciertos,
equivocarse no es malo, es ingenuidad,
hacerlo de la misma forma es necedad,
el experto se ha equivocado con diferente actitud
cada lucha y caída, será historia grande, tú.
(Héctor Bello)